UNIVERSITÀ DEGLI STUDI DI PADOVA

Dipartimento di Fisica e Astronomia "Galileo Galilei"

Corso di Laurea Magistrale in Fisica

Tesi di Laurea

Simulation of lithium cooling and transport in Magnum-PSI using B2.5-Eunomia coupled codes

Relatore

Dr. Gianluigi Serianni

Relatore Esterno

Dr. Hugo de Blank

Laureando

Luca Balbinot

Anno Accademico 2017/2018

UNIVERSITÀ
DEGLI STUDI
DI PADOVA

TU/e Technische Universiteit Eindhoven University of Technology

DIFFER
Dutch Institute for
Fundamental Energy Research

Abstract

In a tokamak a part of the energy is deposited as heat in the region called divertor. Liquid metal divertors seem to be the candidate for next generation fusion experiments due to their numerous cooling channels like ionization and line radiation, and due to the fact that evaporated metals can be easily replenished thanks to high capillarity of metals. One on the main problems of this divertor concept is that if the metal density in the main plasma reaches the Greenwald limit it can cause disruption. For this reason lithium is the best candidate for liquid metal divertors due to its low Z number. Liquid lithium targets concepts can be studied in linear devices such as Magnum-PSI that reproduces divertor high density, low electron temperature conditions. Magnum-PSI plasma dynamics is simulated by B2.5 a fluid model code, while neutral dynamics is simulated by Eunomia, a Monte Carlo code. The objective of this project is understanding plasma and neutral dynamics with the purpose of increasing cooling and reducing lithium density upstream. This will be done by studying the coupling of the two codes, upgrading lithium cooling and lithium emission, then internal validation with a liquid lithium target will be performed. Afterwards working range of plasma parameters will be studied calculating heat transport to the target and lithium flux upstream with the aim of understanding the influence of plasma parameters. Target geometry will be studied by focusing on the vapor box divertor concept and the lithium transport will be optimized. Proposals for optimal liquid metal divertor and vapor box geometry are made according to the results of the simulations.

Contents

List of Figures

List of Tables

Introduction

The increasing electric energy demand will be one the biggest issues of this century. It is predicted that world electric energy demand will increase at least by 28% from nowadays to 2040 [7].
Fossil fuel power plants still play the bigger role in global energy production and they will do for the next decades [14], although they play the bigger role even in greenhouse gas emissions, such as CO_2, that is having an impact on climate changes [24]; this drives humankind to researching alternative energy sources.

Energy from nuclear fusion could be that alternative. Nuclear fusion is a relatively unlimited, zero CO_2 energy source. It also produces a limited amount of short living radioactive isotopes [25].
Magnetic confinement is the most studied way to reach nuclear fusion conditions; the currently dominant magnetic configuration is the tokamak. In a tokamak very few particles ($10^{20}\,\mathrm{part/m^3}$) with energy of about 10 keV are confined. To avoid those high energy particles to diffuse to the vessel wall, the most external of them are driven, by magnetic field lines, to impact on a very specific part of the device, the divertor. In figure 1a a sketch of the poloidal section of a tokamak is shown: the external blue lines represent the poloidal magnetic field lines that drive the outer particles to the divertor legs

The future reactor divertor will be required to be able to handle $20\,\mathrm{MW/m^2}$ [32] of power from the plasma. ITER [1] divertor will be composed by tungsten plates; it is already known that this will not be the configuration of future reactor divertor because of the limited life of tungsten plates due to erosion. Liquid metal divertors represent an alternative in power handling. Liquid metals are chosen because of their strong capillarity, which helps refilling continuously the zone of the divertors where plasma evaporates particles [30], and because evaporated metal forms a cloud in front of the plasma facing components (PFCs) that reduces heat load to the divertor by radiation cooling. The major issues with liquid metal divertors are tritium retention and metal diffusion from the divertor area to the core of plasma, because, if the impurity density upstream reaches the Greenwald limit[23], it can cause a sudden shut-down of the plasma, called disruption. For this second issue lithium is a good candidate for liquid metal PFCs due to its low atomic number and the fact that the Greenwald density limit decreases with increasing atomic number.

The physics of the divertor region is very different from the plasma core physics because of low electron temperature (few eV) and high neutral pressure (several Pascal), so in the divertor area neutral kinetics must be taken into account. Studying neutrals and ions kinetics in this particular region is very important to understand the amount of lithium going into the main plasma and the amount of energy that a certain configuration of the divertor could handle. For this reason numerical codes were developed. Eunomia is a code that, through a Monte Carlo approach, simulating several test particles, determines neutral distribution function together with neutral and ion gain and loss channels. On the other hand, B2.5 is a code that solves the ion continuity equation, equation of motion and energy equation starting from a given neutral and electron background. Several coupled iteration of the two codes can reproduce neutral-plasma interaction.
On the experimental side, divertor conditions can be reproduced in linear devices such as Magnum-PSI at DIFFER [10]. In linear devices plasma parameters and target can be handled more easily than in toroidal devices; furthermore, simulating plasma and neutral motion in linear geometry is easier due to

[1] Next generation fusion experiment under construction in Cadarache in the south of France

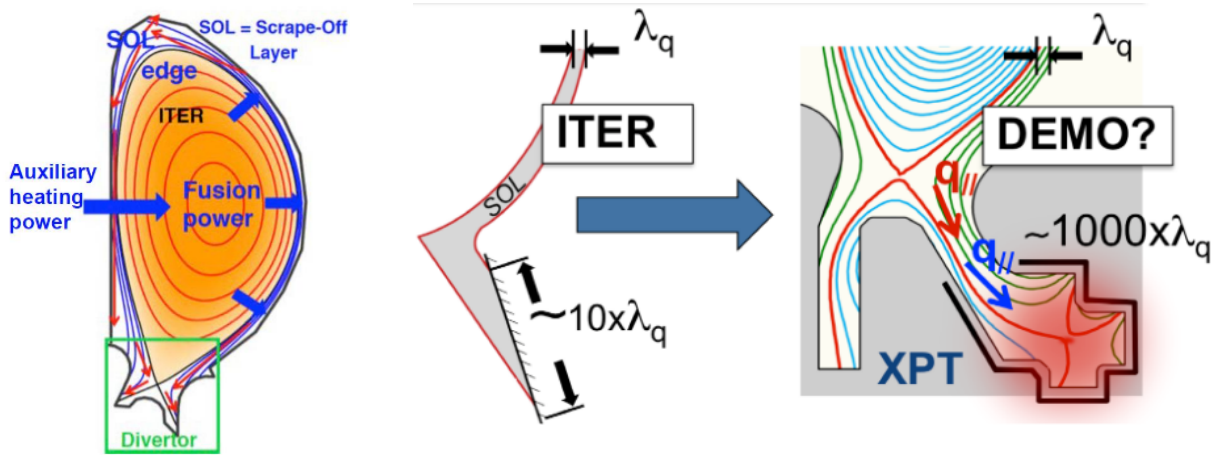

(a) Sketch of .the poloidal view of a tokamak[15].

(b) Sketch of the poloidal view of future ITER divertor and possible DEMO divertor[17].

Figure 1: Sketch of the poloidal view of a tokamak and its possible divertor legs.

their perfect axial geometry.

In both Eunomia and B2.5 stand alone lithium transport has been implemented[2] and verified for the geometry of MAGNUM-PSI. The two codes were written to work together: Eunomia provides B2.5 with the neutral background, after some iteration of B2.5, Eunomia redraws background and the cycle restarts. The coupling of the two codes has already been validated without lithium.
The topic of this project will be performing and internally validating the coupling of the two codes to simulate a plasma hitting a lithium target in Magnum-PSI, thus reproducing divertor-like conditions. Great importance will be given to simulations of lithium evaporation, transport and vapor cooling and to the assessment of their sensitivity to several parameters. The parameters that will be considered will be plasma temperature, plasma flux and its distribution, target temperature, target geometry, the possibility of using differential pumping vapor box, the number of its boxes, their temperature shape and size.

0.1 Research Goals

Although liquid lithium PFCs seem to provide various and efficient cooling channels, some problems still need to be solved like evaluating the amount of neutral and ionized lithium transported through the scrape off layer (SOL) to the plasma core. Magnum-PSI provides similar condition to those found in the divertor region: low plasma temperature (some eV), high particles flux $10^{24}\,\mathrm{m}^{-2}\mathrm{s}^{-1}$ and high neutral pressure. Anyway a linear device offers a simpler geometry than a toroidal one.
In both B2.5 and Eunomia stand-alone lithium transport has been implemented but the coupling of the two including Li transport still needs to be proved.
For this reasons the main questions of my project, simulating Magnum-PSI conditions are:

- **How are lithium transport and vapor cooling affected by different plasma and target parameters?**
- **How much and how can power load to the target and lithium transport upstream be reduced?**

Working on plasma parameters could seem unusual since in a tokamak plasma parameters upstream are fixed; although they change along the divertor region. For this reason knowing the working range of different plasma parameters facing liquid lithium will give information about the best conditions to

[2]Lithium in has been implemented in Eunomia by Ray Chandra in his master thesis work[6] while lithium has been implemented in B2.5 by Mike Machielsen in his master thesis work[20]. Both project had been carried on at DIFFER

have in the divertor region.
To be able to answer the previous questions I will answer the following preliminary question:

- Which are the physical conditions I should use in each code to get convergence and to get results that are physically correct?

Then I step further into the main part of my project that can be divided into some main questions that need to be answered step by step:

- Can I internally validate the coupling method and the relative predictions using a liquid lithium target in Magnum-PSI? Which are the parameters that can be used for experimental validation?
- Which are the most important plasma cooling channels in different conditions?
- With this set up can I answer to the two main questions?

How much my prediction could be applied to toroidal geometry is also very important for future fusion scenario. To do so, I need to predict the transport of neutral and ion particle to the different part of the beam. Lithium flux upstream could estimate lithium flux through the SOL while flux to the chamber wall could be related to lithium flux to the private region.
As anticipated ITER-like conditions prescribe that the divertor must dissipate $20\,\mathrm{MW/m^2}$ without reaching the Greenwald limit [22]. The goal is understanding how it is possible to get closer to that energy, by modifying the previous parameters, while keeping lithium density upstream below the Greenwald limit.

0.2 Project Workplan

The workplan is presented in this section. It will be divided into: preliminary question, validation, research of optimal plasma and geometrical parameters.

0.2.1 Preliminary Question

In this part of the project I have to become familiar with the coupling of the two codes and with handling code parameters. First of all I use a "perturbative approach", starting from small amount of lithium. This way I can understand the most important phenomena in different conditions. Then, thanks to those considerations I find the proper boundary conditions, the main reactions involved, on the target, on the walls and in the plasma. Further I will be able to describe the system with different parameters like temperature, lithium density, beam current etc.
First of all I need to be able to distinguish the different cooling contributions such as evaporation, radiation, collision with slow particles, in different plasma conditions. A simple collisional-radiative model (CRM) already exists for Eunomia [31] and has been implemented for lithium[6] on the Eunomia side. I investigate how much the present CRM can be applied to the coupled runs and whether it is necessary to expand it.
Current Eunomia version considers only Li and Li^+ lithium species. When running simulations with about 5 eV electron temperature (consistently with MAGNUM-PSI conditions) this is a good approximation because lithium first ionization energy is about 5 eV while second and third ionization energy are 75 eV and 85 eV respectively. Which is the validity range of this assumption? How can this method be extended to fusion scenario?
Which are its physical limits in describing plasma-neutral interactions?

0.2.2 Validation

In this project internal validation of the coupled codes will be done. The experiments in Magnum-PSI using liquid lithium target are planned short term so the proposed simulations will suit Magnum-PSI operative parameters in order to be used for the experimental validation of the coupled codes. The relevant parameters that can be experimentally checked will be underlined when the results will be

presented.
Internal validation will be performed for each simulation with the purpose of understanding whether the results of the simulation are consistent with the assumptions that brought me us to these.
For example, current Eunomia version does not consider three body interactions; this is a good assumption as long as lithium density is very low. In this case validation consists in calculating the ratio between cooling contribution or mean free path of the considered and not considered reactions making sure that the former are always dominant on the other. Otherwise I need to implement more collisions.
I also need to check if absorbing or reflecting boundary conditions to the walls are consistent with the results we will find [11].
Since both B2.5 and Eunomia are steady state codes total lithium flux in and out of the system must be 0 as much as energy fluxes. Those statement will be check as validation of the coupling of the two codes.
Other phenomena are studied like the relevance of supersonic jets in the vapor box concept and other higher order phenomena, that were not considered in the codes, will be investigated to validate the coupling. I will need to distinguish between regimes in which those kind of phenomena are not relevant and in which they are.

0.2.3 Research plasma parameters working range

In this part how lithium transport can influence cooling (and vice versa) is investigated. Different plasma parameters will be used in order to increase cooling performances and reduce lithium transport through the beam. This will be done performing different simulations to find the optimal plasma parameters with the purpose of:

- improving vapor shielding in order to reduce target temperature and lithium flux from the target,
- reducing lithium transport through the beam,
- increasing lithium redeposition.

Lithium flux upstream $\Gamma_{Li,u}$ and the energy dissipated by ionization and evaporation per unit of target area E_{cool}/A_{tar} will be calculated as function of target temperature, electron temperature, magnetic field, beam flux and lithium density in front of the target.
The closer to the target, the more linear geometry can approximate the toroidal one; for these reasons optimizing those three points in linear geometry could have an application even for the toroidal one. For this reason distinguishing between transport through the beam and transport out of the beam will be important. It will also be important distinguishing between neutral and ions transport. For example lithium flux upstream could estimate lithium flux through the SOL while flux to the chamber wall could be related to lithium flux to the private region. Al neutral fluxes in every part of the vessel could be calculated by Eunomia.

0.2.4 Research of optimal geometry

With the same objectives described in the previous chapter and with similar method I simulated lithium cooling and transport with a different target geometry.

The alternative geometry that is studied is the vapor box around the target as shown in figure 2b compared to the traditional target shown in figure 2a. This geometry should increase lithium density in front of the target, reducing target temperature and neutral lithium transport through the beam. This geometry as been studied using absorbing boundary condition to the wall.
With this concept more free parameters are available like temperature of each box and not only the target temperature. Understanding which of all this parameters are the most relevant to reduce lithium transport upstream and how much it can be reduced is the main purpose of this part of the project.

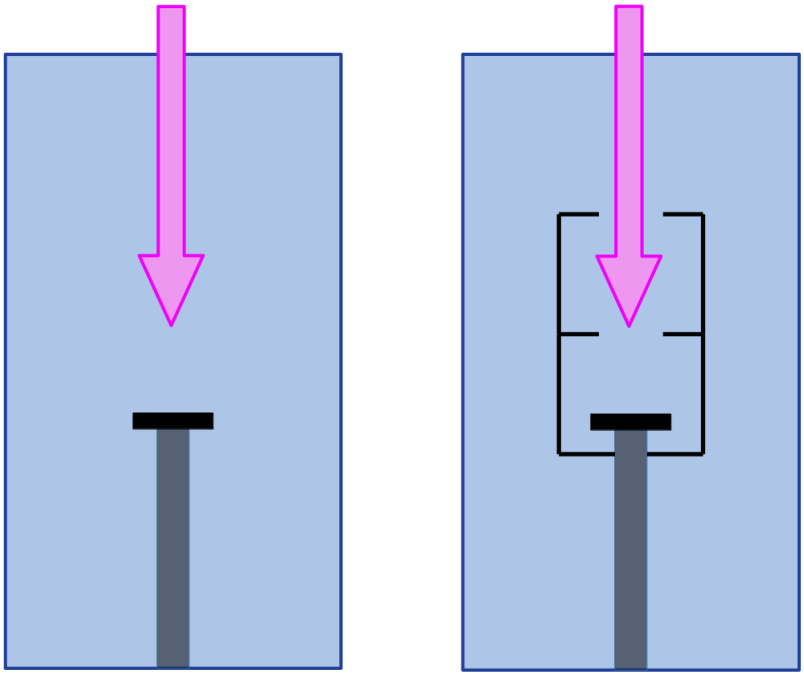

(a) Normal target (b) Vapor box concept

Figure 2: Sketch of the two target geometries that are studied. The grey part represent the target holder, the target is in black while the pink arrow represent plasma incoming in the target area.

Calculating E_{cool} for each box, I can estimate how many boxes are needed to dissipate power and when adding boxes does not relevantly improve power dissipation.
Furthermore, fixing box temperatures and knowing heat flux to the surface thanks to B2.5 I can estimate the amount of heat that has to be transported by conduction by each component.

Chapter 1

Background of the project

1.1 Magnum-PSI and liquid lithium target

Magnum-PSI is a linear device designed for testing divertors concepts. As it is shown in figure 1.1 Magnum-PSI is divided in three chambers, the source chamber, the heating chamber, out of which the super-magnet coils are positioned, and the target chamber. Each chamber is separated from the others by skimmers. Vacuum pumps are present in each of them.
Magnum-PSI operation range is described in figure 1.2.

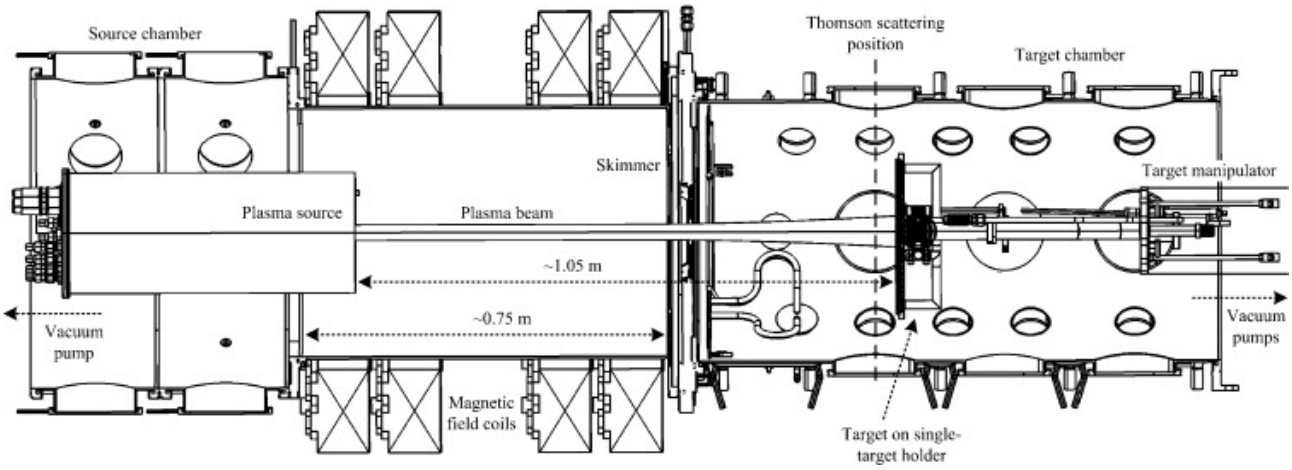

Figure 1.1: Plant of Magnum-PSI linear device[16]

Thanks to its design Magnum-PSI can operate with[10]:

- Heat fluxes $> 10\,\mathrm{MWm^{-2}}$
- Low neutral background density $< 1\,\mathrm{Pa}$
- Strong magnetic field up to $2.5\,\mathrm{T}$
- Cooling power of the target up to $100\,\mathrm{kW}$
- Long timescale due to steady state capability

Those are the the conditions that will be used as input parameters in my simulations. The possibility of long timescale of plasma exposure will be crucial for experimental validation since B2.5-Eunomia are steady state codes.

The lithium influx to Magnum-PSI target chamber comes from a target and the plasma-target interaction will be crucial in the simulations. The target that will be tested in Magnum-PSI is a 3D printed tungsten target[26].

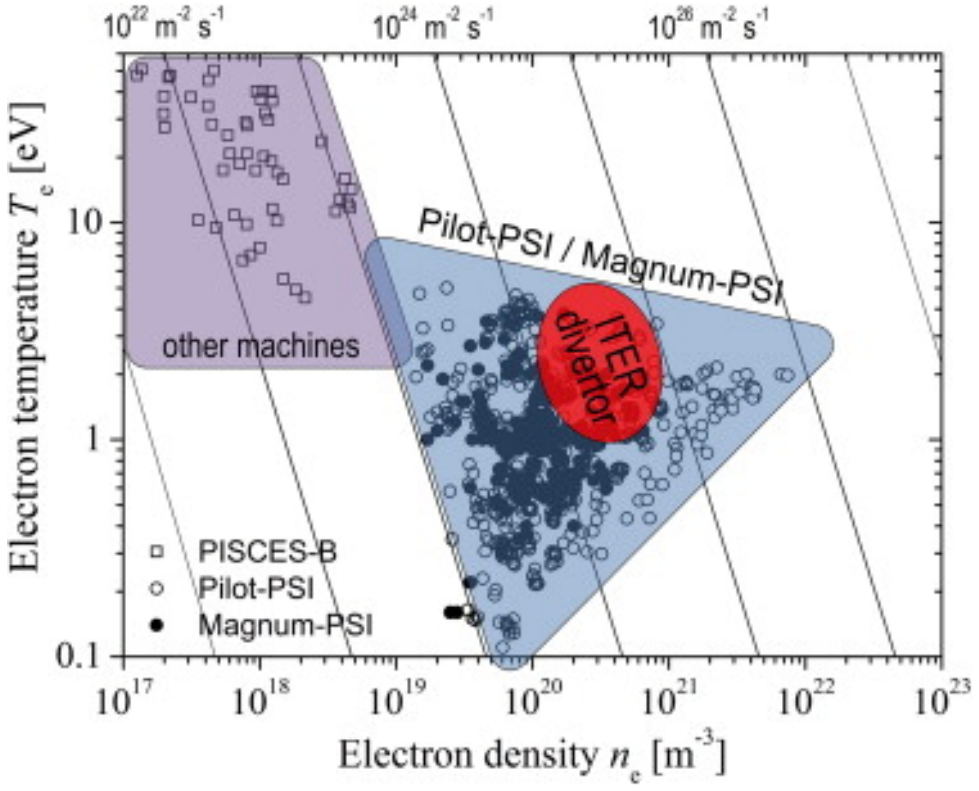

Figure 1.2: Operation range of Magnum-PSI compared to other experiments and to ITER divertor plasma temperature and density[12].

The target can be described as a tungsten sponge filled with liquid lithium, it has a porous core that connects the inner part, a liquid lithium reservoir, to the surface that is exposed to the plasma beam. The surface itself is porous in order to increase the capillary force.
When exposed to the plasma beam the target warms up and liquid lithium at the target surface evaporates and sputters to Magnum-PSI target chamber. The aim of the target design is to be always able to continuously refill the target surface with lithium coming from the reservoir thanks to capillary force.
The geometrical features of the target that has been simulated in this project are shown in figure 1.3.
As I will explain in chapter 3, lithium flow in the target and the thermal coupling of the target itself with the cooling/heating system will not be included in the simulations; the target in fact will be modeled as a lithium "sea", indefinitely deep; although, the geometrical features will be respected and quantities relative to the target, such as the total lithium influx and the plasma energy deposited to the target will be calculated.

1.2 Eunomia

In the divertor legs of a tokamak, the plasma temperature is typically below 10 eV[29] while neutral pressure can be several Pascals[28].
In these low temperature, high pressure conditions, the neutral particle density is similar to the plasma density and interaction between neutrals becomes important. In this regime, both plasma dynamics and a kinetic description of neutral species are crucial. Eunomia has primarily been developed to simulate neutral species in tokamak divertors and other experiments with similar conditions.
Eunomia is a code that, using Montecarlo techniques, solves the Boltzmann equations in and nearby low temperature plasma so calculating equilibrium density, temperature and flow velocity of the neutral species.
Eunomia is written in Fortran 95. Since Eunomia is a Montecarlo code, it requires a high amount of memory; for this reason it is normally run by a supercomputer array; parallelization techniques are

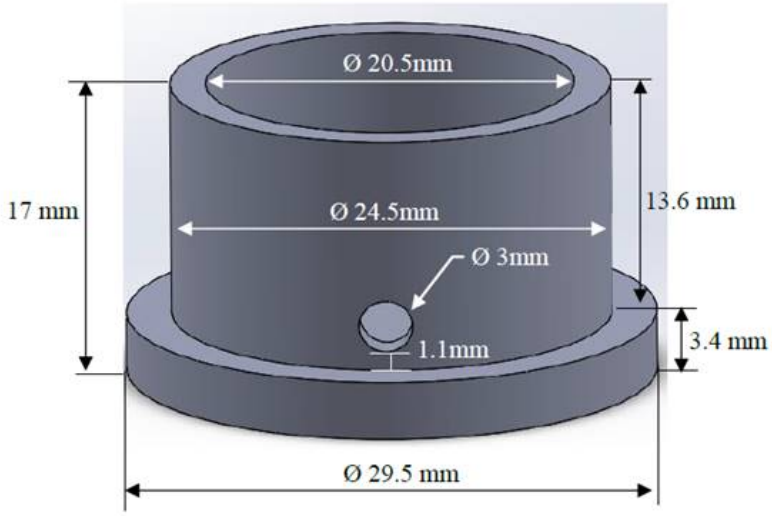

Figure 1.3: Geometrical description of the porous tungsten target filled with liquid lithium.

used to run the code.

1.2.1 Boltzmann equation

A brief introduction of the implemented method is now presented while fundamental explanation of equilibrium fluid dynamics[8] and of Montecarlo method[21] are available in literature.
The probability density function f(r,v,t) of species j is defined in a six dimensional space and describes the number of particles of a system that in a certain moment are in a infinitesimal element of the phase space $(r + \delta r, v + \delta v)$.

$$dN_j = f_j(\mathbf{r}, \mathbf{v}, t) d^3\mathbf{r} d^3\mathbf{v} \tag{1.1}$$

consequently the total number of particles is given by:

$$N_j^{tot} = \int d^3r \int d^3v f_j(\mathbf{r}, \mathbf{v}, t) \tag{1.2}$$

so the density in a infinitesimal volume element d^3r is

$$n_j(\mathbf{r}, t) d^3r = d^3r \int f_j(\mathbf{r}, \mathbf{v}) d^3v. \tag{1.3}$$

The Boltzmann equation for a certain specie j can be written as:

$$\left[\frac{\partial}{\partial t} + \mathbf{v} \cdot \nabla_r + \frac{\mathbf{F}_j(\mathbf{r}, \mathbf{v}, t)}{m} \cdot \nabla_v\right] f_j(\mathbf{r}, \mathbf{v}, t) = \left(\frac{\partial f_j(\mathbf{r}, \mathbf{v}, t)}{\partial t}\right)_{coll}, \tag{1.4}$$

where the l.h.s. of the equation is the convective derivative generalized to the density flux in the phase space (where $\mathbf{a}_j(\mathbf{r}, \mathbf{v}, t)$, the acceleration, has been substituted with $\frac{\mathbf{F}_j(\mathbf{r},\mathbf{v},t)}{m}$ and the r.h.s. is the collisional operator.
Eunomia is a steady state code that finds equilibrium solutions so all the time dependencies in equation 1.4 must be deleted.
The right hand side of equation 1.4 is called collisional operator; collisions are in fact what makes the convective derivative (left hand side) different from 0. Two different phenomena can introduce (or remove) particles from a phase space element $(\mathbf{r} + \delta\mathbf{r}, \mathbf{v} + \delta\mathbf{v})$ that is moving with the fluid: collisions and sources,

$$r.h.s. = \sum_i C_j(\mathbf{r}, \mathbf{v}, i), + S_j(\mathbf{r}, \mathbf{v}), \tag{1.5}$$

where $C_j(\mathbf{r}, \mathbf{v}, i)$ is the collisional net flow of j particles in the element due to collision with i particles

and $S_j(\mathbf{r}, \mathbf{v})$ is the source term. According to the previous assumptions there is no time dependence on those terms.
Assuming equilibrium conditions, substituting equation 1.5 in equation 1.4 it becomes:

$$\Big[\mathbf{v} \cdot \nabla_r\Big] f_j(\mathbf{r}, \mathbf{v}) = \sum_i C_j(\mathbf{r}, \mathbf{v}, i), + S_j(\mathbf{r}, \mathbf{v}), \tag{1.6}$$

where the force term as been deleted assuming that no external force is present in the system that is a solid assumptions since gravity is negligible and particles have no electric charge.

1.2.2 Eunomia flowchart

The aim of the Montecarlo method is solving equation 1.6 by lunching many test particles each one of them representing many real physical particles. The particles move in an initial standard background or in the one produced by the previous iteration. The behavior of test-particles and real particles is identical.
After a test particle is lunched it makes several collisions[1], after each collisions test particle state x_i changes to x_{i+1}, this process is called Markov chain. After a certain number N of collisions the neutral test particle X_i is lost (due to ionization, loss to the wall, etc.) and its simulation ends; then a new particle is lunched. In equation 1.7 the process is described:

$$X_i = (x_1, x_2, ..., x_N); \qquad \mathbf{X} = (X_1, X_2, ..., X_{N_{MAX}}). \tag{1.7}$$

Each relevant quantity Q, relative to particles X is then calculated upon averaging on the state assumed by the test particle:

$$Q = \frac{1}{N_{MAX}} \sum_{j=1}^{N_{MAX}} X_j. \tag{1.8}$$

Each physical quantity (density, velocity, energy) related with neutral particles can be calculated according to 1.8. Neutral and ion density velocity and energy sources can be calculated according to 1.8 as well; This is crucial in the coupling since Eunomia itself produces the loss and source terms needed to solve B2.5 equations and recalculate plasma background; obviously Eunomia only calculates plasma source terms that involve interactions with neutrals.
It must be underlined that, even if a test particle is free to move from a cell of the volume discretization to another, the average operation described in equation 1.8 is calculated cell by cell. So only the states assumed by a particle in a cell are considered.
After all the test particles are simulated a cycle is finished, a new background is calculated a new cycle can restart with a new background (standalone case) or the background can be passed to B2.5 (coupled run). The flowchart that has been described is sketched in figure 1.4a. In figure 1.4b the particle tracing is represented.
Lastly it must be reminded that Eunomia geometry is a 3D geometry even if the system that will be described has a cylindrical symmetry. The cylindrical symmetry simplifies B2.5 equations from 3D to 2D with the relative coordinates transformation. For a Montecarlo code though, since the test particles behave like real particles, simulating the real 3D volume comes easier than reducing the number of dimensions.
For those reasons all the simulations in Eunomia are carried on in a 3D space discretized by tetrahedrons and then the outcome of the simulation in projected in the 2D space covered by triangles.

1.3 B2.5

B2.5 is a finite difference code that computes plasma dynamics solving the Braginskii equations. When coupled (with Eunomia or other kinetics codes) it provides the kinetic code with the plasma background.

[1]The numerical procedure with which collisions are performed will not be discussed in this work; I will only limit to describe in next chapters the collisions considered in each simulations and how the rate coefficients have been calculated. The reader can find a careful description of random collision generation in Eunomia in Rob Wieggers thesis[31].

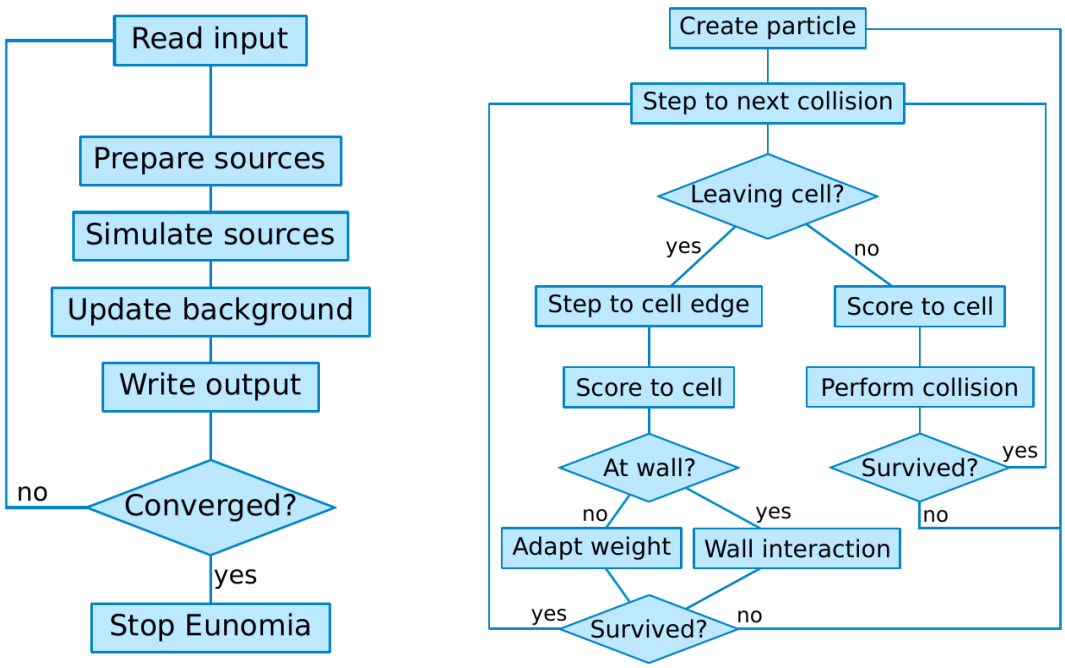

(a) Representation of Eunomia flowchart

(b) Representation of Eunomia particles tracing

Figure 1.4: Representation of Eunomia flowchart[31].

B2.5 can be used in both toroidal and linear geometry. In both scenarios, due to tokamak poloidal symmetry for tokamaks and axial symmetry for linear devices the equations can be reduced to two dimensions; in the linear case the two directions will be the radial and the axial direction.

1.3.1 The equations

[2] Like Eunomia, B2.5 is a steady state code, thus it does not include fast phenomena like the propagation of waves in plasma. For this reason electron density and momentum can be derived from ion dynamics using quasi-neutrality assumption and calculating plasma currents.
Therefore, the equations needed to solved the system will be $3 \cdot N_s + 2$, where N_s is the number of ion species considered: the three equation of ion dynamics (three for each ion species), the electrons energy equation and Ohm equation. Continuity equation for ions species i is:

$$\frac{\partial n_i}{\partial t} + \nabla \cdot (n_i \mathbf{v}_i) = S_{n_i}, \tag{1.9}$$

where n_i, v_i and S_{n_i} are the density, velocity and density source of species i.
The parallel momentum equation for ion is:

$$\frac{\partial}{\partial t}(m_i n_i v_{i\parallel}) + \nabla \cdot (m_i n_i \mathbf{v}_i v_{i\parallel}) = -\nabla_\parallel p_i - \left(\nabla \cdot \prod\nolimits_i\right)_\parallel + Z_i e n_i \nabla_\parallel \Phi + F_k + R_{i\parallel} + S_{m_i v_{i\parallel}}, \tag{1.10}$$

where p_i is the pressure of species i, $\prod_i$ is the viscosity tensor, Z_i is the charge of the ions species, e is the electron charge, Φ the potential, F_k is the Coriolis force, $S_{m_i v_{i\parallel}}$ is the parallel momentum source and $\mathbf{R}_i$ is the ion-electron friction.
The parallel momentum balance for electrons is provided by the Ohm equation:

$$j_\parallel = \sigma_\parallel \left(\frac{1}{e n_e} \nabla_\parallel n_e T_e + \frac{0.71}{e} \nabla_\parallel T_e - \nabla_\parallel \Phi \right), \tag{1.11}$$

where T_e is the electron temperature, σ the resistivity and n_e the electron density. The total plasma current instead is calculated by summing all its classical components:

$$\mathbf{j} = \mathbf{j}_{dia} + \mathbf{j}_{in} + \mathbf{j}_{vis} + \mathbf{j}_s + \mathbf{j}_\parallel, \tag{1.12}$$

[2] Equations of this sections are taken from [31]

where $\mathbf{j}_{dia}$ is the diamagnetic current, $\mathbf{j}_{in}$ is a contribution from inertia and gyro-viscosity, $\mathbf{j}_{vis}$ is the viscosity contribution due to charged particles interaction and $\mathbf{j}_s$ is the viscosity contribution due to neutral particles interaction.
Analogously the perpendicular velocity contribution are calculated the same way adding the $\mathbf{E}\times\mathbf{B}$ drift velocity $\mathbf{v}_\perp^a$:

$$\mathbf{v}_\perp = \mathbf{v}_\perp^a + \mathbf{v}_\perp^{dia} + \mathbf{v}_\perp^{in} + \mathbf{v}_\perp^{vis} + \mathbf{v}_\perp^s, \tag{1.13}$$

where the same of equation 1.12 has been used.
The energy equation for ions is:

$$\frac{\partial}{\partial t}\left(\frac{3}{2}n_iT_i+\frac{m_in_i}{2}\mathbf{v}_i^2\right)+\nabla\cdot\left[\left(\frac{5}{2}n_iT_i+\frac{m_in_i}{2}\mathbf{v}_i^2\right)\mathbf{v}_i+\prod_i\cdot\mathbf{v}_i+\mathbf{q}_i\right] = (Z_ien_i\mathbf{E}-\mathbf{R}_i)\cdot\mathbf{v}_i-Q_{ei}+S_{E_i} \tag{1.14}$$

while the energy for electrons is:

$$\frac{\partial}{\partial t}\left(\frac{3}{2}n_eT_e\right) + \nabla\cdot\left(\frac{5}{2}n_eT_e\mathbf{v}_i + \mathbf{q}_i\right) = -en_e\mathbf{E}\cdot\mathbf{v}_e + \mathbf{R}_i\cdot\mathbf{v}_i + Q_{ei} + S_{E_e}. \tag{1.15}$$

In equation 1.14 and 1.15 $\mathbf{q}_i/e$ are ions and electrons energy fluxes, Q_{ei} is the energy exchange from ions to electrons, and $S_{E_{i/e}}$ are the ion and electron energy source (not considering the electron contribution for the ions term and vice versa).

1.3.2 Coupled run flowchart

In the coupled run B2.5 acts as the master code. Starting from a standard background, B2.5 does a fixed number of iterations (typically 10 but there will be some exceptions). After those B2.5 iterations the plasma solutions are passed to Eunomia and converted in its 3D plasma background, then, one iteration is performed. As anticipated in section 1.2, Eunomia provides the source term for B2.5 equations (S_{n_i},$S_{m_iv_{i\|}}$ and $S_{E_{i/e}}$) as well as the new neutral background. Each quantity of Eunomia is projected in its 2D representation then, the information is passed to B2.5 rectangular grid (each B2.5 rectangular element is made of two Eunomia triangular element) and the cycle restarts with a new neutral background.
Since the Montecarlo code requires the generation of millions of test particles each iteration, parallelized runs are often needed in order to reduce computational time. In parallelized run one processor, the master processor, runs B2.5 while all the other processors run Eunomia. Parallelized run flowchart is shown in figure 1.5.

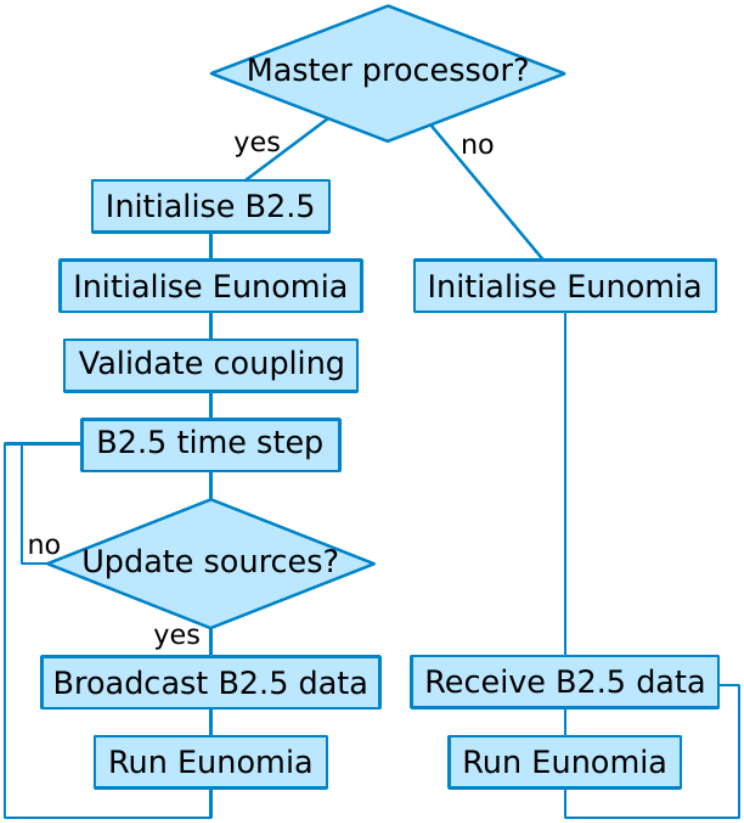

Figure 1.5: Flowchart of the coupled B2.5-Eunomia parallelized runs[31].

Chapter 2

Considered collisions

When modeling the influence of the lithium vapor cloud on plasma and vice versa, many collisions should be considered and careful understanding of the collisional radiative process is needed. The knowledge of the collisional radiative model will be fundamental to describe the radiative dissipation that is the main advantage of liquid metal divertors.
The main purpose of this chapter will be showing the physical collisions implemented to describe such a system; then all the steps that are needed to describe and predict every relevant plasma cooling channel will be described.
Collisions which include at least one neutral particle are implemented in Eunomia but play a huge role in B2.5; in fact most of those collisions provide B2.5 their relative plasma particles, momentum and energy sources. For those reasons the collisions implemented in Eunomia are described; a collisional radiative model is implemented and performed in the post-processing analysis, this analysis will be used as validation of the coupling itself. Further in the project is will be used as confirmation of the convergence.

2.1 Considered species and collisions

The species simulated in the coupled runs by B2.5 and Eunomia are showed in table 2.1.
I have chosen to not include Li^{2+} and Li^{3+} for both physical reasons. The physical reason is that second

B2.5	e^-, H^+, Li^+
Eunomia	H, Li, H_2

Table 2.1: List of species considered in the coupled B2.5-Eunomia simulations.

and third ionization energy for lithium are 76 and 122 eV respectively while electrons temperature in the divertor volume is always lower than 10 eV. More a more accurate upper energy limit of the model will be discussed later in this chapter.
Li^{2+} and Li^{3+} dynamic is normally implemented for codes that study lithium dynamic in the main plasma. If it is wanted to introduce Li^{2+} and Li^{3+} it has to be considered that Li^{2+} and Li^{3+} density, momentum and energy source term can not be provided by Eunomia, like for Li^+ but must be provided by B2.5.

The collisions implemented in Eunomia are showed in table 2.2. The one reported is the most complete list of collisions which also considers H_2 vibrational states. In table 2.2, if after a certain collision the test particle is lost, the test symbol of the particle is in red; if a collision generates a plasma particle loss the symbol of the plasma particle is blue, while if a collision generates a plasma source the symbol is relative to the source particle is green.

The simulation of H_2 vibrational states takes huge memory quantity, in fact 15 different vibrational states are implemented. The simulation of H_2 vibrational states can be deactivated if it is needed to

reduce the memory usage, however I have always chosen to activate the vibrational tool because it has been demonstrated to play an important role in energy transfer when plasma temperature is below 1 eV[5]. As I will show in the following chapters, the region in front of the target often has a plasma temperature below 1 eV.

On the lithium side, different collisions had been implemented with all the considered species. All the lithium test particles are simulated as ground state particles. The reason why this choice has been made will be described in section 2.1.1.
From table 2.2 it is also possible to see that for lithium, ionization is only provided by electrons, while for hydrogen charge exchange is relevant has well. This is consequence of the low temperature, heavy particles ionization for both particles is defined only in the keV range and there are no photons with such energy in the system described. Charge exchange collision for lithium ($Li + H^+ \rightarrow Li^+ + H$) is not relevant at this temperature range but for the Li_{2p} state; nevertheless,as I will show in the next section, Li_{2p} population is never relevant.
To understand how plasma cooling is calculated in Eunomia excitation and elastic collision can be taken as an example. The lithium (or hydrogen) test particle is not lost after making one of those collisions, it will in fact proceed to the next collision, the only effect of those collisions is the momentum exchange and plasma energy loss that will be considered in the following B2.5 iteration. Cooling channels will be carefully described in section 5.2.

2.1.1 Fast reactions modeling

As described in the previous chapter and in appendix B, in Eunomia each neutral specie is simulated and each possible collision frequency is calculated from the relative rate coefficients. H* modeling in B2.5-Eunomia simulations has already been discussed in [31] and will not be discussed in this project since hydrogen coupling has already been validated.
On the other hand, Li* in Eunomia is assumed to ionize or de-excite to the ground state instantaneously. For this reasons, reactions like *electron impact ionization* or *recombination* are are considered only for their relative momentum exchange and electron energy sink.
Those rate coefficients are calculated from databases[1] as function of the temperature of each specie averaging on every atomic state represented by the test particle; this is the so called *"fast reaction modeling"*.
This treatment implies that the only two neutral lithium atomic state considered are the one that will be called ground state (which electron configuration is $[He]2s$) and the first excited state ($[He]2p$). Can the system, under this assumption, describe the system with high accuracy? The analysis of the collisional radiative model will answer this question.

2.2 The collisional radiative model

The possibility of solving the collisional radiative model (CRM) for each species simulated in B2.5-Eunomia is available and could be performed by a specific tool. Nevertheless, for memory issues, it has been decided to not use this tool; the simulations indeed, as described in chapter 4 already requires a huge amount of memory and time so it has been solved only in the post-processing.
The collisional radiative model has been studied to understand if the three states description (Li_{2s}, Li_{2p}, Li^+), implemented in B2.5-Eunomia, is enough to describe the physics of the system.
It has been decided to not consider any excited state of Li^+ since this specie has a noble gas electron configuration so the shell is complete and so the energy gap between the ground state and the first excited state about 10 eV, twice the energy gap between Li ground state and first excited state.
The prediction of the three states CR model will then be compared to a complete CR model found in the literature to quantify the level of agreement.

[1] aggiungere qualche database

	Collisions	Collision type	data
0	$e^- + H(2s) \rightarrow e^- + H^+ + e^-$	Electron impact ionization	[31]
1	$e^- + H(2s) \rightarrow e^- + H^*$	Electron impact excitation	[31]
2	$H^+ + H(2s) \rightarrow H^+ + H^*$	Heavy particle excitation	[31]
3	$H^+ + H(2s) \rightarrow H^+ H^+ + e^-$	Heavy particle ionization	[31]
4	$H^+ + H \rightarrow H H^+$	Charge exchange	[31]
5	$e^- + H_2 \rightarrow e^- + H + H$	Dissociation	[31]
6	$H + H \rightarrow H + H$	Elastic Collision	[9]
7	$H_2 + H_2 \rightarrow H_2 + H_2$	Elastic Collision	[9]
8	$H + H_2 \rightarrow H + H_2$	Elastic Collision	[9]
9	$e^- + H^+ \rightarrow H$	Recombination	[2]
10	$e^- + H^+ + H_2 \rightarrow H + H + H$	Molecular activated recombination	[31]
11	$e^- + H^+ + H_2 \rightarrow H + H + H$	Molecular activated recombination	[3]
12	$H^+ + H \rightarrow H^+ + H$	Elastic Collision	[2]
13	$H^+ + H_2 \rightarrow H^+ + H_2$	Elastic Collision	[2]
14	$e^- + H^+ + H_2 \rightarrow H + H + H$	MAR for vibrational state	[31]
15	$H_2 + H_2 \rightarrow H_2 + H_2$	Heavy particle excitation	[9]
16	$H + H_2 \rightarrow H + H_2$	Heavy particle excitation	[9]
17	$H^+ + H_2 \rightarrow H^+ + H_2$	Heavy particle excitation	[2]
18	$e^- + H_2 \rightarrow e^- + H_2$	Electron impact excitation	[31]
19	$e^- + H_2 \rightarrow e^- + H_2$	Electron impact excitation	[31]
20	$e^- + H_2 \rightarrow H + H^-$	Dissociative ionization	[31]
21	$Li + Li \rightarrow Li + Li$	Elastic Collision	[9]
22	$Li + H \rightarrow Li + H$	Elastic Collision	[9]
23	$Li + H_2 \rightarrow Li + H_2$	E. C. for vibrational state	[9]
24	$e^- + Li \rightarrow e^- + Li^+ + e^-$	Electron impact ionization	[9]
25	$e^- + Li_{2s} \rightarrow e^- + Li_{2p}$	Electron impact excitation	[9]
26	$e^- + Li_{2s} \rightarrow e^- + Li_{3p}$	Electron impact excitation	[9]
27	$Li + H^+ \rightarrow Li^+ + H$	Charge exchange	[9]
28	$Li + H^+ \rightarrow Li + H^+$	Elastic collision	[9]
29	$Li^+ + e^- \rightarrow Li$	Recombination	[9]
30	$Li^+ + H \rightarrow Li^+ + H$	Elastic collision	[9]

Table 2.2: List of collisions implemented in Eunomia. If a plasma loss/source is related to to a reaction the particle specie is colored blue/green. Neutral test particles which are lost after a reaction a reported in red.

Collision type	Reaction	Frequency	Symbol in the equations
Excitation	$e^- + Li_{2s} \rightarrow e^- + Li_{2p}$	$f^{i-e}_{exc2p2s}$	A
Ionization	$e^- + Li_{2s} \rightarrow e^- + Li^+ + e^-$	f^{i-e}_{Ion2s}	B
De-excitation	$Li_{2p} \rightarrow Li_{2s} + \gamma$	$f_{DeExc2p2s}$	C
Recombination	$e^- + Li^+ \rightarrow Li_{2s}$	f^{i-e}_{Rec2s}	D
Recombination	$e^- + Li^+ \rightarrow Li_{2s}$	f^{i-e}_{Rec2p}	E
Ionization	$e^- + Li_{2p} \rightarrow e^- + Li^+ + e^-$	f^{i-e}_{Ion2p}	F
Ionization	$e^- + Li^+ \rightarrow e^- + Li^{2+} + e^-$	f^{i-e}_{2Ion}	G
Recombination	$e^- + Li^{2+} \rightarrow Li^+$	f^{i-e}_{2Rec}	H

Table 2.3: List of symbols pointing to collisional frequencies that will be used in the collisional radiative model description. In the first part the reactions considered in the three state model, which are the same implemented in the simulation, are reported. In the second part the reactions added to the four state model are reported.

2.2.1 The equations of the model

The considered CR model assumes no lithium flux, gain or losses in the model, so the continuity equation becomes equation 2.1:

$$\frac{\partial}{\partial t}\left(Li_{2s} + Li_{2p} + Li^+\right) = 0. \tag{2.1}$$

In the following equations I will use symbols indicating to collision frequencies. The collision frequencies and their relative symbols in the equation are shown in table 2.3
Lithium three species CR model, that describes the same lithium system simulated, is described by the matrix equation 2.2.

$$\begin{pmatrix} -A-B & C & D \\ A & -C-F & E \\ B & F & -D-E \end{pmatrix} \begin{pmatrix} Li_{2s} \\ Li_{2p} \\ Li^+ \end{pmatrix} = \begin{pmatrix} \frac{\partial Li_{2s}}{\partial t} \\ \frac{\partial Li_{2p}}{\partial t} \\ \frac{\partial Li^+}{\partial t} \end{pmatrix} \tag{2.2}$$

In this equation Li_{2s}, Li_{2p} and Li^+ represent the three lithium abundances. All the frequencies depend on electrons density, electrons and lithium temperature but not on lithium density. The independence of the frequencies lithium density guarantees the three equations system to be linear on lithium density. In a isolated system in equilibrium condition equation 2.2 turns into 2.3.

$$\begin{pmatrix} -A-B & C & D \\ A & -C-F & E \\ B & F & -D-E \end{pmatrix} \begin{pmatrix} Li_{2s} \\ Li_{2p} \\ Li^+ \end{pmatrix} = \begin{pmatrix} 0 \\ 0 \\ 0 \end{pmatrix} \tag{2.3}$$

This is a linear equation that always admits solution different to zero. The lithium mass conservation (2.1) is mathematically reflected on the determinant of the matrix that is always equal to zero.
Since only two out of the three equations are independent, the solution of the system is a vector that provides the relative abundances. The vector in described by equation 2.4 and 2.5.

$$Li_{2s} = \frac{DC + CE + DF}{AD + AE + BE} Li_{2p} \tag{2.4}$$

$$Li^+ = \frac{AF + BC + BF}{AD + AE + BE} Li_{2p} \tag{2.5}$$

The system can be closed substituting one of the equations with a third independent equations that provides the density normalization:

$$Li_{2s} + Li_{2p} + Li^+ = 1. \tag{2.6}$$

Substituting equation 2.4 and 2.5 into 2.6, equation 2.7, that closes the system, is obtained:

$$\mathrm{Li}_{2p} = \frac{AD + AE + BE}{(A+B)(E+F) + C(B+D+E) + D(A+F)}. \tag{2.7}$$

The three states CR model is now ready to be solved for different neutral and plasma conditions.

2.2.2 CR model parameters

In this section I will discuss how the matrix parameters have been calculated in different plasma conditions.

As reported in the previous section, the only ionization reaction considered is electron impact ionization. Also for excitation the only considered reaction is electron impact excitation because heavy particles lithium excitation is neglectable in few eV temperature range and because photons cannot be implemented as test particles in Eunomia. Heavy particles collisions will play a role only in lithium thermalization and momentum exchange.
The approximation of not considering photons re-absorption implies that I have not considered the possibility of a photon, generated after a de-excitation process, to impact on a ground state Li particle and excite it. This approximation does not lead to lack of physical description of the system because this reaction does not lead to any cooling channel since the absorption of the photon is followed by a new photon emission. The only effect of this emission→re-absorption process is to delay the photons absorption to the wall; the energy relative to the $2p \rightarrow 2s$ transition is lost by the system anyway since the only possibilities are absorption and re-emission by other neutral particles or absorption by the wall.
The photons in fact cannot be re-absorbed by the plasma itself since the plasma electron frequency, calculated as

$$\omega_{e,p} = \left(\frac{n_e q^2}{m_e \varepsilon_0}\right)^{0.5}, \tag{2.8}$$

for a plasma density of $10^{20}\,\mathrm{m}^{-3}$ is about $10^{11}\,\mathrm{s}^{-1}$ while the frequency of emitted photons of the lithium $2p \rightarrow 2s$ transition at 671 nm is $2 \times 10^{15}\,\mathrm{s}^{-1}$, so, since the radiation frequency is order of magnitude higher than electron plasma frequency, the plasma is transparent to this radiation.
To conclude the overview on photons re-absorption I remind that this reaction has an effect on the Li_{2s}/Li_{2p} ratio. The effect of this approximation on the ratio will be discussed in section 2.3.

Since in the described system lithium particles are emitted from the target at target temperature (it will be described in chapter 3) lithium temperature will always be lower than plasma temperature. Further, even considering a completely thermalized system, since lithium mass is about 14000 times bigger than electron mass, lithium speed is more than 2 order of magnitude lower than electrons'. For those two reasons Li-e^- collisions can be described as fast electrons impinging on a frozen lithium background; therefore collisions frequency will be independent on lithium temperature.
Following those considerations, electron-ion collision frequencies for ionization and excitation has been calculated as follow:

$$\begin{aligned} f^{e-i}_{Ion2s} &= n_{Li2s}\langle\sigma_{Ion2s} v_e\rangle, \\ f^{e-i}_{Ion2p} &= n_{Li2p}\langle\sigma_{Ion2p} v_e\rangle, \\ f^{e-i}_{Exc2s2p} &= n_{Li2s}\langle\sigma_{Exc2s2p} v_e\rangle, \end{aligned} \tag{2.9}$$

where σ_* are the cross sections, v_e is the electron speed, n_* are the densities and f^{e-i}_* are the three collision frequency of an electron impinging on a lithium particle. In equation 2.9 the symbol $\langle\rangle$ refers to average over electrons velocity distributions; since we are considering thermal equilibrium conditions the distributions is assumed to be Maxwell-Boltzmann.
But matrix parameter are the frequencies relative to lithium particles, not electrons, so are calculated as follow:

$$\begin{gathered} A = f^{i-e}_{Exc2s2p} = f^{e-i}_{Exc2s2p}\frac{n_e}{n_{Li2s}} = n_e\langle\sigma_{Exc2s2p} v_e\rangle, B = f^{i-e}_{Ion2s} = f^{e-i}_{Ion2s}\frac{n_e}{n_{Li2s}} = n_e\langle\sigma_{Ion2s} v_e\rangle, \\ F = f^{i-e}_{Ion2p} = f^{e-i}_{Ion2p}\frac{n_e}{n_{Li2p}} = n_e\langle\sigma_{Ion2p} v_e\rangle, \end{gathered} \tag{2.10}$$

that are independent on lithium density as required.
The three cross sections have been taken from IAEA Amdis Aladdin database[2] and, to perform the integration, had been fit by polynomial functions of the logarithm of the cross sections. Cross sections are shown in figure 2.1.
Since for a Maxwell-Boltzmann distribution

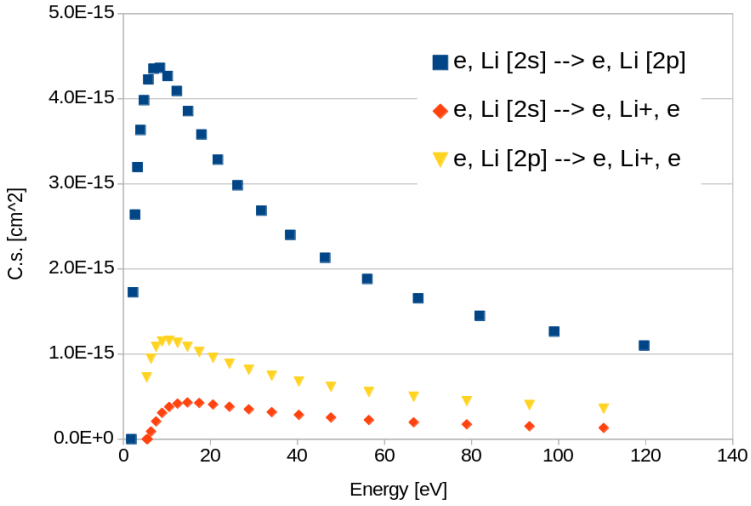

Figure 2.1: Considered cross section from IAEA database

$$f(v) = 4\pi \left(\frac{m_e}{2\pi k_B T_e} \right)^{3/2} v^2 e^{-\frac{m_e v^2}{2K_B T_e}}, \tag{2.11}$$

the rate coefficient $\langle \sigma v \rangle$ is calculated as:

$$R = \langle \sigma v \rangle = \frac{8\pi}{m_e^{1/2}} \left(\frac{1}{2\pi k_B T_e} \right)^{3/2} \int_0^\infty \sigma(\varepsilon) \varepsilon e^{\frac{-\varepsilon}{k_B T_e}} d\varepsilon. \tag{2.12}$$

The rate coefficients for electron temperature from 0 to 12 eV have been calculated integrating expression 2.2.2 till 120 eV, so 10 times the higher temperature considered, using the trapezes method and dividing the total energy interval in 480 intervals of 0.25 eV each.

De-excitation frequency is given by the first Einstein coefficient "A" that corresponds to spontaneous emission. Stimulated emission have not been considered since photons-particle interaction as been neglected as it has been described before.

Recombination rate coefficients have been taken directly from the ADAS database[3]. Since the recombination rate coefficient depends both on electron temperature and density and the rate coefficients where given only for certain values, the recombination rate coefficients for arbitrary T_e and n_e values has been calculated performing a 2D weighted average on the closer database-given temperatures and densities.
An overlook on the method considered is given by figure 2.2. Let's consider a temperature T_c and a density d_c such that $T_i < T_c < T_{i+1}$ and $d_j < d_c < d_{j+1}$, where T_i,T_{i+1},d_j and d_{j+1} are the closer temperatures and densities for which recombination rate coefficients are given. If $a = T_c - T_i$, $b = T_{i+1} - T_c$, $c = d_c - d_j$ and $e = d_{j+1} - d_j$, the rate coefficients at $T = T_c$ and $d = d_c$, $R(T_c, d_c)$ is calculated as:

$$R(T_c, d_c) = \frac{1}{c+e} \left[e \frac{bR(T_i, d_j) + aR(T_{i+1}, d_j)}{a+b} + c \frac{bR(T_i, d_{j+1}) + aR(T_{i+1}, d_{j+1})}{a+b} \right]. \tag{2.13}$$

[2] Three references to be added here
[3] Add here the citation

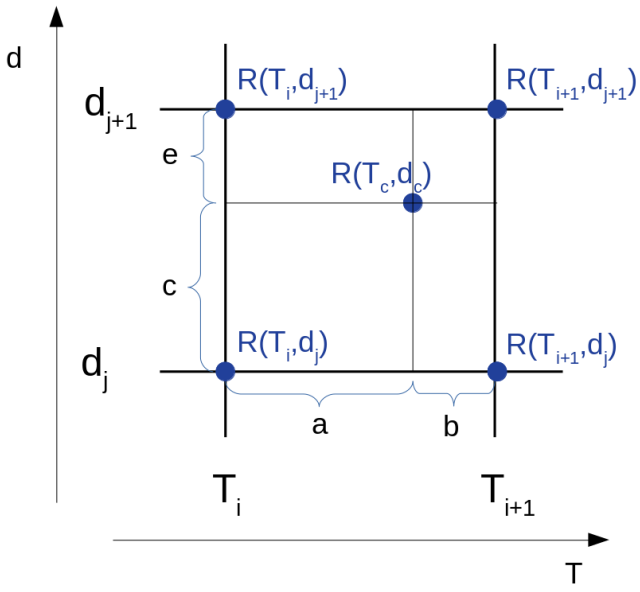

Figure 2.2: Sketch of the average method for recombination rate coefficients.

The calculated rate coefficients for $n_e = 10^{20}\,\mathrm{m}^{-3}$, that are all calculated as in equation but for recombination, are shown in figure 2.3. In figure 2.3 also some rate coefficients for the previously described reactions are shown together with some that will be discussed later.

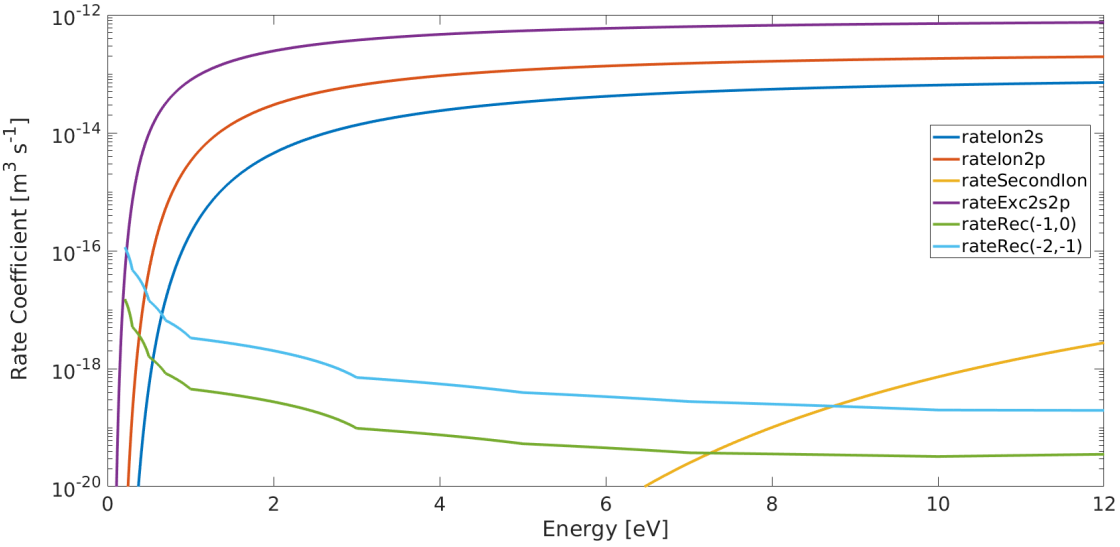

Figure 2.3: Calculated rate coefficients. $\mathrm{rateIon_2s}$ and $\mathrm{rateIon_2p}$ are the ionization rate coefficient for ionization from the 2 s and 2 p state lithium state, $\mathrm{rateExc_2s_2p}$ is the considered excitation rate coefficient, $\mathrm{rateRec}(-1,0)$ and $\mathrm{rateRec}(-2,-1)$ are the recombination rate coefficient from Li^+ to Li and from Li^{2+} to Li^+ respectively, rateSecondIon is the rate coefficient for second ionization.

2.3 Outcome and limits of the model

Once the electrons density is fixed to $10^{20}\,\mathrm{m}^{-3}$ equations 2.4, 2.5 and 2.7 can be solved for different electrons temperature.
Results are shown in figure 2.4. From figure 2.4 it is possible to make some considerations about the validity of the three state model.

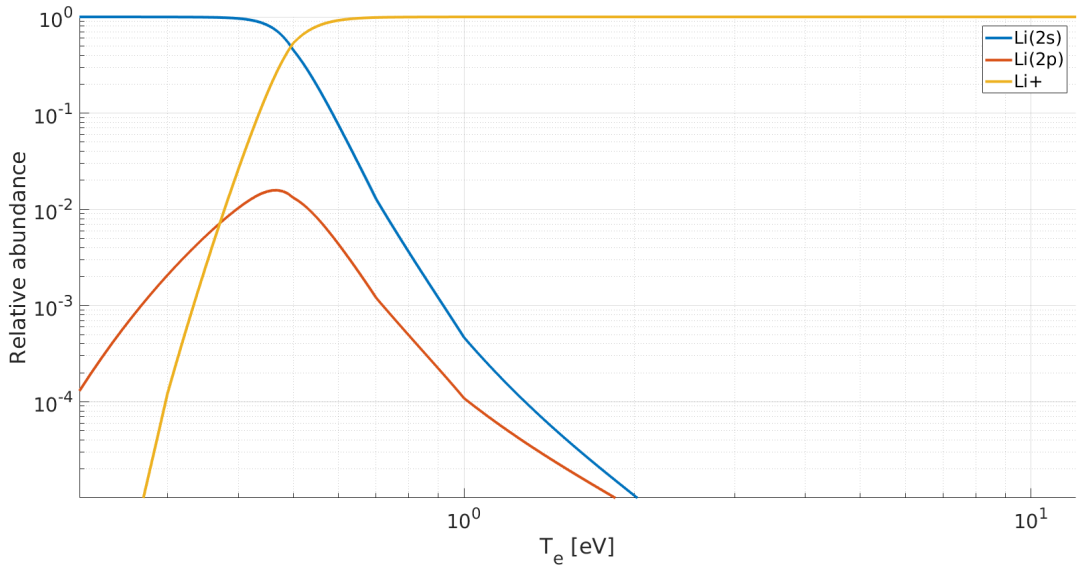

Figure 2.4: Outcome of the three species CR model for $n_e = 10^{20}\,\mathrm{m}^{-3}$.

Firstly figure 2.4 shows that, even if the first ionization energy is higher than 5 eV, Li^+ population is already dominant even at 1 eV. This will forced me also to check when Li^{2+} becomes relevant even if the second ionization energy is about 80 eV.
The transition from neutral to ions dominance occurs very rapidly increasing electrons temperature, so even thermal gradient con can produce huge gradient in species abundances.
Lastly it is possible to notice that Li_{2p} abundance is relevant, compared to Li_{2s} abundance only for temperature higher than 1 eV. It is also shown that Li_{2p} comparable to the ground state abundance only when the total neutral abundance is negligible. More generally it is possible to say that when the abundance of the excited states is higher than the ground state, neutrals themselves are not relevant. The effect on cooling, not considering higher excited states, is that $excitation - radiation$ processes for higher energy states are not calculated. Nevertheless, those cooling channels are proportional to the population abundance[4] and those high energy population are never relevant as it is shown in figure 2.4. Quantitative estimation on plasma cooling are reported in chapter **??**.

To calculate the upper energy limit of the three state model,developing a 4 state model, that considers also Li^{2+} population is needed.
Keeping all the equilibrium and mass conservation assumptions, the model is described by equation 2.14 were the convention showed in table 2.3 has been applied.

$$\begin{pmatrix} -A-B & C & D & 0 \\ A & -C-F & E & 0 \\ B & F & -D-E-G & H \\ 0 & 0 & G & -H \end{pmatrix} \begin{pmatrix} \mathrm{Li}_{2s} \\ \mathrm{Li}_{2p} \\ \mathrm{Li}^+ \\ \mathrm{Li}^{2+} \end{pmatrix} = \begin{pmatrix} 0 \\ 0 \\ 0 \\ 0 \end{pmatrix}. \tag{2.14}$$

Again the four equation are not independent so one of them has been replaced with the normalization

$$\mathrm{Li}_{2s} + \mathrm{Li}_{2p} + \mathrm{Li}^+ + \mathrm{Li}^{2+} = 1. \tag{2.15}$$

The solution of equation 2.14 is shown in figure 2.5 and are represented by the continuous lines while the results given by the three state model is represented by the dashed lines.
Figure 2.5 shows that there are no differences between 3 three and four species models as long as the electron temperature is kept below 7 eV. This has been the high energy limit of my simulations.

[4]The energy dissipated per unity of volume and time is calculated as: $\varepsilon_{cool} = n_* \Delta(E) A$ where A is the Einstein coefficient and $\Delta(E)$ the energy difference between the two states and n_* the density of the "*" population.

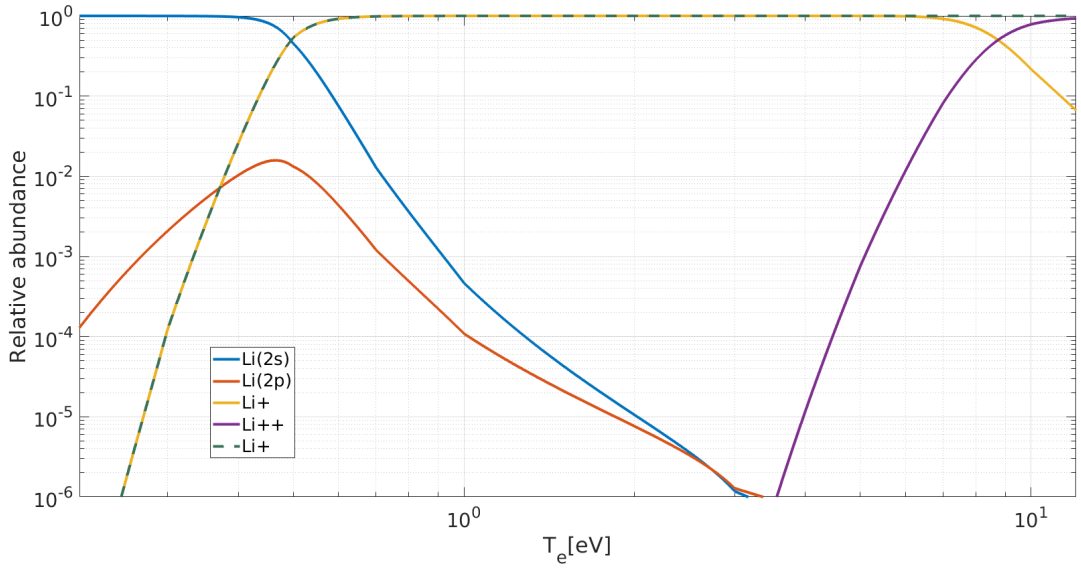

Figure 2.5: Outcome of the four species CR model [continuous lines] and comparison with Li^+ abundance in the three species CR model [dashed line].

Chapter 3

Geometry and Boundary Conditions

3.1 Considered Geometries

The entire real geometry of Magnum-PSI has been described in section 1.1. Starting from the experiment geometry, three different geometries have been created to study different phenomena and different experimental scenarios.
In all the following geometries cylindrical symmetry is assumed so plasma dynamic can be described in a 2D domain, neutral dynamic is simulated in a 3D domain. Once the borders of the 2D (r-z) domain are defined, the *triangle* tool, available in the package, builds the mesh.
The discretization of the simulated volume is divided into *internal grid* and *external grid*. The *internal grid* is the central part of the cylinder where the plasma beam is; it defines the region where B2.5 solves the plasma equations with a final element method. As reported in section 1.3 B2.5 elements are rectangular elements since the total B2.5 domain is a 2D rectangle. On the other hand Eunomia works on a 3D volume so tetrahedrons are needed to fill the 3D space; the 2D representation of the tetrahedrons are triangles. Eunomia internal grid is generated by dividing B2.5 elements in 2 or 4 triangles cutting the rectangles along the diagonals; an example is shown in figure 3.1b.
The external region is defined only for Eunomia and describes all the region of the experiment out of the plasma beam. Also here the triangles are the 2D representation of the 3D tetrahedrons.

Magnum-PSI target chamber

For numerical reasons it has been decided, for a large part of the project, to study only Magnum-PSI target chamber volume.
Studying the entire Magnum-PSI volume would required more than doubled the amount of cells in the domain, consequently increasing the computational cost. Furthermore, the majority of lithium-plasma interaction takes place in the first centimeters from the target; lithium density then rapidly decreases along the plasma beam as will be shown in the next chapters. For those reasons all the physically interesting phenomena are visible in the target chamber; the target chamber can be seen as the inner box of a vapor box.
In figure 3.1a and 3.1b Magnum-PSI target region mesh is represented. It is a 2D representation of Magnum-PSI chamber; the 3D representation is obtained rotating figure 3.1a around $r = 0$ axis.
The black part of 3.1a is the internal grid; the plasma enters the target chamber from the bottom left part of figure 3.1a while the target is positioned at z =0.029 m. The z =0 m axis has been chosen to be the Thompson scattering position, all other positions are consequent to this choice. The white part over the internal grid represents the target holder and is actually out of the simulation volume. The pumps in Magnum-PSI are located in the back part of the target chamber, in the simulations they are located at z =0.667 m.
It has been decided to divide the internal region in $32 \cdot 64 = 2048$ rectangular cells to have an accurate discretization. This means that 4096 out of the total 4895 Eunomia cells are in the internal grid.

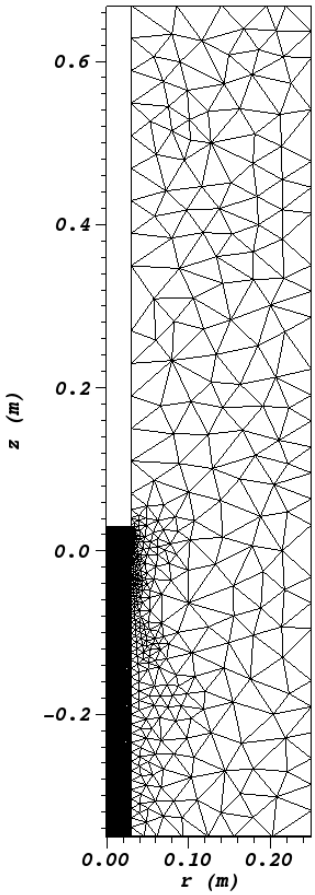

(a) Mesh of the Magnum-PSI target chamber.

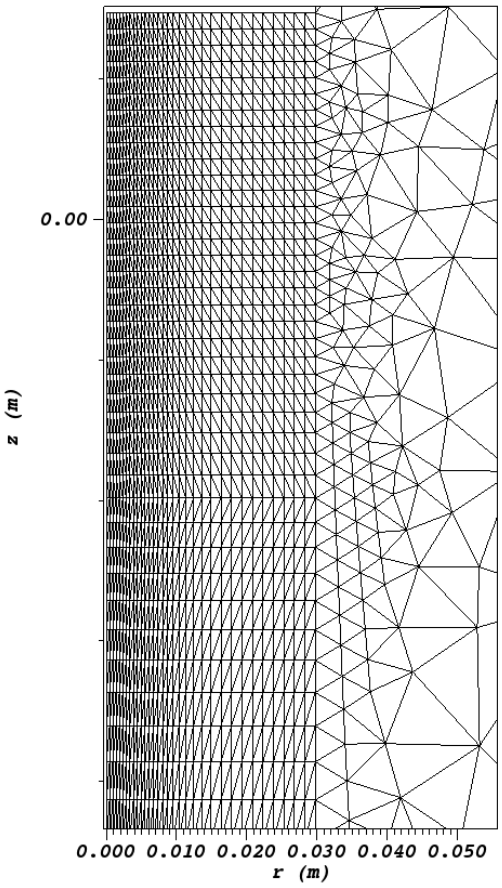

(b) Portion of the internal grid and external grid close to the target.

Figure 3.1: Entire and partial 2D view of B2.5-Eunomia discretization of the Magnum-PSI target chamber volume.

Total Magnum-PSI geometry and the vapor box

The total Magnum-PSI geometry has been built to compare the simulations of the coupled runs with the results of the standalone runs already made[6][20]. Magnum-PSI geometry is shown in figure 3.2.
Magnum-PSI geometry is similar to the one of possible vapor-box since the walls divide the total experiment volume into smaller chambers. For this reasons the vapor box simulations will be performed starting from Magnum-PSI geometry moving or adding the walls and will be discussed in chapter 7

3.2 Boundary conditions

Neutral boundary conditions are defined for Eunomia in each wall of the simulated geometry while plasma boundary conditions for B2.5 are defined only for the internal grid.

3.2.1 Neutral boundary conditions

Boundary conditions for Eunomia are divided in two types:

- boundary conditions that define a particle source from a wall
- boundary conditions that define what happens to a test particle when it hits a wall.

The first type boundary conditions define sources for simulated test particles. Test particles are launched from the wall and the weight of launched test particles is proportional to the intensity of the particles income from the wall Γ_{in}.

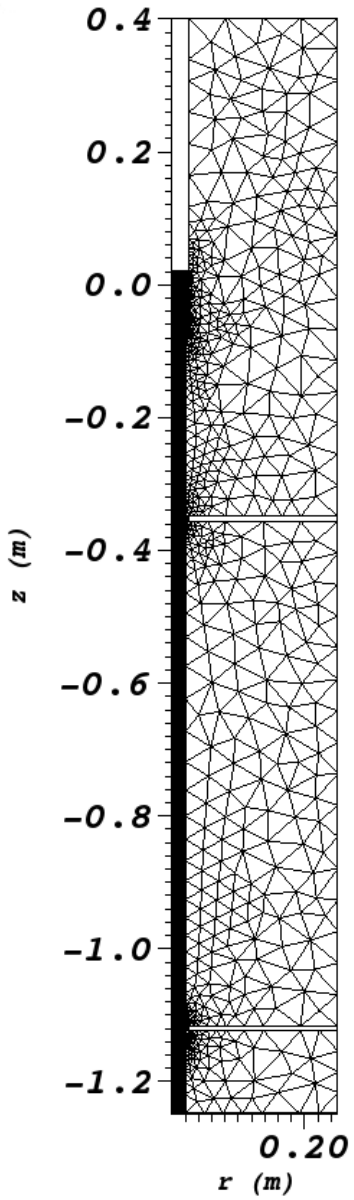

Figure 3.2: Total Magnum-PSI geometry. The total magnum geometry is divided in three parts. The source chamber is the lower part of the image is the chamber where the plasma beam is emitted; then the plasma beam passes through the heating chamber and hits the target in the target chamber.

For those reasons when a wall source is modeled what it is really fixed is the influx from the target Γ_{in}, that generates the test particles, not the total flux $\Gamma_{tot} = \Gamma_{in} - \Gamma_{out}$. The wall generated test particles can also, after some collisions, come back to the wall where they had been generated and there being reabsorbed this limiting the in total lithium flux. This approach is very convenient for target modeling, as will be shown, because the total observed flux of particles from the simulation will also consider redeposition.
In the described system the only boundaries that are sources of neutral particles are the target, that is a Li source, and the entrance to the chamber that is a H and H_2 source.

Particles wall sources

The lithium target that will be exposed to Magnum-PSI plasma will be a 3D-printed tungsten sponge filled with liquid lithium as described in 1.1.
By the modeling point of view, the target is seen like as a lithium "sea" indefinitely deep. The limits of this assumption will be discussed later.
Lithium outcome from the target had been recently modeled [6], its modeling is composed of two physically different sources: evaporation and sputtering.

Evaporation has been modeled using the Langmuir evaporation rule[18]:

$$\Gamma_{evap,\mathrm{Li}} = \frac{p_{\mathrm{Li}} - p_a}{\sqrt{2\pi m_{\mathrm{Li}} k_B T_{surf}}}, \tag{3.1}$$

where p_{Li} is the lithium vapor pressure, p_a is the environment pressure above lithium surface (both expressed in Pa), m_{Li} is the lithium particles mass that is approximated to $6.938\,\mathrm{a\,m\,u}$, k_B is the Boltzmann constant and T_{surf} is the surface temperature.
Lithium vapor pressure is calculated according to the empirical formula 3.2 [13],

$$\ln(p_{\mathrm{Li}})[\mathrm{Pa}] = 26.89 - \frac{18880}{T_{surf}} - 0.4942\ln(T_{surf}). \tag{3.2}$$

Lithium influx is highly dependent on target temperature as it is shown in figure 3.3. The target temperature range of my simulation, and of the following experiments will be between 500 and 1000 K; as figure 3.3 shows there are eight orders of magnitude between plasma flux at 500 and 1000 K, so I expect the simulations to be highly dependent on T_{surf}.
Lastly I have to remember that the minimum target temperature I should simulate is the evaporation temperature $T_{evap} = 454\,\mathrm{K}$.
The target temperature profile is chosen before each simulation and it does not change during the simulation. The target temperature can be set for each facing target cell, so from each cell border a certain amount of lithium test particles are generated and simulated.
Lithium particles coming out from the target by evaporation have the same energy they had in the target; for this reason, supposing thermal equilibrium in the liquid target, it has been decided to generate the test particle with a Maxwell-Boltzmann velocity distribution:

$$f(v) = 4\pi\left(\frac{m_{Li}}{2\pi K_B T_{surf}}\right)^{3/2} v^2 \exp\left(-m_{Li}v^2/2K_B T_{surf}\right). \tag{3.3}$$

The direction of the generated test particles has been settled to be a cosine-like distribution where $0\,^\circ$ correspond to the direction orthogonal to the target.

A more accurate description of the real physical system would require to update the target temperature according to the plasma heat deposited to the target, at every B2.5-Eunomia cycle. The quantities that would be required for such a description are: the heat flux to the target, that can be easily calculated from the plasma density and temperature profiles, and the heat transport through the tungsten-lithium target (described in section 1.1) and its thermal coupling with the target cooling (or heating) system. Such a description is out of the scope of this project since I mainly focused on the coupling of the

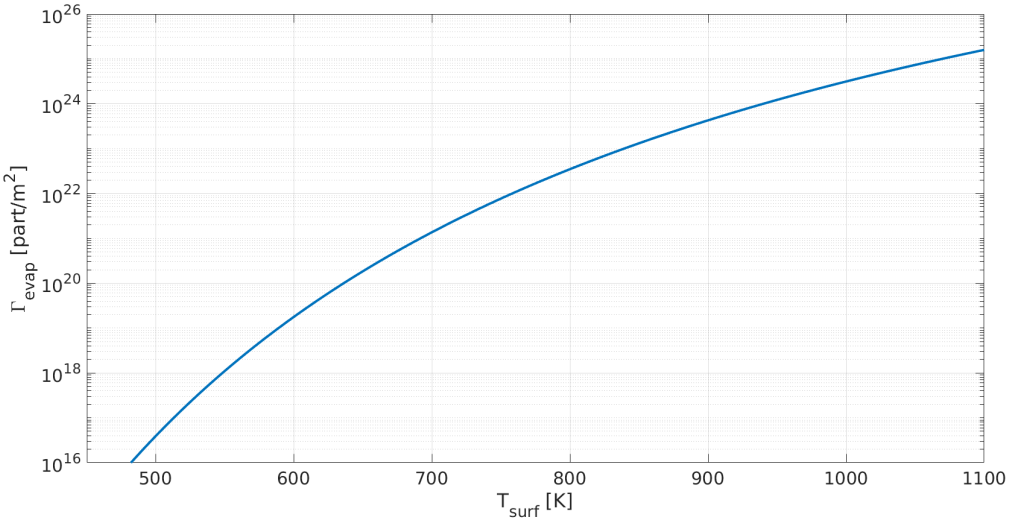

Figure 3.3: Lithium evaporation flux from the target according to Langmuir evaporation law.

codes itself and not on the physics of a specific target. Furthermore, a self consistent description of target temperature could lead to convergence problem. In fact, using liquid lithium targets, an oscillatory behavior of lithium flux was observed in a recent experimental campaign at DIFFER [30]. This behavior, whose reasons are still debated, has been linked with the thermal coupling of the lithium target and, since it is not a stationary phenomena, it could affect the predictability of B2.5-Eunomia solutions that are steady state solutions.
For all those reasons I've chosen to keep the target temperature profile constant in each simulation. During the experimental validation campaign the target temperature can be set with cooling or heating systems to match the simulation values, or, on the other way around, the simulation input target temperature profile can be set consistently with the experimental data from pyrometry.

When a surface atom is hit by a fast particle momentum and energy are transfered from the hitting particle to the surface one. If the energy component normal to the surface transferred to this atom is larger than a value known as the surface binding energy (SBE) then the atom will overcome its bound state on the surface and be ejected. The threshold energy E_{th} (higher than the SBE) is a slightly higher than the SBE. This process is known as physical sputtering and is a particles source in the model I want to describe. The sputtering model had been implemented in Eunomia [6] according to [1] modeling.
The *sputtering yield* is defined as:

$$Y = \frac{\Gamma_{sput.,Li}}{\Gamma_{H^+}}, \tag{3.4}$$

where $\Gamma_{sput.,Li}$ is the flux of sputtered Li particles from the target and Γ_{H^+} is the flux of H^+ particles to the target.
The sputtering Yield can be calculated as:

$$Y(T) = \frac{Y_{ad}}{1 + A\exp\left(\frac{E_{Eff}}{k_B T_{surf}}\right)} \tag{3.5}$$

where Y_{ad}, A and E_{eff} are fitting parameters from experimental data. The best-fit values are $Y_{ad} = 2.9$, $A = 9\,6\mathrm{d} - 6$, and $E_{eff} = 0.70eV$.
The sputtering yield for different target temperature, calculated according to 3.5, is shown in figure 3.4. Once the sputtering yield is know, $\Gamma_{sput.,Li}$ is calculated by inverting 3.4.
In the simulated conditions H^+ flux to the target is about $10^{24}\,\mathrm{m^{-2}s^{-1}}$ and the sputtering yield is about 1, this means that, for temperature below 900 K sputtering emission is always dominant on evaporation emission, the opposite happens for temperature higher than 900 K
Lithium particles emitted from sputtering process are emitted with the same energy as the impinging

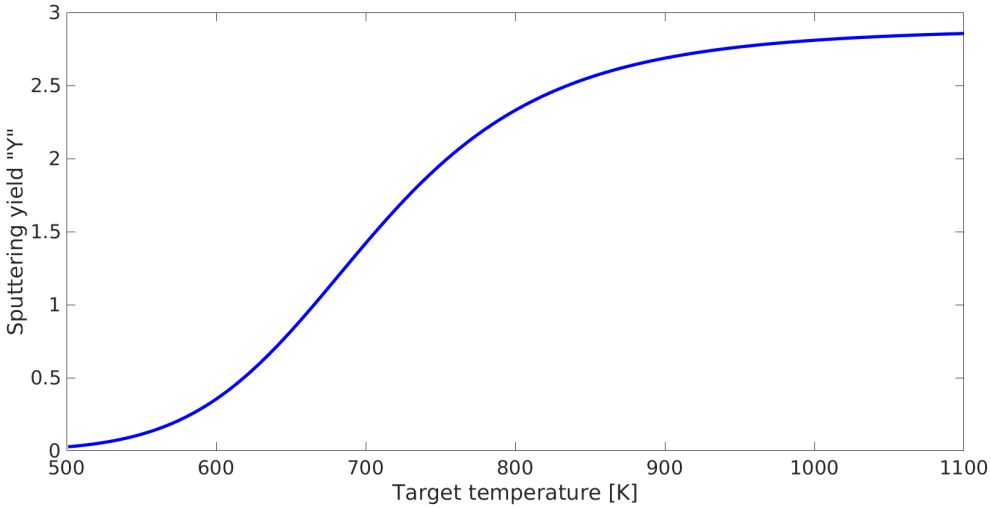

Figure 3.4: Lithium sputtering yield varying target temperature. Since plasma flux to the target in my simulations is about $10^{24}\,\mathrm{m^{-2}s^{-1}}$ so it is the lithium flux from sputtering.

particle.

The only other neutral particles source in the system is the H_2 and H source at the target region entrance (for target region geometry). These were introduced to compensate for the loss of particles to the pumps and simulate neutral flux from the vessel wall to the pumps themselves. The source is a uniform over the length of the target region entrance and its value can be settled in order to obtain the required neutral pressure in the simulated region.

Boundary condition for incident particles

I'll now analyze what happens to a test particle when it reaches a wall.
Absorption boundary condition are settled at the pumps. It means that any test particle which crosses that boundary is lost. The same condition which were applied to the entrance of the target region.
At the axis of the chamber, that computationally is treated like a wall, specular reflecting boundary conditions are settled for each species; this way, thanks to the axial geometry of the system, the influence of the axial wall is canceled.
For lithium non reflecting boundary conditions are settled for any other wall that has not been discussed yet. This condition has been chosen because, since every facing component of the chamber, but the lithium target, is at the environment temperature, that is less than lithium evaporation temperature, lithium particles immediately condensate there and are lost. If reflection conditions would have been used, time in cell for the test particles nearby the walls would had been doubled on average and so had been the density; there would have also been a Li velocity contribution exiting the walls that does not exist in reality.
Also the target has non reflecting conditions for lithium test particles for similar reasons. Lithium real particles are in fact reabsorbed by the target if they hit it, and so imposing non reflecting conditions is still the most physical choice.
For H and H_2 test particles specular reflection has been chosen for each wall (but the pumps as previously described) again to conform with real physics of the real system where a not only in-coming particles to the wall are present for also out-coming due to de-absorption.

3.2.2 Plasma boundary conditions

Plasma boundary conditions are instead the classic boundary condition to be used in a finite element method. Since the plasma equations are solved only in the internal region that represents the plasma beam, boundary conditions are specified for the 4 boundaries of the internal grid: the target, the axis

of the cylinder[1], the entrance of the chamber and the limit of the internal region at $r = 3\,\text{cm}$. It has to be remembered that potential boundary conditions must be specified as well.

At the target non collisional Debye sheath non magnetic conditions were chosen for both lithium and hydrogen so the treatment in the following analysis will be the same for both species. The possibility of using non magnetic conditions is due to the fact that it has been chosen to simulate only geometries where the target plate is perpendicular to the magnetic field.
It must be specified that B2.5 solves the plasma equations only in the main plasma where quasi-neutrality is respected. The Debye sheath and the pre-sheath are not part of the simulation but their physics is used to obtain boundary conditions for the potential, ions density, momentum and energy. The validation of those conditions is discussed in 3.2.3, here the physical conditions that are supposed imposing this boundary conditions are mentioned:

- Non collisional sheath, $T_s = T_{ps}$
- Collisional pre-sheath with potential drop in the pre-sheath $\Phi_{ps} - \Phi_p = -\frac{K_B T_e}{2q}$; where Φ_{ps} is the potential at the sheath entrance, Φ_p is the plasma potential and q is the electron charge.
- Density at the sheath edge $n_s = n_p \exp(-1)$
- Ion accelerations, perpendicular to the wall, in the pre-sheath to the ionic sonic speed $c_s = \sqrt{\frac{K_B T_e}{m_i}}$

For the axis boundary the conditions chosen are reported. Those conditions reflect the fact that through the axis, in equilibrium conditions, no flux should exist. They have already been widely used [20] [31].

- Zero energy flux through the boundary for ions of each species.
- Zero momentum flux through the boundary for ions of each species.
- Zero density flux through the boundary for ions of each species.
- $\frac{\partial \Phi}{\partial x} = 0$ where Φ is the potential and x the coordinate perpendicular to the boundary.

The boundary conditions at the entrance of the beginning of the plasma column (entrance of the Magnum-PSI target chamber or plasma source)

- Fixed plasma temperature profile, it varies in different simulations. Values suitable with Magnum-PSI specifics were chosen.
- Zero gradient condition for velocity.
- Fixed density profile, it varies in different simulations. Values suitable with Magnum-PSI specifics were chosen.
- Fixed potential profile, it varies in different simulations. Normally for magnum target chamber geometry the potential profile at the entrance of the target chamber coming from B2.5 standalone simulations of the all magnum volume has been chosen.

The boundary conditions for the *internal boundary* at $r = 3\,\text{cm}$ are:

- For electrons zero temperature is set; for ions temperature boundary conditions a decay length is chosen. The decay length chosen is 3 cm that is typical for fusion devices[27].
- Zero momentum flux through the boundary for ions of each species.
- For both ion species density boundary conditions a decay length is chosen. The chosen decays length is 3 cm that is typical for fusion devices[27].
- Zero potential is set.

[1]For numerical reasons it is not possible to solve the equations till $r = 0\,\text{cm}$ so a small number (compared to the size of the experiment) as been chosen as minor radial position. In my simulations the minor radial position is $1 \times 10^{-5}\,\text{m}$ that is two orders of magnitude lower than the radial extension of the target.

3.2.3 Checking boundary conditions

Target boundary conditions

For the lithium target non collisional Debye sheath conditions were chosen for B2.5 and neutral lithium influx from the target has been chosen for Eunomia.
In order to those to conditions to be consistent with each other the Debay sheath is needed to be non collisional and and no ionization of the incoming evaporated particles is required. To verify this the sheath dynamic has to be solved. A simple 1D model of the Debye sheath has been solved in order validate those conditions.
Assuming one dimension, stationary, non collisional sheath and solving the Poisson equation in the Debye sheath turns into[19]:

$$\frac{\partial^2\Phi(x)}{\partial x^2} = \frac{e}{\varepsilon_0}\Big(n_e(x) - n_i(x)\Big) = \frac{e}{\varepsilon_0} n_s\left[\exp\left(\frac{q\Phi(x)}{K_B T_e}\right) - \left(1 - \frac{2q\Phi(x)}{m_i c_s^2}\right)^{1/2}\right], \tag{3.6}$$

since

$$n_e(x) = n_s \exp\left(\frac{q\Phi(x)}{K_B T_e}\right); \qquad n_i = n_s\left(1 - \frac{2q\Phi(x)}{m_i c_s^2}\right)^{1/2}, \tag{3.7}$$

where q is the electron charge, $\Phi(x)$ the potential, n_s the plasma density at the entrance of the sheath, m_i the mass of the ions, c_s the ionic sonic speed ($c_s = \sqrt{\frac{K_B T_e}{m_i}}$) and T_e the electrons temperature.
Equation 3.6 can be solved for example upon assuming the potential at the entrance of the sheath Φ_s equal to zero and so its derivative, then assuming quasi neutral collisional pre-sheath the potential drop is[19]:

$$\Phi_W - \Phi_p = -\frac{K_B T_e}{2q}\left[\ln\left(\frac{m_i}{2\pi m_e}\right) + 1\right] = -\alpha\frac{K_B T_e}{q} \tag{3.8}$$

where Φ_W and Φ_p are the potential at the wall and in the plasma, m_i and m_e are the mass of the ions and the electrons and $\alpha = \frac{1}{2}[\ln\frac{m_i}{2\pi m_e} + 1]$ is a physical parameter that can be specified in B2.5 input files.
So, if the electron temperature and plasma density are given Poisson equation can be solved in the Debye sheath. This has been done in the post processing analysis, equation 3.6 and 3.7 were solved with 3.8 as boundary conditions for each cell using plasma density and temperature of the target facing cells as input parameters.
The probability of ionization or charge exchange of the lithium particles emitted from the target in the Debye sheath depends on the ion or electron impact energy; temperature of the emitted lithium does not play any role since the particles are emitted with the wall temperature of the target so their temperature is below 0.1 eV.
If a neutral particle evaporates from a wall with temperature T_w its speed is $v_p = \sqrt{K_B T_w/m}$ and the time it takes to cover the distance l is $t_l = l/v_p$. If l is short enough to consider the background particles density and energy constant along that path the collisional frequency of a Lithium neutral particle in that region is

$$f = n\sigma v, \tag{3.9}$$

where n is the background particles density, σ the collision cross section and v the relative speed.
As previously said I'm interested in the electron ionization ($e^- + Li \rightarrow e^- + Li^+ + e^-$) and charge exchange ($H^+ + Li \rightarrow H + Li^+$). So in the system previously described the two collisional frequencies, f_{ion} and f_{ex}, in a uniform density and energy region, according to 3.9,are:

$$f_{ion} = n_e\sigma_{ion}(E_e)\sqrt{\frac{E_e}{m_e}}; \qquad f_{ex} = n_H\sigma_{ex}(E_i)\sqrt{\frac{E_H}{m_H}}; \tag{3.10}$$

where E_e, E_H, n_e and n_H are the electrons and ions energy respectively.
The probability that a lithium particle does not make an ionization or charge exchange collision (P_i and P_{ex} respectively) along the path l are calculated as:

$$P_i = 1 - t_l f_{ion}; \qquad P_{ex} = 1 - t_l f_{ex} \tag{3.11}$$

In the Debye sheath ions are accelerated by the potential drop and electrons are decelerated, ion and electron impact energy are calculated as:

$$E_H(x) = T_{i,p} - \Phi(x); \qquad E_e(x) = T_e + \Phi(x). \tag{3.12}$$

After solving equations 3.6 and 3.7 the Debye sheath length L_D can be divided into a certain number n_D of cells, each of length $l_D = L_D/n_D$, where density and potential can be considered constant. The no-ionization and no-charge exchange probabilities (P_i^j and P_{ex}^j $j = 1...n_D$) can be calculated according to 3.11. Then the total probabilities are calculated as the product of the single probabilities:

$$P_{t,*} = \prod_{j=1}^{n_D} P_*^j; \qquad * = i, ex \tag{3.13}$$

The ionization and charge exchange probabilities are then calculated subtracting $P_{t,i}$ or $P_{t,ex}$ from the total probability 1.
This procedures has been implemented in the post processing analysis using the temperatures and densities of each cells in front of the target to check if there are ions coming to the system from the target.
Since electron density drops down exponentially in the Debye sheath, while the ion density decreases more slowly, according to equation 3.7. Furthermore electron energy decreases in the Debye sheath, according to 3.12 so charge exchange collisions are always more relevant than electron ionization collisions for lithium in this temperature range. The higher the plasma temperature the higher the potential drop (equation 3.8), the higher the ion energy (equation 3.12), the higher the charge exchange frequency. For those reasons the simulations with higher plasma temperature will be those where I will find the higher charge exchange probability.
In figure 3.5 the two probabilities, ionization and charge exchange in the Debye sheath, are shown against the radial position for the higher plasma temperature simulated with Magnum-PSI. It is shown that the charge exchange probability is always lower than 0.1%. In the other simulations with lower plasma temperature the charge exchange probability is order of magnitude lower. So it has been proved that the two Eunomia and B2.5 boundary conditions are consistent with each other.

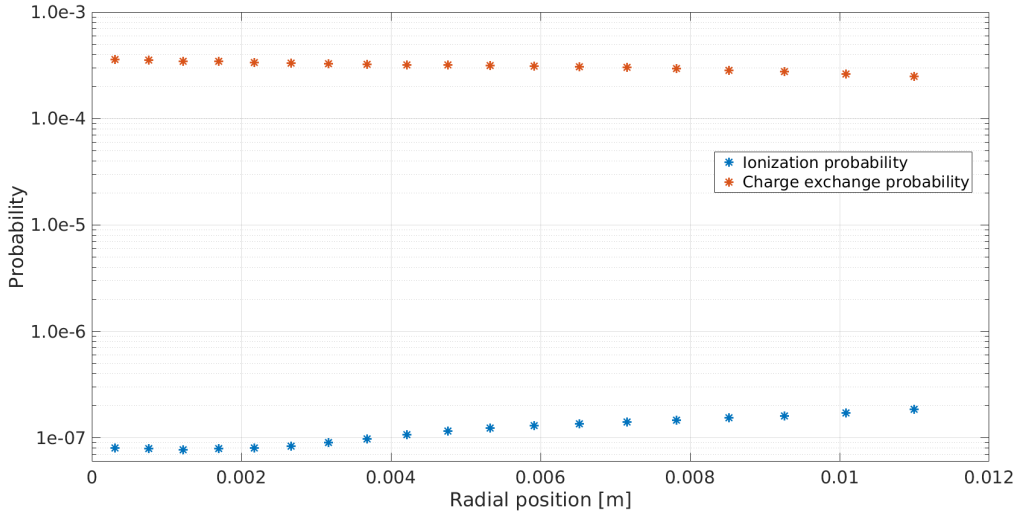

Figure 3.5: Probability that an evaporated particle makes a ionization or a charge exchange collision in the Debye sheath. Those results were calculated using as input parameter the plasma temperature and density obtained in a simulation where the target temperature was 700 K and the plasma temperature upstream T_e =7 eV.

T_{target} [K]	T_e [eV]	Γ_{in} $[part/m^2]$	Γ_{out} [part/m^2]	ratio	$\Gamma_{Li^+,loss}$ $[part/m^2]$	New Γ_{out} $[part/m^2]$	new Ratio
700	5	1.65×10^{20}	1.53×10^{20}	7.41%	8.00×10^{18}	1.61×10^{20}	2.57%
800	5	2.55×10^{20}	2.38×10^{20}	6.54%	7.60×10^{18}	2.46×10^{20}	3.56%
850	5	3.61×10^{20}	3.50×10^{20}	2.87%	4.50×10^{17}	3.61×10^{20}	-0.02%
600	5	1.75×10^{19}	1.56×10^{19}	10.71%	2.20×10^{18}	1.78×10^{19}	-1.85%
700	5	1.57×10^{20}	1.54×10^{20}	1.96%	2.20×10^{18}	1.57×10^{20}	0.56%
700	7	8.76×10^{15}	8.74×10^{15}	0.20%	3.00×10^{13}	8.77×10^{15}	-0.14%
700	6	1.93×10^{20}	1.76×10^{20}	9.09%	1.20×10^{19}	1.88×10^{20}	2.89%

Table 3.1: Lithium fluxes in different simulations.

Lithium density conservation

To check if the selected boundary conditions respect the mass conservation law lithium flux in and out of the system has been calculated for the outcomes of the simulations that had been performed. The goal has been checking if there is a consistent difference between lithium flux in and out of the system. This checking has been performed for each run that had converged according to the parameters that will be presented in chapter 4.2.
The outgoing normal direction of each wall of the eight walls has been calculated: $\hat{n_j}$ j=1...8.
Each cells in which at least one of border represent a fraction of an external wall, according to figure 3.1a, from now on will be called wall-cells. For each wall cells the area of the external wall represented by its external border has been calculated. If N_W is the number of external walls and N_j the number of wall cells of the j-th wall, I will name each area A_i^j with $j = 1...N_W$ and $i = 1...N_j$. Consequently it has been checked that the total external area corresponds to the sum of the wall cells external area:

$$A_{tot} = \sum_{j=1}^{N_W} \sum_{i=1}^{N_j} A_i^j. \tag{3.14}$$

The physical information for each specie in each cell of Eunomia output are: density, temperature, average velocity in all three directions and their relative sources that are passed to B2.5. For these reasons Li and Li^+ fluxes, from each wall cells, off the system were calculated as:

$$\Gamma_{*,i}^j = A_i^j n_{*,i}^j \mathbf{v}_{*,i}^j \cdot \hat{n}_j; \qquad * = \mathrm{Li}, \mathrm{Li}^+ \tag{3.15}$$

where in 3.15 the same notation as in equation 3.14 has been used, and $\mathbf{v}_{*,i}^j$ stands for the average velocity vector for Li or Li^+ in the i-th cell of the j-th wall. According to 3.15 the lithium flux out of the system will be positive and lithium flux into the system (only in front of the target) is considered negative. The total Li and Li^+ fluxes will be summed since we are not interested in the charge state of the incoming/outgoing particles but only on lithium flux.
This check of the lithium flux was performed for the output of each simulations that had converged; all of them presented analogous results. In table 3.1 the results from some of the simulations shown. The incoming lithium flux $\mathrm{Li_{in}}$ and the outgoing lithium flux $\mathrm{Li_{out}}$ calculated from the output of different simulation are reported; the ratio that corresponds to the fifth column is calculated as $\frac{\mathrm{Li_{in}}-\mathrm{Li_{in}}}{\mathrm{Li_{out}}}$ and represents the difference between incoming and outgoing lithium from the system normalized to the total incoming lithium in the system. It shows that the incoming lithium flux is alway bigger than the outgoing.

The reason of this systematic difference is due to the fact that Li^+ dynamics is calculated only in the internal region. As it will be shown in chapter 5, where the outcome of the simulations will be shown, Li^+ density suddenly drops to 0 out of the internal region, this indicates that some Li^+ is lost in the simulations due to the geometry of the discretization.
Calculating the Li^+ flux that is lost out of the internal region $\Gamma_{Li^+,loss}$ as been calculated as the other fluxes. Thus, adding this contribution to the outgoing flux, a new ratio as been calculated as the

previous one (last two columns of table 3.1). It is shown that the ratio of the flux difference reduces by almost a order of magnitude and that the incoming flux is not systematically higher than the outgoing since some ratio are below 0. The remaining difference, that is around 1% of the incoming lithium flux can be due to Montecarlo fluctuation and finite discretization but does not present the systematic behavior previously described.
Those considerations lead me to the conclusions that the boundary conditions themselves are well coupled but some of the lithium particles are unavoidably lost due to the geometry of the simulation itself.

Chapter 4

Computational methods

4.1 Convergence process

The process to make the simulation converge is a multi-step process. In low lithium density runs the process is divided into three steps, in high lithium density simulation the number of steps is higher. The three main steps in each simulations are:

- B2.5 standalone convergence;
- *frozen plasma* coupled simulation;
- *warm plasma* coupled simulation.

The initial solutions for plasma and neutrals are flat, gaussian or triangular distributions. B2.5 standalone is run until the main plasma quantities reaches convergence. The initial B2.5 standalone run is only needed to have a initial plasma solution as initial condition for the coupled run, for this reason there is no strict convergence criterion: B2.5 is run until the oscillation of plasma temperature and density is orders of magnitude lower than their related quantities. In figure 4.1 the electron temperature in a cell is shown against the *simulation time*. Simulation time it is not the real time evolution of plasma but the sum of all time discretization units dt used to discretize time derivative terms in B2.5 equations(see section 1.3). dt is fixed at the beginning of the run, and it is the value of time discretization, the higher the precision, but the longer the simulation will be. In figure 4.1 the time assigned to iteration n is $t_n = n \cdot dt$. Normally in this pre-run $dt = 10^{-6}\,\mathrm{s}$, if higher dt is set, the residuals of some plasma quantities become too big and the simulation stops after finding some *Not A Number*.
In those B2.5 standalone pre-run Li^+ density is kept to 0[1] to not influence other plasma quantities. When B2.5 standalone run at the beginning of the simulation was skipped the coupled run has diverged at the first iteration.

After the first standalone B2.5 run the plasma temperature close to the target is very high compared to the equilibrium temperature reached when lithium is added. With the parameters I used in the simulations, plasma temperature in the lithium cloud in front of the target is about 0.4 eV, while after the standalone run it is about 3/4 eV, one order of magnitude more.
For this reason it is not possible to start the simulation with a time discretization dt as high as the one used in the standalone simulation. dt must be kept low in order to reduce residuals terms. If time discretization is kept high, about $10^{-6}\,\mathrm{s}$, the code diverges after few iterations as it is shown in figure 4.2 that shows the target temperature evolution in a cell in a diverging run. To have a clear overview of the diverging mechanism to avoid a "movie" of the same diverging run is shown in figure 4.3, 4.4 and 4.5 that show lithium density, electron temperature and electron energy source evolution respectively.
Simulation-time evolution of plasma temperature is so rapid that allows lithium to diffuse everywhere,

[1] Initial density can not be set to zero for numerical reasons, a initial density of $1\,\mathrm{m}^{-3}$ was set.

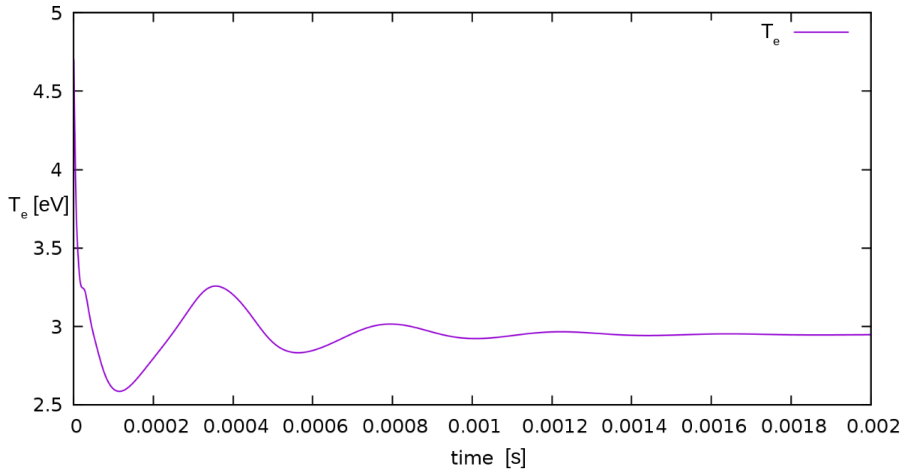

Figure 4.1: Electron temperature convergence in a test cell during the standalone B2.5 run.

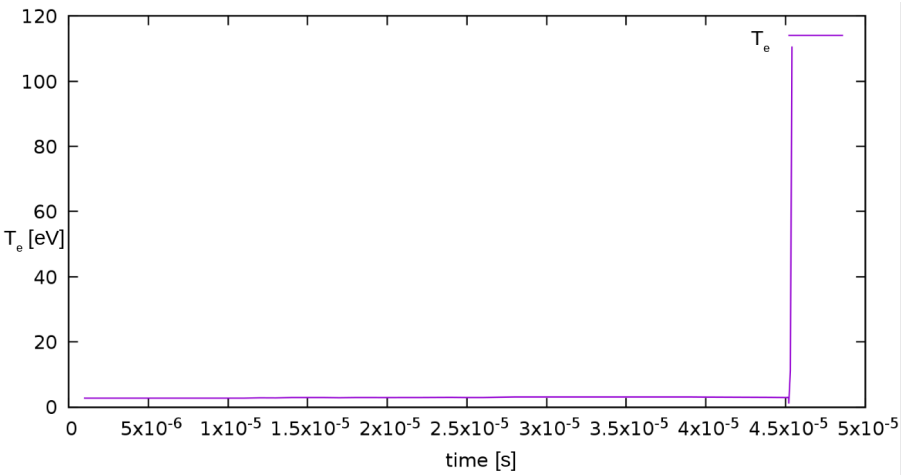

Figure 4.2: Electron temperature divergence in cell in a B2.5-Eunomia coupled run.

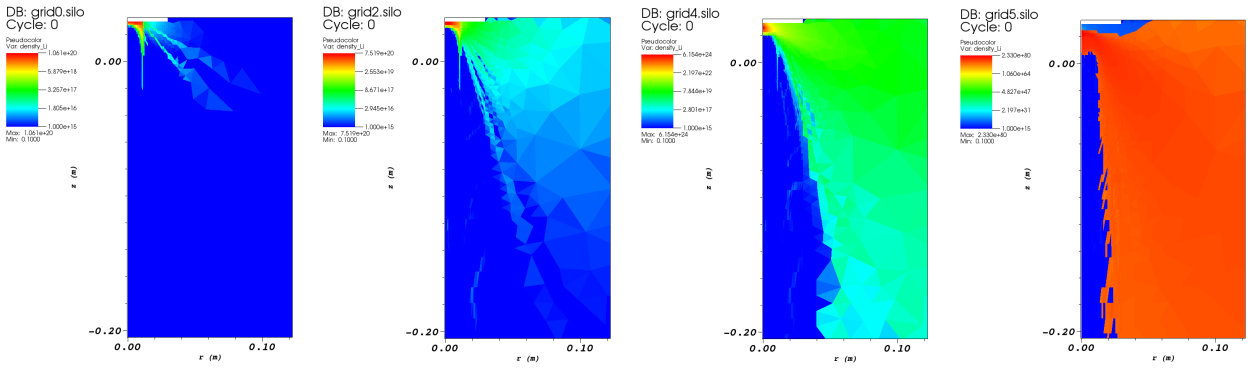

(a) Cycle 0. (b) Cycle 2. (c) Cycle 4. (d) Cycle 5.

Figure 4.3: Lithium density evolution in a diverging run.

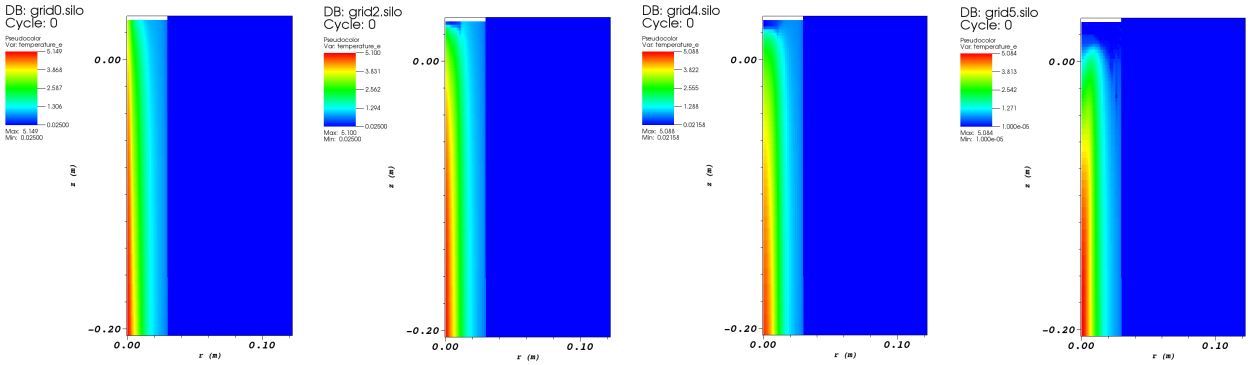

(a) Cycle 0. (b) Cycle 2. (c) Cycle 4. (d) Cycle 5.

Figure 4.4: Electron temperature evolution in a diverging run

plasma cooling peak moves down as well as the lithium density front[2], these two effect combined produce a high electron plasma energy loss (figure 4.5c and 4.5d) that decreases plasma temperature, lithium recombination increases and so lithium density does. These chain effect rapidly diverges after a few iteration as shown in figure 4.3d, 4.4d and 4.5d.

For those reasons it is needed to firstly run a coupled run with almost *frozen plasma*, that means selecting a very small dt, for those reason plasma quantities will not change during this second run that is equivalent to a Eunomia standalone run. The high plasma temperature close to the target confines neutral lithium close to the target since lithium particles, if moving upstream, are immediately ionized; some lithium particles are able to escape the beam are and diffuse in the chamber composing a lithium density background. This dual actions of plasma temperature on lithium density profile and the other way around are very strongly coupled with each other as it will be shown in the next chapter, for this reason plasma temperature and lithium density can not freely oscillate.

After the frozen plasma simulation has run for about 100 cycles and a lithium background density is set, it is possible to start the proper coupled run that is called "*warm plasma*" run. The simulation is run until it converges according to the parameters described in section 4.2. The number of iteration required depends on the total lithium influx from the target and the number of test particles generated for each neutral source. The higher the lithium flux, the higher the required number of iteration; the higher the number of test particles, the lower the number of cycles required.
In runs where the lithium flux from the target is very high, $T_{tar} > 700\,\mathrm{K}$ or $T_{e,max} < 5\,\mathrm{eV}$, some intermediate steps between the *frozen plasma* run, $dt \sim 10^{-10}\,\mathrm{s}$, and the *warm plasma* run, $dt \sim 10^{-6}\,\mathrm{s}$, some intermediate step are required in order to avoid the same kind of divergence that has been described before.

[2]The reason why electron energy loss and lithium density front always move together will be explained and demonstrated in the next chapter and it is related to the fact that ionization is the main plasma energy loss channel

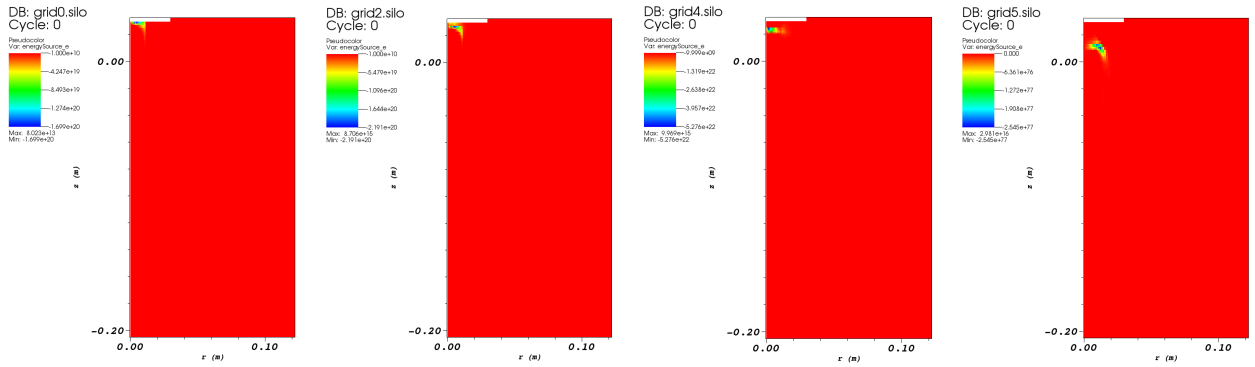

(a) Cycle 0. (b) Cycle 2. (c) Cycle 4. (d) Cycle 5.

Figure 4.5: Electron energy source evolution in a diverging run.

4.1.1 Trapped particles

When running simulations with high lithium density flux a lithium cloud is formed in front of the target. Lithium density and plasma temperature are linked to each other[3], so, if lithium density profile moves back, lithium density profile moves forward and vice versa. As it has been shown in figure 4.1, plasma quantities oscillate when slowly converging. The coupling of lithium density with plasma quantities, together with plasma temperature oscillating behavior makes lithium high density front oscillate forward and backward together with the plasma temperature. In figure 4.6a the lithium cloud had moved forward in the plasma beam, while in figure 4.6b the lithium cloud had been pushed back by the increasing local plasma temperature.
As it is shown in figure 4.6b, when the lithium cloud moves back, some high neutral lithium density areas are left in the plasma. This behavior is related to the fact that the plasma quantities, like electron temperature is evolving in the simulations faster than the neutral quantities like lithium density. For this reason, when electron temperature increases the lithium cloud is not pushed back enough, therefore some neutrals particles are trapped in a high electron temperature regions, where, according to the CR model, the neutral density should be lower. The fact that those particles are *trapped* is due to the fact that, in a high neutral density volume more test particles are generates, those particles hardly leave the cell and are immediately ionized due to the high plasma temperature, "the time in cell" for lithium is higher than expected due to the high number of test particles generates. Furthermore, when calculating the new neutral background, Eunomia weight the old background with the results of its last iteration, this also makes those trapped particles hardly disappear. Thus big oscillations must be avoided in order to prevent the presence of unphysical trapped particles.
The way that I found to avoid big plasma temperature oscillation is: reducing dt and reducing the speed of plasma evolution that can be quantified as $N_{B2.5} \cdot dt$, where $N_{B2.5}$ is the number of B2.5 iteration between each Eunomia iteration. The reason why plasma quantities evolution had been slowed down is to avoid trapped particles, while the reason why dt has been reduced is to reduce the residuals and so decrease the oscillations amplitude.
In the specific case of the run with the geometry called *Magnum target geometry*, dt had been reduced from 10^{-6} s to 10^{-8} s and $N_{B2.5}$ has been increased from 10 to 100. This way oscillations with a period of about 30 cycles had been stopped in 100 cycles and their stability has been checked over about 200 cycles.

4.2 Convergence criteria

Convergence of each run has been checked with a script designed for checking convergence of Monte Carlo codes. The implementation of the script that checks the convergence of the runs was not part of this project since it had already been written[4]. I have only adapted some input parameters and

[3] it will be proven on the next chapter
[4] Courtesy of Ray Chandra, PHD at DIFFER.

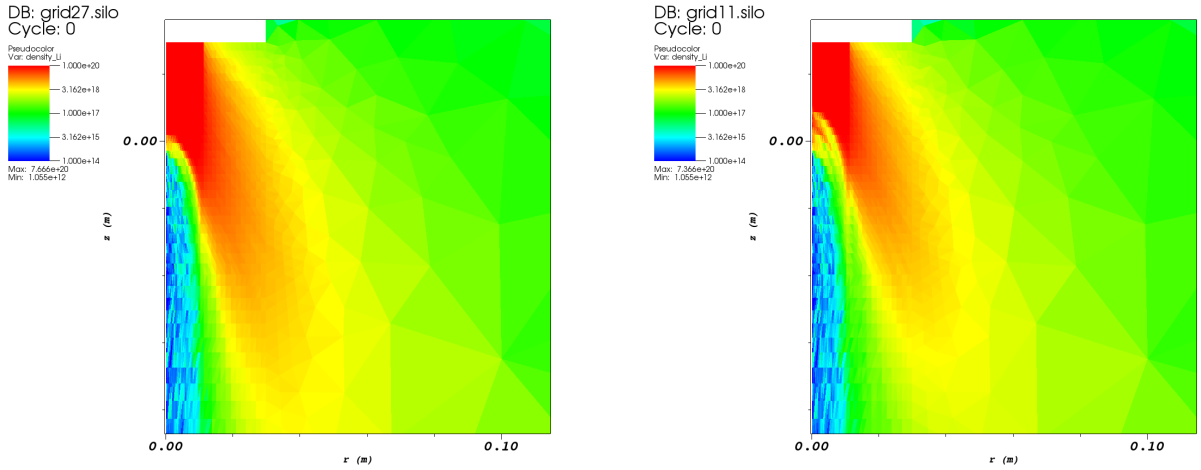

(a) Oscillation that causes trapped particles.

(b) Trapped particles after oscillation.

Figure 4.6: Trapped lithium particles in high energy plasma caused by plasma temperature oscillations.

checked the convergence of the runs by using the script, so just a quick overlook at the implemented method will be given; the reader can find detailed information in the article written by M.Y.Ata[4] whose theory has was implemented in the script.
The proposed criterion seeks a convergence band around the average value. The width of the band is 2σ. The variance is calculated from the distribution in every cycle of each quantity in every cell. Once the confidence belt was made, for each quantity the script checked in which cells the values assumed by that quantity in the last 50 cycles had been always inside the confidence belt; if so, that quantity in that cell was considered converged. When 90% of the cells had converged for that quantity the run itself had been considered to converged for that quantity.

It was also checked that, if trapped particles were avoided, identical simulations starting from equal starting conditions, but using different time discretization dt, were converging to the same equilibrium state. This was done by using the same confidence belt criterion.

Chapter 5

Results of the simulations

In this chapter the outcome of the simulation with Magnum target chamber geometry will be presented; for this reason the geometry implemented in these simulation is the so called (in chapter 3) *Magnum-PSI target chamber*, the boundary conditions and the target simulated are those which have been described for the same geometry in the same chapter.
Simulations with Magnum geometry have been performed by using different maximum plasma temperature, plasma temperature profile and target temperature.
As anticipated in chapter 3, plasma temperature T_e is a plasma boundary condition upstream as well as plasma density. Both plasma density and temperature were assumed to exhibit a Gaussian profile whose values of maximum density, maximum temperature, density and energy semi-amplitude ($T_{e,max}$, $n_{e,max}$, σ_{T_e}, σ_{n_e} respectively) similar to that of previous experiments performed with Magnum-PSI[10]. This way, plasma-target interaction, lithium cooling and transport was studied in different regimes.
In order to check target temperature (T_{Tar}) influence, a scan on T_{Tar} has been made by performing five runs while varying T_{Tar} from 550 K up to 850 K and $T_{e,max} = 5$ eV; then a scan on plasma temperature has been performed while varying plasma temperature at the entrance of the target chamber from 4 to 7eV (no more than 7eV according to the limit of the model established in chapter 2) and while fixing the target temperature at 700 K.
It must be underlined that in the first scan a low value for σ_{T_e} has been used, a higher one has been used for the second scan in order to understand the influence of this parameter on lithium transport.
The input parameters of the nine runs that have just been described is summarized in table 5.1. The first block of runs from run030 to run034 will be named *target temperature scan*, the second block of runs will be named *plasma temperature scan*.
H^+ plasma temperature profiles upstream, described in table 5.1 are shown in figure 5.1. In order to make the figures more understandable for the reader, in the legend of the pictures, from now on, I will refer to each run by writing its plasma temperature peak upstream and its target temperature peak.

run number	$T_{e,max}$ [eV]	σ_{T_e} [eV]	$n_{e,max}$ [m^{-3}]	σ_{n_e} [m^{-3}]	T_{Tar} [K]
030	5	0.01	10^{-20}	0.01	550 K
031	5	0.01	10^{-20}	0.01	700 K
032	5	0.01	10^{-20}	0.01	800 K
033	5	0.01	10^{-20}	0.01	850 K
034	5	0.01	10^{-20}	0.01	600 K
036	5	0.018	10^{-20}	0.01	700 K
037	7	0.018	10^{-20}	0.01	700 K
038	6	0.018	10^{-20}	0.01	700 K
039	4	0.018	10^{-20}	0.01	700 K

Table 5.1: Plasma density profiles upstream and target temperature in Magnum-PSI target chamber geometry simulations.

The scale of greens refers to the target temperature scan and the scale of reds refers to the plasma temperature scan.

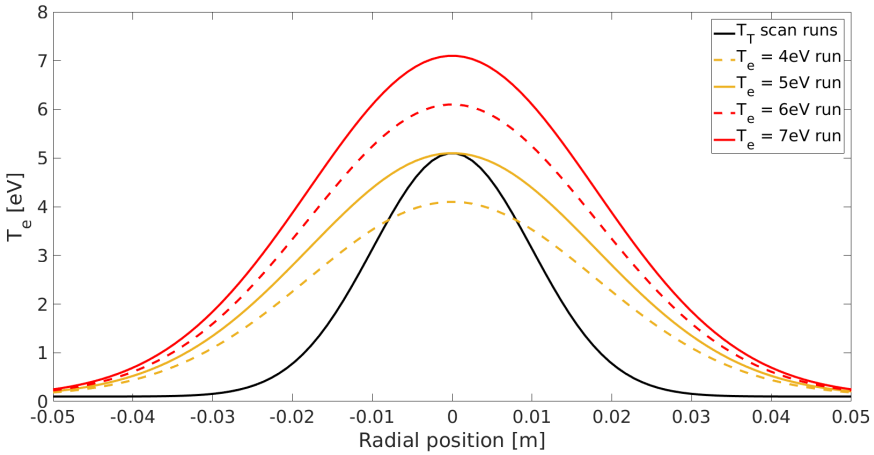

Figure 5.1: Plasma temperature profile upstream in different simulations, for all the runs of the target temperature scan the plasma profile is the same. Different width were used for the plasma temperature scan runs in order to study the influence of this quantity on lithium transport. In further results analysis plasma temperature width will be compared to the target diameter, $d = 2.4\,\mathrm{cm}$.

I must emphasize that the convergence of all the nine runs, that has just been described, and whose results will be described in this chapter, have been checked according to the parameters described in chapter 4.

5.1 Simulations output outlook

Part of the output of the simulations is shown in figures from 5.2 to 5.10; in those figures Li density, Li^+ density and electron temperature are shown.
Watching the following figures the reader must pay attention to the actual scale of each figure; in fact, in order to make every single figure physically readable, it has been chosen to use different scale from figure to figure that show the same quantity from different runs.
In the following images, for all the quantities related with neutral particles, a 2D projection of the 3D simulation output is shown, the same that is passed from Eunomia to B2.5 as background for plasma simulations. All the quantities related to plasma dynamic are presented in the same 2D geometry they are simulated with.
The symmetry axis of the cylinder (magnum target chamber) is on the left hand side of each figure, the white strip is the target holder and the target is positioned at the end of the target holder (lower part of the strip). When plasma related quantities are shown, only the beam area, simulated by B2.5 is shown.

5.1.1 Lithium transport in the chamber

One of the first phenomena that can be qualitatively seen in figures from 5.2a to 5.10a, when considering lithium transport from the target, is that two different lithium transport channels are present: direct lithium jet from the target and ionization-recombination: a lithium particle emitted from the target can either directly diffuse into the chamber or be ionized and then diffuse as an ion to the outer part of the beam, where the plasma temperature is lower, ad then recombine and diffuse as a neutral.
Runs where lithium direct jet from the target is dominant are run032 and run033, they are shown in figure 5.4a and 5.5a. On the other hand the ionization-recombination transport is dominant in run037 and run038, as it is shown in figure 5.8a and 5.9a; the proof that in those cases . In some other cases the two transport are equivalent, as in run036 as shown in figure 5.7a.

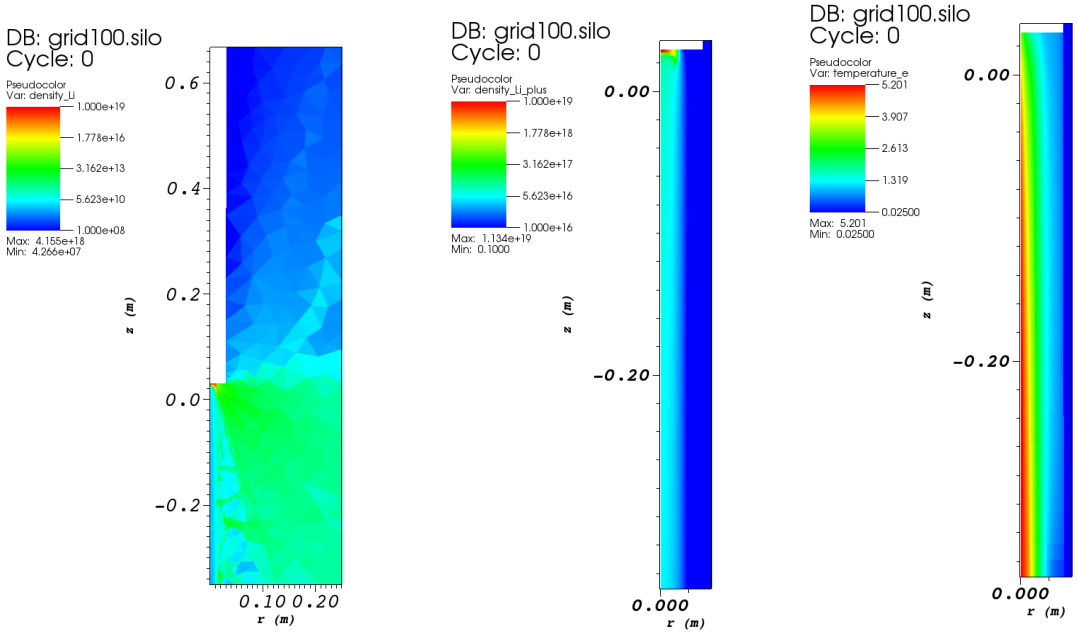

(a) Run030 Li density shape (b) Run030 Li^+ density shape (c) Run030 electron temperature shape

Figure 5.2: Run030 Li, Li^+ and electron temperature shape.

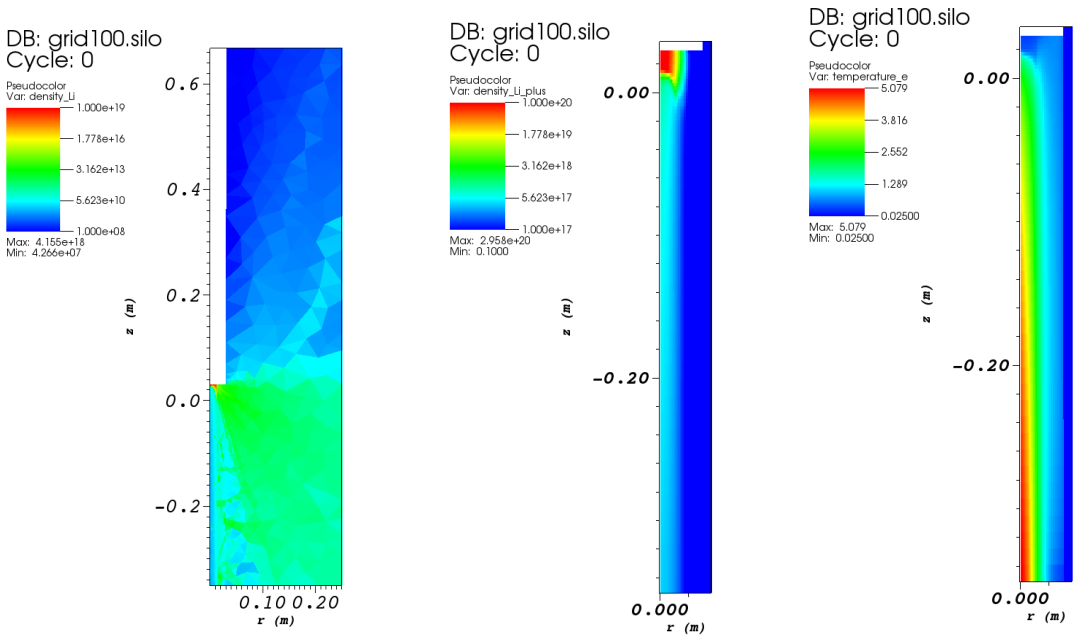

(a) Run031 Li density shape (b) Run031 Li^+ density shape (c) Run031 electron temperature shape

Figure 5.3: Run 031 Li, Li^+ and electron temperature shape.

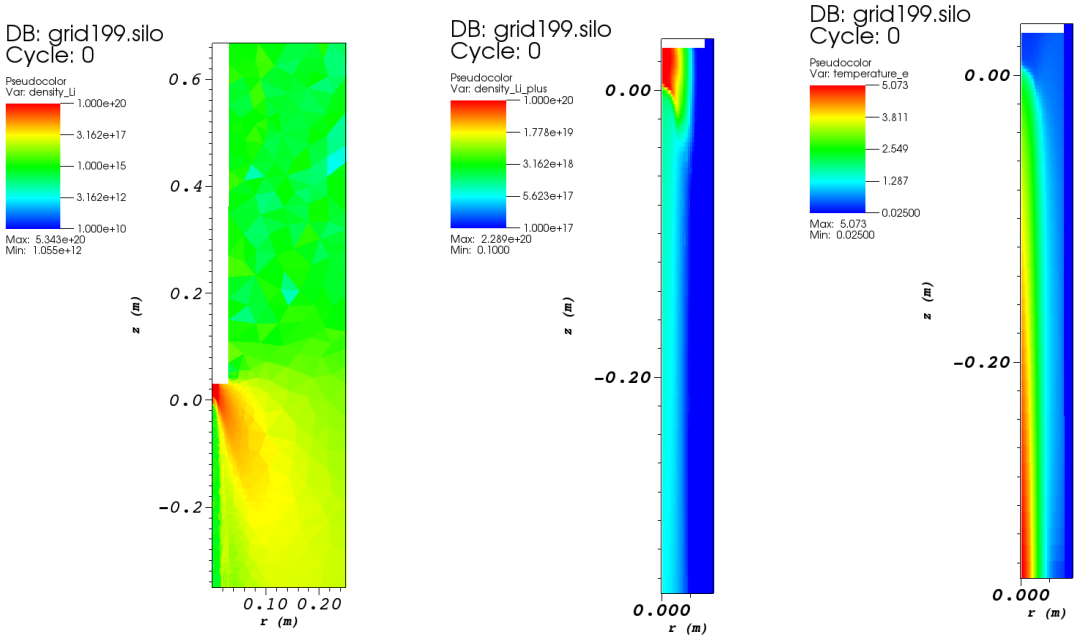

(a) Run032 Li density shape (b) Run032 Li^+ density shape (c) Run032 electron temperature shape

Figure 5.4: Run032 Li, Li^+ and electron temperature shape.

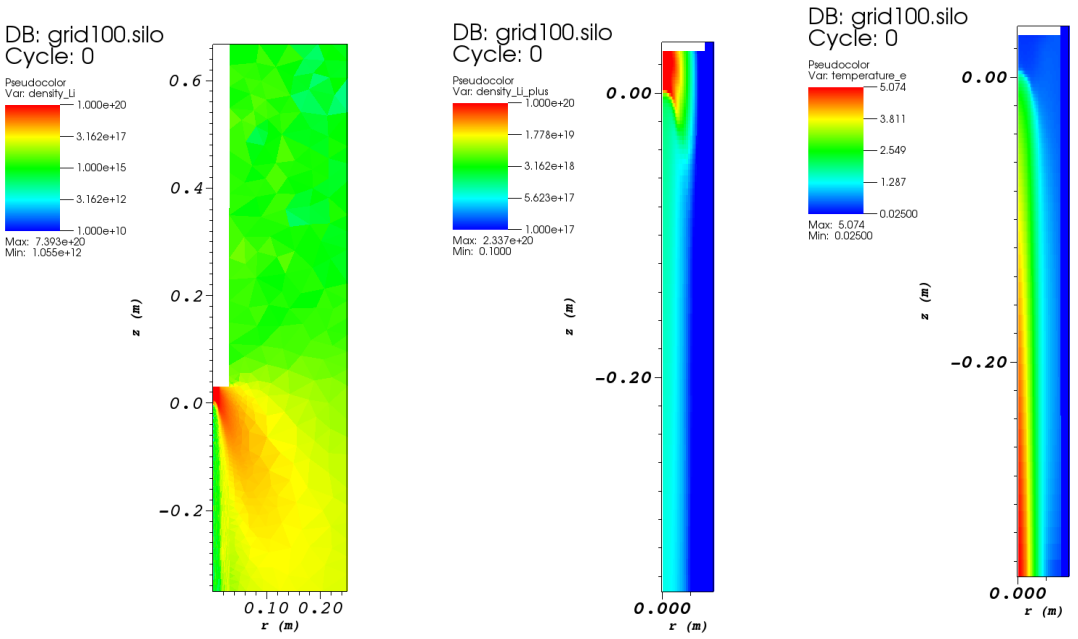

(a) Run033 Li density shape (b) Run033 Li^+ density shape (c) Run033 electron temperature shape

Figure 5.5: Run 033 Li, Li^+ and electron temperature shape.

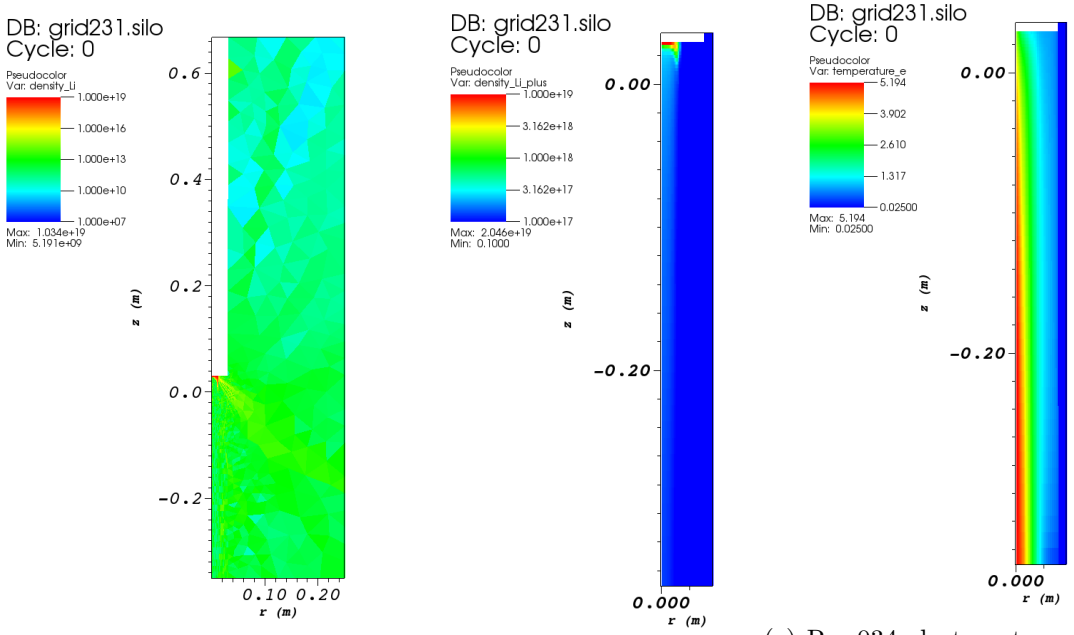

(a) Run034 Li density shape (b) Run034 Li^+ density shape (c) Run034 electron temperature shape

Figure 5.6: Run 034 Li, Li^+ and electron temperature shape.

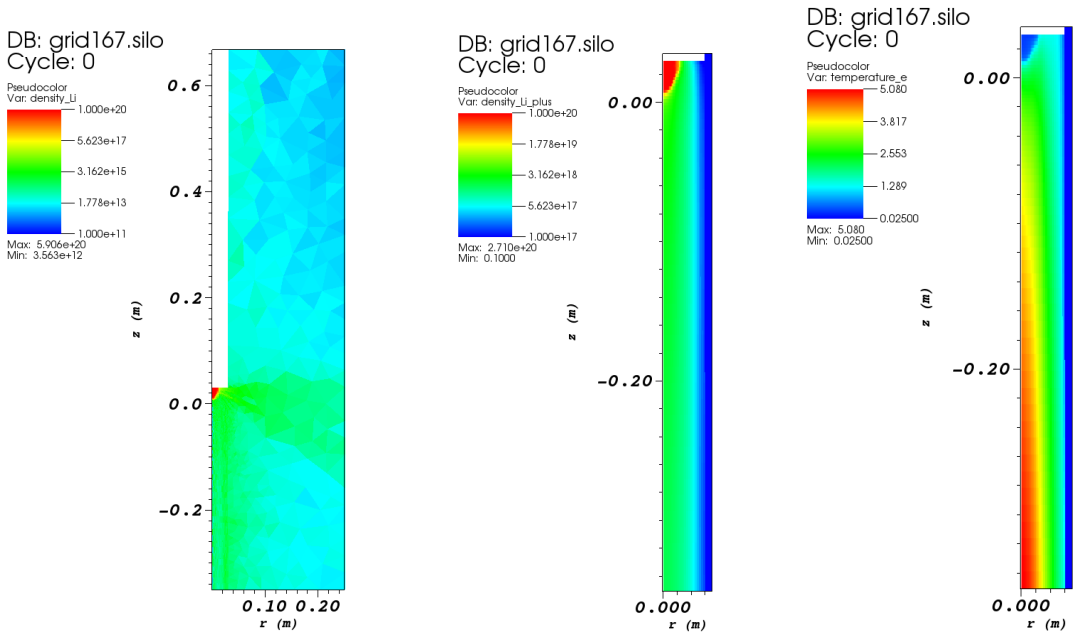

(a) Run036 Li density shape (b) Run036 Li^+ density shape (c) Run036 electron temperature shape

Figure 5.7: Run036 Li, Li^+ and electron temperature shape.

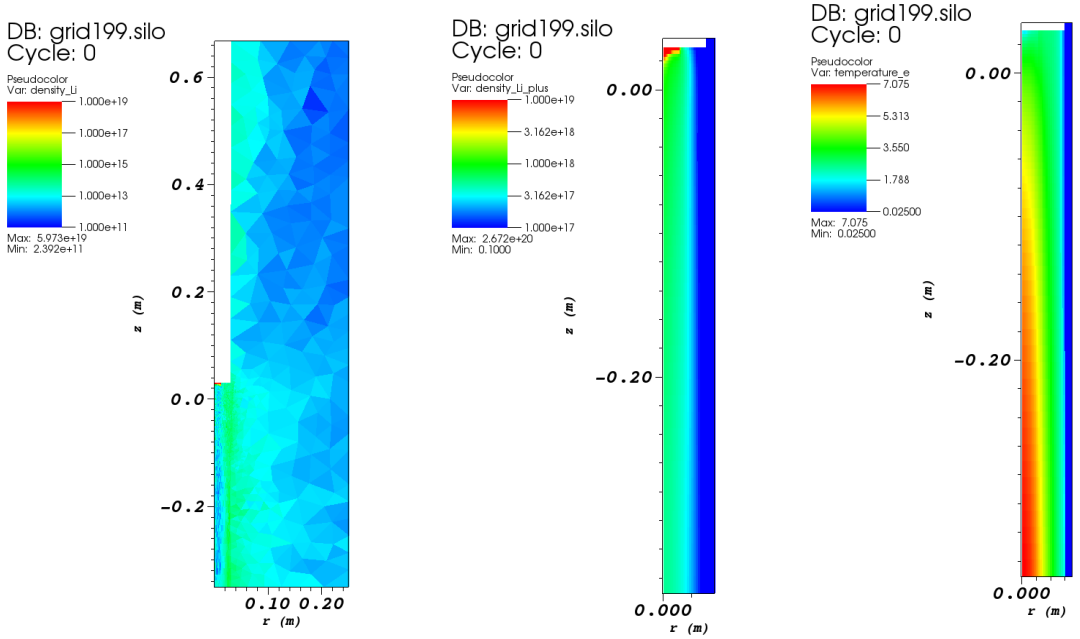

(a) Run037 Li density shape (b) Run037 Li^+ density shape (c) Run037 electron temperature shape

Figure 5.8: Run037 Li, Li^+ and electron temperature shape.

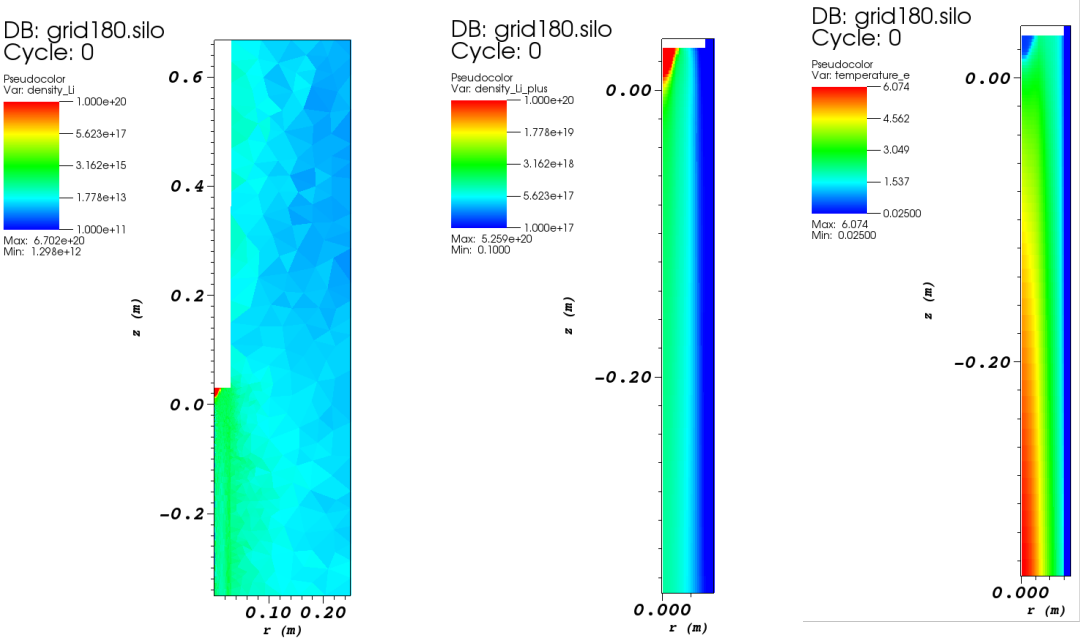

(a) Run038 Li density shape (b) Run038 Li^+ density shape (c) Run038 electron temperature shape

Figure 5.9: Run 038 Li, Li^+ and electron temperature shape.

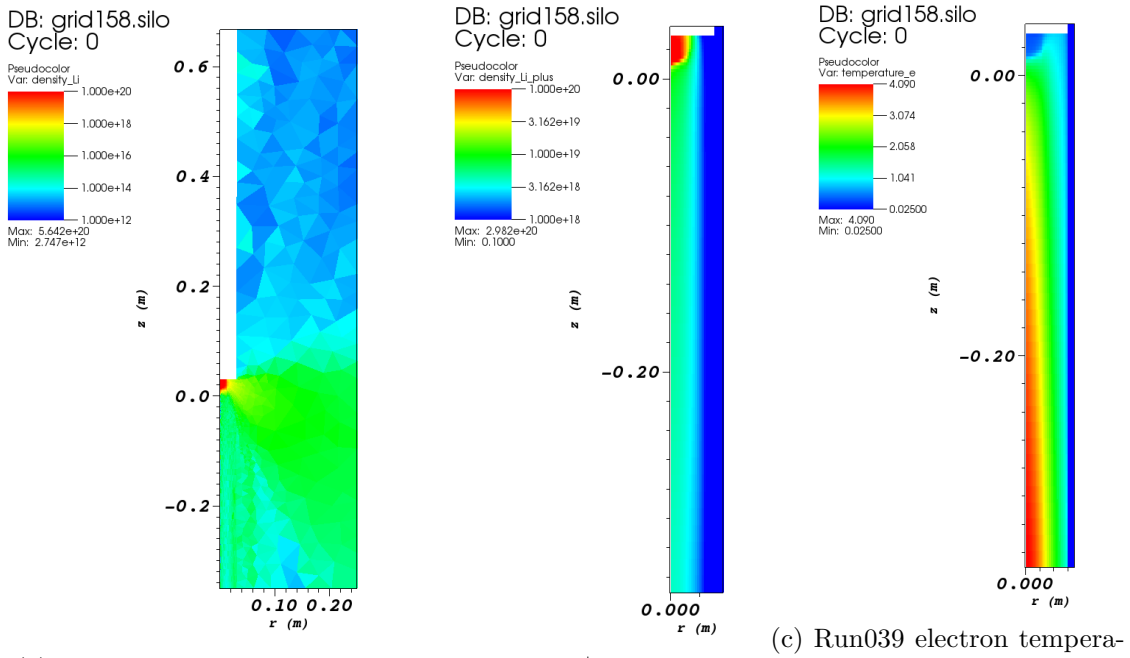

(a) Run039 Li density shape (b) Run039 Li^+ density shape (c) Run039 electron temperature shape

Figure 5.10: Run039 Li, Li^+ and electron temperature shape.

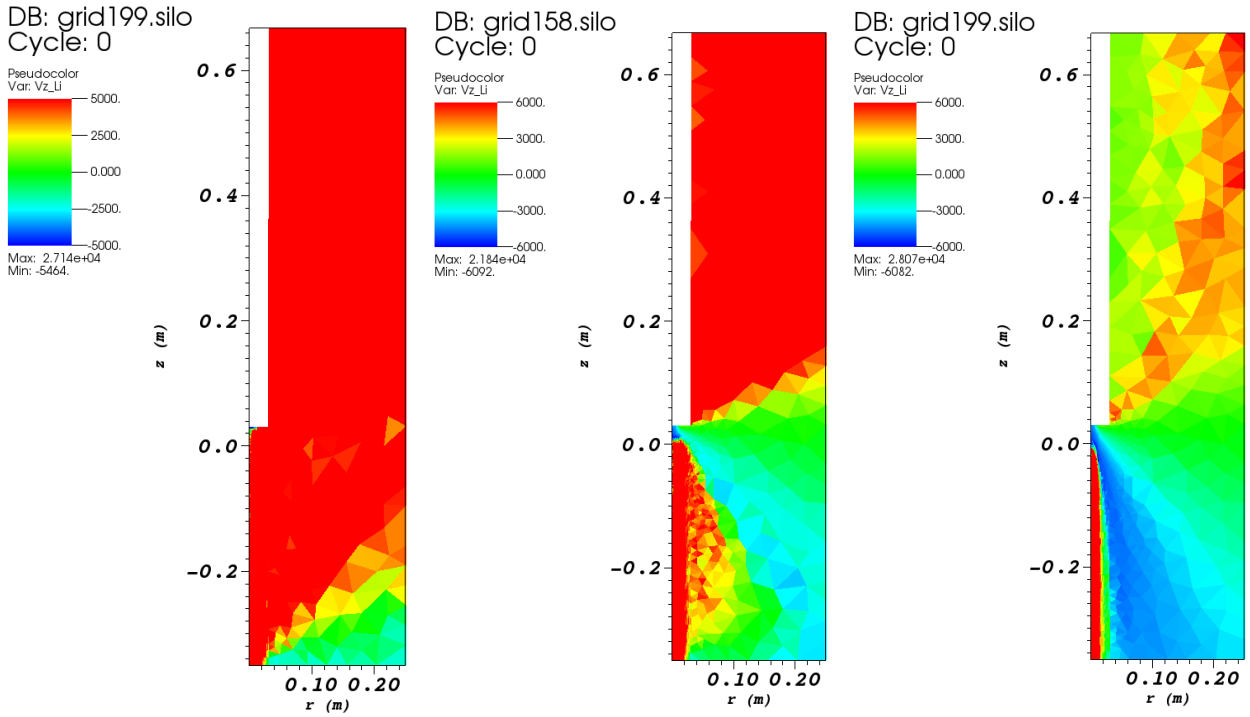

(a) $v_{z,Li}$ in run037, only ionization-recombination transport is present: the average axial velocity of lithium particles is positive since they are generated from recombination of Li^+ particles that have positive axial velocity.

(b) $v_{z,Li}$ in run037, intermediate regime: lithium velocity is positive close to the beam and negative in the lithium jet.

(c) $v_{z,Li}$ in run032, lithium jet regime: lithium velocity is negative in most of the chamber.

Figure 5.11: $v_{z,Li}$ comparison in different regimes.

The difference between the two regimes is also evident by looking at the axial velocity profile that is shown in figure 5.11. In run037 (figure 5.11a), where ionization-recombination transport is dominant, the average Li axial velocity, $v_{z,Li}$, is positive because Li particles are generated from Li^+ recombination, and Li^+ particles, because of to momentum exchange with plasma particles, have a positive axial velocity. Run032 is shown in figure 5.11c, it shows a Li jet regime, the axial velocity is negative since particle come straight from the target and are slightly slowed down by the low density medium. Run039 presents an intermediate regime, figure 5.11b, there is a positive contribution to the axial velocity close to the beam and a negative in the lithium jet.

While lithium jet from the target is just a neutral particle diffusive process, the ionization-recombination transport consists in a multi-step process: ionization of Li neutral particles by electrons, thermalization and transport Li^+ ions and consequently recombination of Li^+ ions where plasma temperature is low, diffusion of neutral lithium particles through the chamber. Obviously, when following a physical particle, more than one ionization-recombination process can occur, and the one explained is just the easier case.
By the computational point of view, even if the simulation of a neutral particle is stopped when the particle is ionized (the neutral particle is lost as explained in section 1.2), the ionization-recombination process is considered. In fact, if in a region more neutral Li test particles are ionized, a bigger local plasma source term is generated, this provides a higher Li^+ plasma density, in the following cycle a higher plasma density provides a higher neutral Li source from recombination, so, when the simulation converges, after hundreds of cycles, all those diffusive channels are considered.

While ionization-recombination transport is always present (some Li particles are always ionized) direct jet from the target is not always present since ionization mean free path can be much smaller than the actual plasma thickness to be crossed in order to diffuse out of the beam region into the outer part of the chamber.

A back of the envelope calculation of emitted lithium particles ionization mean free path could be done by considering only ionization: ionization mean free path could be calculated as:

$$\lambda_{ion} = \frac{v_{Li}}{\nu_{ion}} = \frac{v_{Li}}{n_e R_{ion}} \tag{5.1}$$

where ν_{ion} is the ionization frequency and R_{ion} the ionization rate coefficient from the 2s state of Li. Nevertheless lithium speed can not be approximated as the emission speed from the target since elastic collisions rate coefficient, below 1 eV, is orders of magnitude higher than the ionization rate coefficient. This is one of the reasons why the coupled codes are needed to solve such a complicated dynamics.

Ionization-recombination lithium transport perpendicular to the field lines is slower than the general neutral particle transport due to magnetic confinement on ion particles. In fact, if lithium particles are immediately ionized before escaping the plasma beam, and particles are in a high plasma temperature region, where Li^+ abundance is higher than Li abundance (see figure 2.4), the total Li and Li^+ perpendicular transport is led by the perpendicular diffusive coefficient $D_\perp(Li)$ instead of the neutral diffusive coefficient $D(Li)$. The two coefficients are linked by:

$$D_\perp(Li) = D(Li)\frac{1}{1+\omega_c^2/\nu_c^2}, \tag{5.2}$$

where ω_c is the cyclotron frequency and ν_c is the total collision frequency.
This is one of the reason why, in the simulations, when transport is dominated by ionization-recombination the plasma density out of the target is orders of magnitude lower than in those where lithium jet out of the target occurs. This is evident comparing run 5.4a and 5.5a to run 5.8a and 5.9a. A second reason is related to redeposition and it is discussed in section 5.1.2.
For those reasons, for fusion application, where lithium transport has to be reduced as much as possible due to the impurity density limit in the main plasma[22], ionization-recombination transport helps reducing lithium flux to the private region of the divertor. The consequences of this phenomena on possible future fusion scenario will be discussed in chapter 7.

5.1.2 Lithium redeposition

Some experiments have already be performed using plasma beam on different lithium targets from the one considered in this simulations. In those experiments controversy has emerged about the redeposition factor of lithium particles emitted by a liquid lithium target. The redeposition factor is the probability of a lithium particle, emitted by the target, to be reabsorbed by the target itself, instead of diffusing in the chamber. It was experimentally calculated to be either very high, about 95%, or low about 80%. The redeposition factor for lithium is calculated as the fraction of particles returning to the target with respect to the total number of particles emitted:

$$R_{Li} = \frac{\int_{A_T} \Gamma^a(Li) dA_T}{\int_{A_T} \Gamma^e(Li) dA_T}, \tag{5.3}$$

where A_T is the target area and $\Gamma^{e/a}(Li)$ are lithium flux emitted by target and lithium flux absorbed by the target respectively.

Lithium flux from the target is made of the two components: sputtering and evaporation. Lithium flux to the target is related to momentum transfer from the plasma particles to the emitted lithium particles.
As anticipated in chapter 3, target temperature profile is fixed in each simulation so the evaporation flux $\Gamma^e_{evap}(Li)$ is easily calculated by equation 3.1 for each cell one of whose sides corresponds to the target.
$\Gamma^e_{sput}(Li)$ is calculated for the same cells with equation 3.4 where H^+ flux to the target is calculated as:

$$\Gamma_{H^+} = n_{H^+} v_{z,H^+} \tag{5.4}$$

where v_{z,H^+} is H^+ axial velocity component in the cell towards the target.
$\Gamma^e(Li)$ has been calculated for each simulation as:

$$\Gamma^e(Li) = \Gamma^e_{evap}(Li) + \Gamma^e_{sput}(Li). \tag{5.5}$$

results are shown in figure 5.12 and 5.13 for the simulation relative to the target temperature and the plasma temperature scan respectively.

In figure 5.14 the ratio between $\Gamma^e_{sput}(Li)$ and $\Gamma^e_{evap}(Li)$ is shown. It is shown that plasma temperature upstream does not influence the sputtering flux, since the ratio with the evaporation flux is almost constant for each run of the plasma temperature scan. This means that only the target temperature plays a role in this ratio. If simulation with higher target temperature had been performed the system would have been in a regime where evaporation had been dominant on sputtering. Unfortunately those simulation could not be carried on due to some oscillatory phenomena explained in chapter 4.

The total lithium flux absorbed by the target $\Gamma^a_(Li)$ is not calculated by the simulation, nevertheless it can be calculated as the difference between the total out flux from the target, $\Gamma^e(Li)$, the net flux from the target: $\Gamma^n(Li)$.

$$\Gamma^n(Li) = \Gamma^e(Li) + \Gamma^a(Li). \tag{5.6}$$

$\Gamma^n(Li)$ can be calculated from the output of the simulation, for each target cell, as:

$$\Gamma^n(Li) = \Gamma(Li) + \Gamma(Li^+) = n_{Li} v_{z,Li} + n_{Li^+} v_{z,Li^+}, \tag{5.7}$$

where, to be consistent with the previous equations the speed is positive if the particle is going to the target and negative if coming from the target.
This type of calculation can be performed only using a Montecarlo code and it's a great advantage in the analysis; if a dynamic code (like B2.5) had been used for neutral particles, the flux of neutral from the wall should have been fixed in order to find a solution to the partial differential equations of the neutral dynamic.

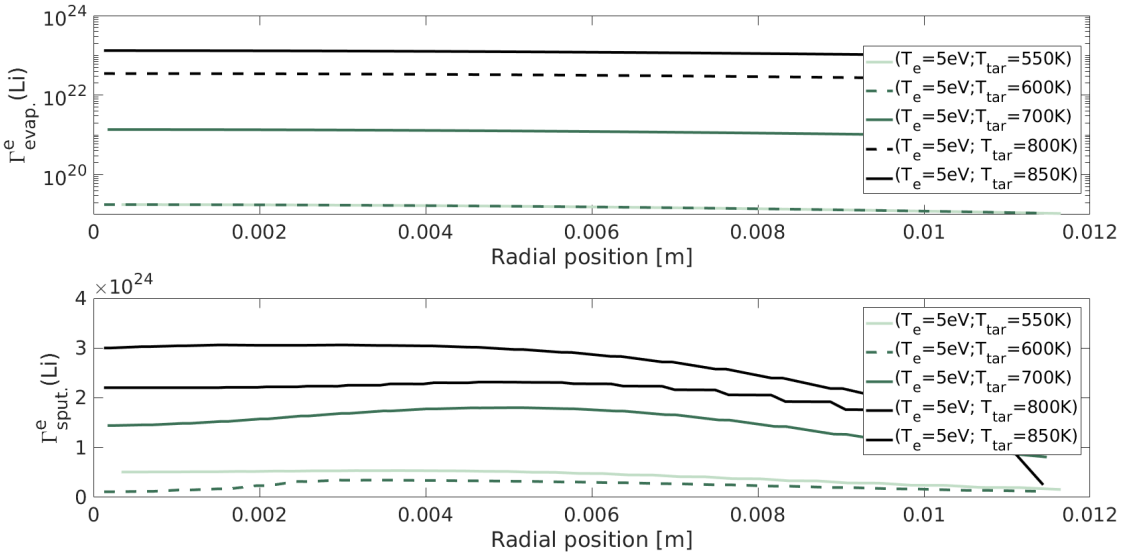

Figure 5.12: Evaporation and sputtering lithium flux from the target in the simulation relative to the target temperature scan (from run030 to run034); lithium flux always increases with target temperature as expected.

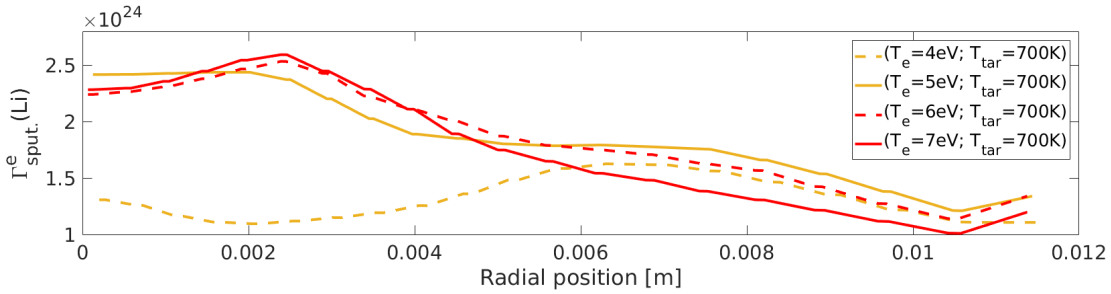

Figure 5.13: Sputtering flux from the target in the simulation relative to the plasma temperature scan (from run036 to run039). Since the target temperature had been 700 K for all the simulation of this scan, the evaporation profile of each simulation is the same for each simulation and it is represented by the curve $\Gamma^e_{evap}(Li)$ relative to the 700 K run in figure 5.12.

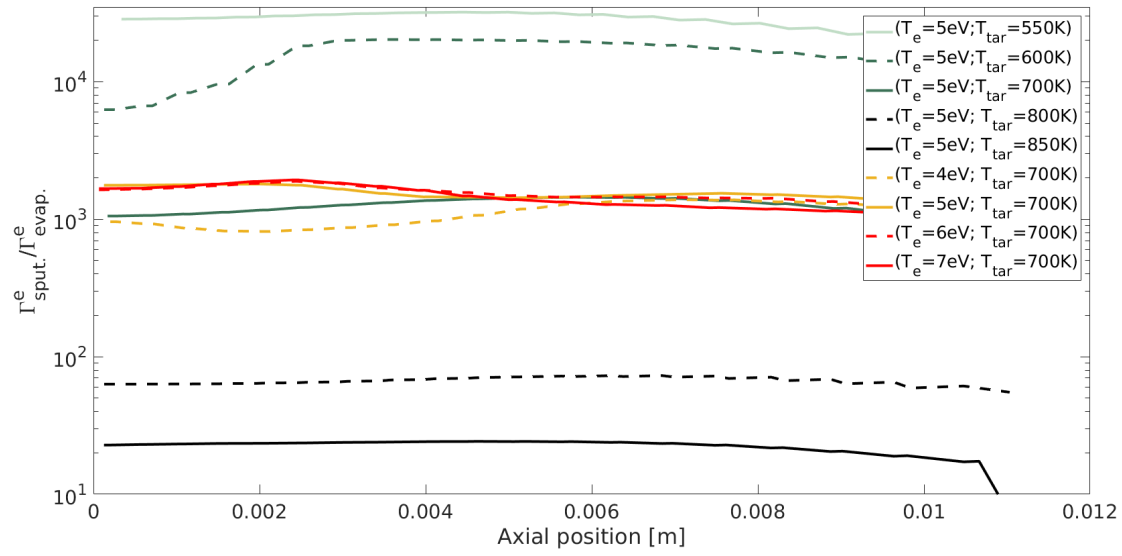

Figure 5.14: Sputtering versus evaporation flux ratio for all the *Magnum-PSI target chamber* runs.

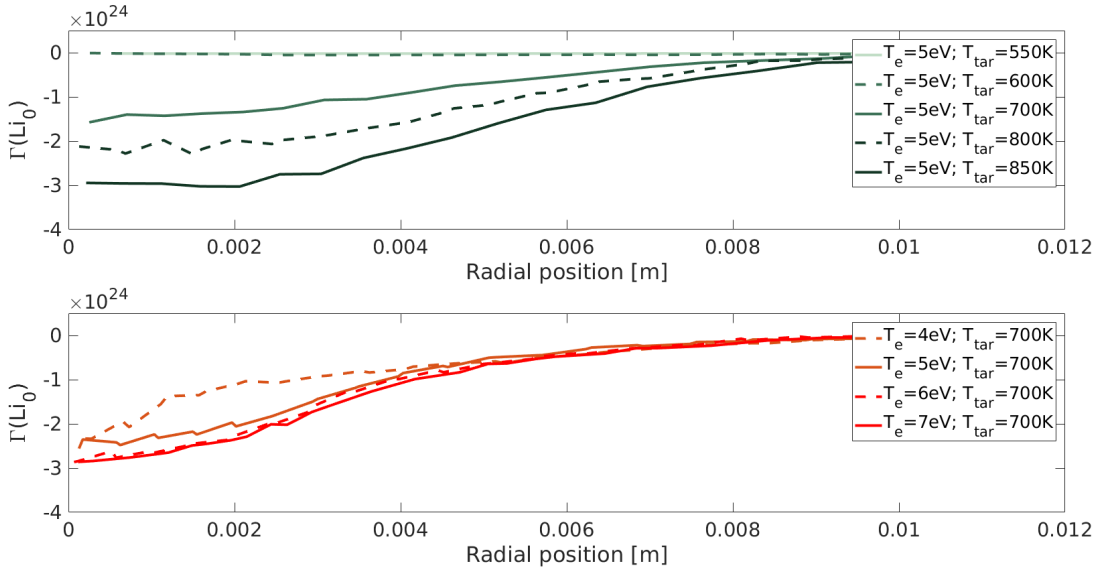

Figure 5.15: Net Li target flux for all magnum target chamber simulations

run	030	031	032	033	034	036	037	038	039
R_{Li}	0.96	0.95	0.83	0.77	0.99	0.94	0.97	0.93	0.98

Table 5.2: Redeposition factors.

With a Montecarlo code the neutral flux from the target determines only the source strength, then density and velocity in a cell are calculated from time in cell and average velocity of the test particles. This way the flux in the target cells is not fixed, in fact, if a lithium test particle is emitted from the target and in the very first cell comes back to the target after an elastic collision with a plasma particle, this test particle will give a non null contribution to the lithium density in the cell but the contribution to v_z will be 0, so the contribution to the net flux from the target will be 0 as well, according to 5.6. For this reason, using absorbing boundary condition on the target guarantees to calculate the net lithium flux.

For each run and each target cell, the two components of $\Gamma^n(Li)$, the neutral and the ion part, have been calculated according to 5.7, results are shown in figure 5.15 and figure 5.16. Obviously Li_0 net flux is negative while Li_+ net flux is positive since only neutral lithium is coming from the target, Li^+ particles in fact are immediately accelerated towards the target by momentum exchange collisions. Once again plasma temperature influence in Li_0 is negligible compared to the influence of target temperature. The shape of $\Gamma(Li^+)$ to the target, in the plasma temperature scan runs, presents a high center that decreases with the temperature, while this does not happen in the target temperature scan. The reason of this behavior will be discussed at the end of the section.

$\Gamma^n(Li)$ is calculated according to equation 5.7, $\Gamma^a(Li)$; then, R_{Li} can be calculated according to equation 5.3; the integrals are calculated multiplying the flux of each cell to the target area fraction represented by each cell.
In table 5.2 the redeposition factors for each run are shown.

As in the experiments two different behaviors are present, a very high redeposition coefficient or a low redeposition coefficient.
It is physically interesting plotting the average plasma temperature $\langle T_e \rangle$ in front of the target (at the end of the simulations) against the redeposition factor of each simulation.
The plot is shown in figure 5.17, the points relative to the target temperature scan are in blue, while

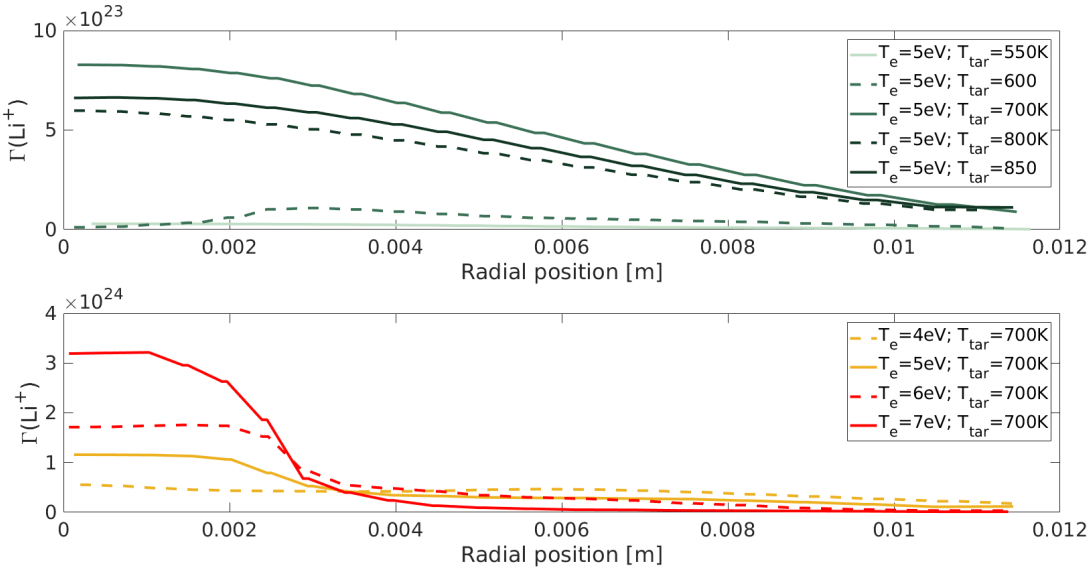

Figure 5.16: Net Li^+ target flux for all magnum target chamber simulations

those relative to the plasma temperature scan are in red. It must be reminded that the T_T temperature scan runs have a narrower energy density distribution, while the electron temperature scan runs have a larger one(see figure 5.1); that every run differs to each other by $T_{T,max}$, $T_{e,max}$ or both and finally that the plasma temperature in front of the target it is not fixed in the simulations but it is a parameter that comes out as a result of equilibrium between Li cooling, plasma temperature upstream and ohmic heating and plasma temperature upstream.

That being said, figure 5.17 shows a correlation between $\langle T_e \rangle$ at the target and the redeposition coefficient. It also shows that the drop off of the redeposition coefficient occurs between 0 3 and 0.4 eV that is exactly the plasma temperature where the crossing point between Li and Li^+ abundance occurs as it is shown in figure 2.4 and figure 2.5.

This phenomenon is hardly experimentally detectable since it requires the measure of the electron temperature in the first millimeters in front of the target. The plasma temperature in fact has its higher gradient in the first millimeters as it will be shown in section 5.2.

For Magnum-PSI specifically, the Thompson scattering lasers and detectors are positioned at the axial position $z = 0$ m, according to the coordinates used in the pictures, about 35 mm far from the target; and there is no correlation between the temperature at that distance and the redeposition coefficient.

The fact that the redeposition coefficient varies and drops down when the average electron temperature is below the temperature of the crossing model brings to a technical and a physical conclusion.

The technical conclusion is that, in order to minimize lithium diffusion in the target region and optimize cooling there is a lower limit to to the plasma temperature in front of the target (the upper limit is given by the stress that the material can handle).

The physical conclusion is that the most efficient cooling process, in order to reduce lithium flux to the target chamber, are momentum transfer collision between beam particles and Li^+ particles. This will be proven and widely discussed in section 5.2.

5.1.3 Energy deposit to the target

Before moving to the analysis of the plasma cooling channels it is needed to check, starting from the output of the simulations, the energy deposit to the target. In future experimental campaign, knowing the energy deposit to the target and the mechanical and thermal characteristics of the target itself it will be possible to establish the amount of heat that needed to be removed by the active cooling in order to reach a certain target temperature.

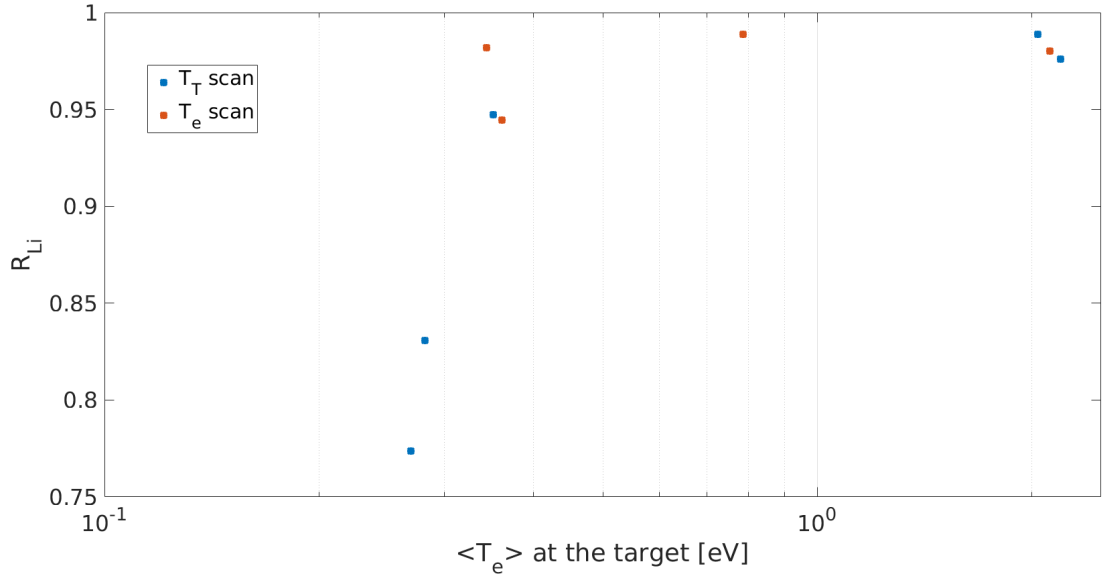

Figure 5.17: Redeposition factor against average plasma temperature in front of the target.

There are two contributions to the energy deposit to the target: the kinetic energy of the plasma particles and the radiative contribution. The radiative contribution has been neglected for two reasons: because the total radiated energy is lower than the energy from plasma particle impact and because, while the plasma particles are directed to the target and so the deposited energy, the line radiation and bremsstrahlung are homogeneously distributed to every angle.

The plasma particle energy flux to the target is calculated as:

$$\Gamma_E^T = \sum_* E_*^T n_*^T v_{z,*}^T \qquad * = \mathrm{H}^+, \mathrm{Li}^+, \mathrm{e}^-; \tag{5.8}$$

where E_*^T is the kinetic energy at the target of the $*$ specie and $n_*^T v_{z,*}^T$ the particle flux.
Since the Debye sheath has been proved to be non collisional, energy is conserved in the Debye sheath as much as the particles flux. Consequently the kinetic energy of the plasma particles can be calculated as the kinetic energy at the entrance of the sheath plus the potential energy difference $\Phi_{W-s} = -\alpha_* \frac{K_B T_e}{q}$.[1]
The particle flux at the target will be the particle flux at the sheath entrance so, according to the theory presented in chapter 3:

$$n_*^T = n_*^s = n_* \exp^{-1}; \quad v_*^T = c_s^* = \sqrt{\frac{K_B T_e}{m_*}}; \tag{5.9}$$

where c_s^* is the sound speed of the $*$ particle and n_* is its main plasma density.
The electrons contribution to energy flux to the target has been neglected due to their mass and to the fact that electron are slowed down in the Debye sheath since the wall is at lower potential than the sheath entrance.
Considering all those assumptions and substituting equation 5.9 into 5.8 the energy flux to the target is calculated as:

$$\Gamma_E^T = \left(e\Phi_{W-s} + \frac{1}{2} m_{H^+} c_s^{H^+}\right) c_s^{H^+} n_{H^+} \exp^{-1} + \left(e\Phi_{W-s} + \frac{1}{2} m_{Li^+} c_s^{Li^+}\right) c_s^{Li^+} n_{Li^+} \exp^{-1}. \tag{5.10}$$

The energy deposit to the target has been calculated for all the simulations according to equation 5.10 using the temperature and plasma density of the cells facing the target. Results are shown in figure 5.18 and 5.19.

[1] In this part of the analysis the same notation that had been used in chapter 3 about the Debye sheath was used

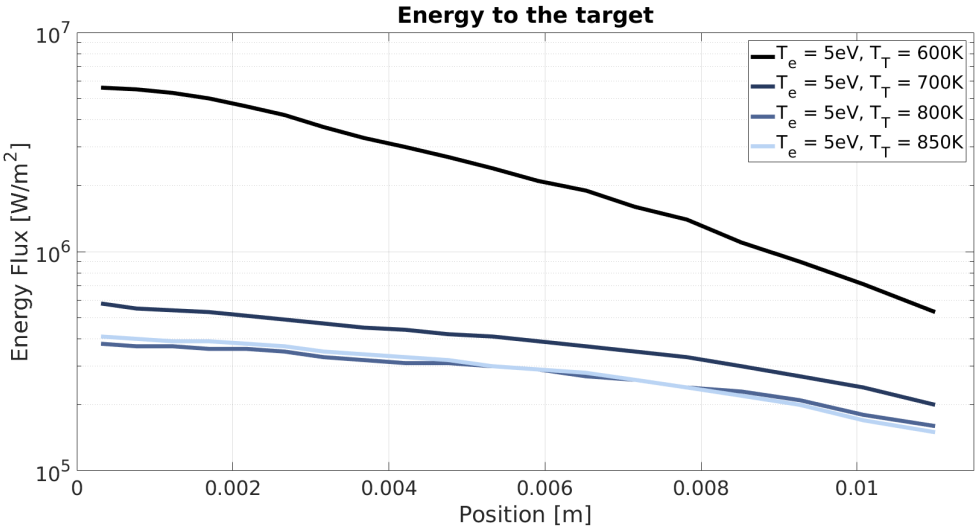

Figure 5.18: Plasma energy deposit to the target for the target temperature scan runs. The energy to the target is reduced with the increasing of Li flux (target temperature), until it saturates at about $4 \times 10^5\,\mathrm{W/m^2}$.

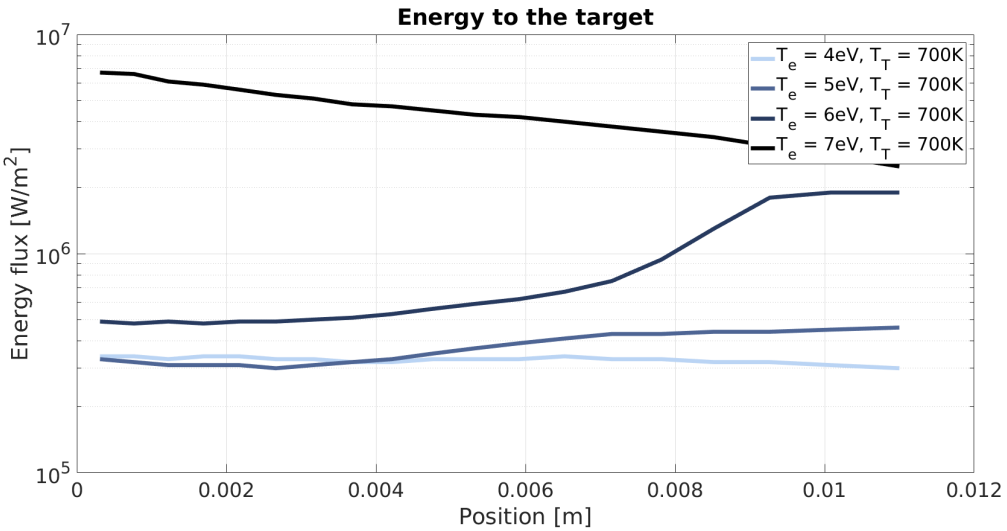

Figure 5.19: Plasma energy deposit to the target for the plasma temperature scan runs. The energy to the target is reduced with the decreasing of plasma temperature upstream, until it saturates at about $4 \times 10^5\,\mathrm{W/m^2}$.

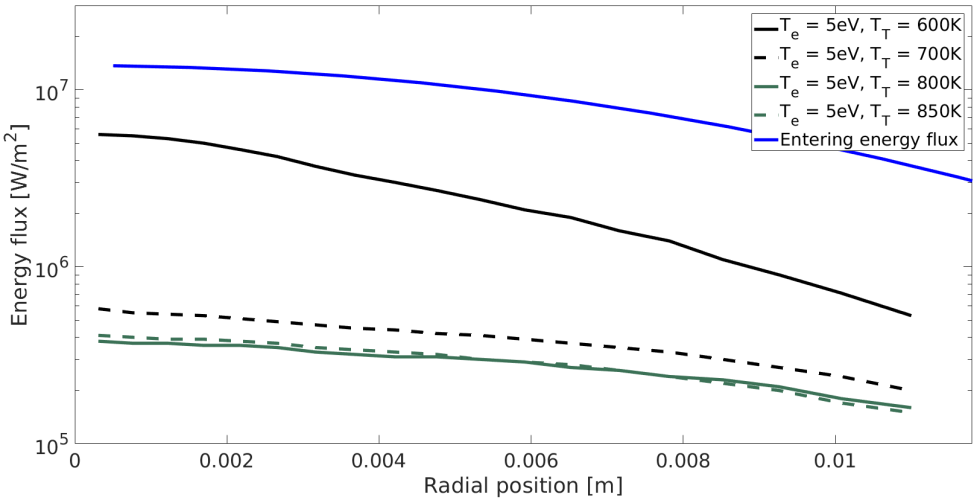

Figure 5.20: Plasma energy to the target for the target temperature scan runs compared to the energy entering the system.

The figures show that the energy to the target is reduced with the increasing of the target temperature and with the decreasing of the plasma temperature upstream as expected. Energy flux is always reduced at least to $1\,\mathrm{MW/m^2}$ but in runs where the conditions have been pushed to the limit like the run with $T_{Tar} = 600\,\mathrm{K}$ or the plasma temperature up to $7\,\mathrm{eV}$ at less than $30\,\mathrm{cm}$ from the target. In next discussions the fact that, when plasma temperature is reduced to $0.4\,\mathrm{eV}$, the energy flux to the target is less than $1\,\mathrm{MW/m^2}$ will be very important; $1\,\mathrm{MW/m^2}$ is a energy flux that can be handled by tungsten plates.
As a comparison, the plasma energy flux entering the system upstream is calculated calculated according to equation 5.11:

$$\Gamma_E^u = qT_{H^+}^u n_{H^+}^u v_{z,H^+}^u + qT_e^u n_e^u v_{z,H^+}^u; \tag{5.11}$$

where T_{e/H^+}^u are the e^- and H^+ temperature (in eV) upstream and n_{e/H^+}^u and n_{e/H^+}^u are their relative density and velocity profiles upstream. The radial energy flux profile at the entrance of the chamber, for all the runs of the target temperature scan, is shown in figure 5.20. By comparing it with the energy deposit to the target (see figure 5.20) I show that energy to the target can be reduced by more than a order of magnitude before saturating.

The main result is that the energy deposit decreases saturating to 30-40 $\mathrm{kW/m^2}$, then, even having a higher lithium density, the energy to the target decreases very slowly. The reason of this behavior can be found by looking at the axial distribution of the plasma temperature. The axial distribution is shown in figure 5.21. The figure shows the projection, parallel to the beam axis, of the electron temperature $2\,\mathrm{mm}$ far from the beam axis. For every different run it is clear that the plasma temperature, after having been reduced to $0.4\,\mathrm{eV}$, then it start decreasing much slower. This saturation of the cooling can be interpreted as the moment when the cooling per particles that diffuses out of the plasma decreases. In fact higher lithium flux guarantees lower plasma temperature only until the temperature in reduced to $0.4\,\mathrm{eV}$.
This is the same energy limit that has been found for the recombination coefficient and in fact, in the following section it will be proven that it is related to both cooling and redeposition.
The plasma temperature heavily influences the energy to the target since from equation 5.10 it's found that $\Gamma_E^T \propto T_e$. Since for those runs the plasma temperature in front of the target is very similar (at least in the central part of the target) the energy deposit to the target is almost the same. When the plasma temperature is not reduced to that limit the energy flux to the target quickly increases.

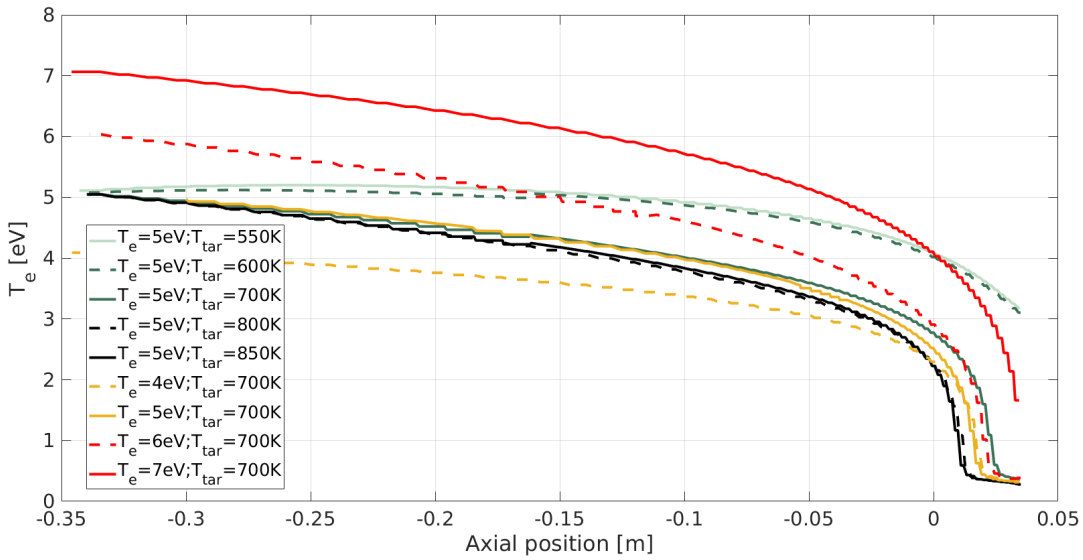

Figure 5.21: Axial temperature profile in different runs.

5.2 Cooling channels and lithium confinement

In this section some of the phenomena, like the redeposition behavior, the two lithium transport channels and the plasma axial temperature that had been described in the previous section will be explained and discussed.
Plasma temperature in fact has its higher gradient in the first millimeters in front of the target as shown in figure 5.21; anyway it has been found that the temperature drops quickly to 0.4 eV and then decreases much slower. This is related to the relevance of the different cooling channels.
To understand which cooling channel is the most relevant the axial projection of some plasma and neutral quantities are shown in figure 5.22, 5.23 and 5.24. The run that has been chosen to carry on this analysis is run031 since the plasma temperature reaches the limit of 0.4 eV and closer to the target it presents the saturation on plasma temperature shown in figure 5.21. Anyway it will be shown that each run shows similar behaviors.
The following images show only the part of the axis profile closer to the target (positioned at $z = 0.035$ m), since, as shown in figure 5.21, the great part of the cooling occurs in the first centimeters from the target.
In figure 5.22 the radial projection of Li and Li^+ density are plotted together with the plasma temperature. It is clear that the cooling happens at the exact point where the ionization occurs. This behavior suggests that the major cooling contribution is lithium ionization. Another component of electron energy loss, related to ionization, it is the thermalization of electrons and Li^+ generated after the ionization. The only Li^+ density source is in fact electron ionization: the original Li particle, that comes from the target and has a temperature much lower than the electron temperature, is ionized ; electrons spend part of their energy to heat Li^+ and e^- generated by ionization. Nevertheless the thermalization of a plasma species by other plasma species is not a net plasma cooling contribution since it is just a energy transfer and that heat is going to be deposited to the target anyway.
The reason why the crossing point between n_{Li} and n_{Li^+} happens at slightly higher energy (farther from the target) than in the CR model is due to the fact that the CR model was a zero flow model while in the simulations Li flux high is high and Li penetrates more in the plasma.
To prove that the most relevant cooling channel is ionization, and to quantify its relevance, in figure 5.23 the electron energy source, S_{T_e} is plotted together with the Li^+ density source: $S_{n_{Li^+}}$. It appears that the electron energy loss has a (negative) peak specular to the ionization peak. The ionization peak is located where electron temperature is between 1 and 0.5 eV.

In order to quantify the importance of ionization as plasma cooling channel, its contribution to S_{T_e} is

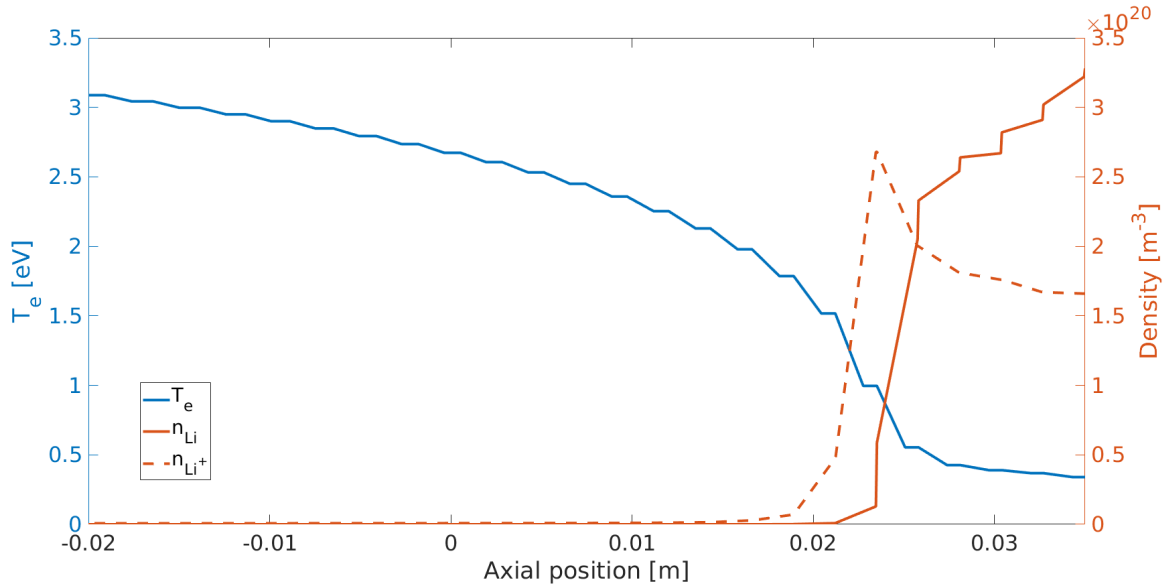

Figure 5.22: Plasma temperature and lithium density axial projection in run031.

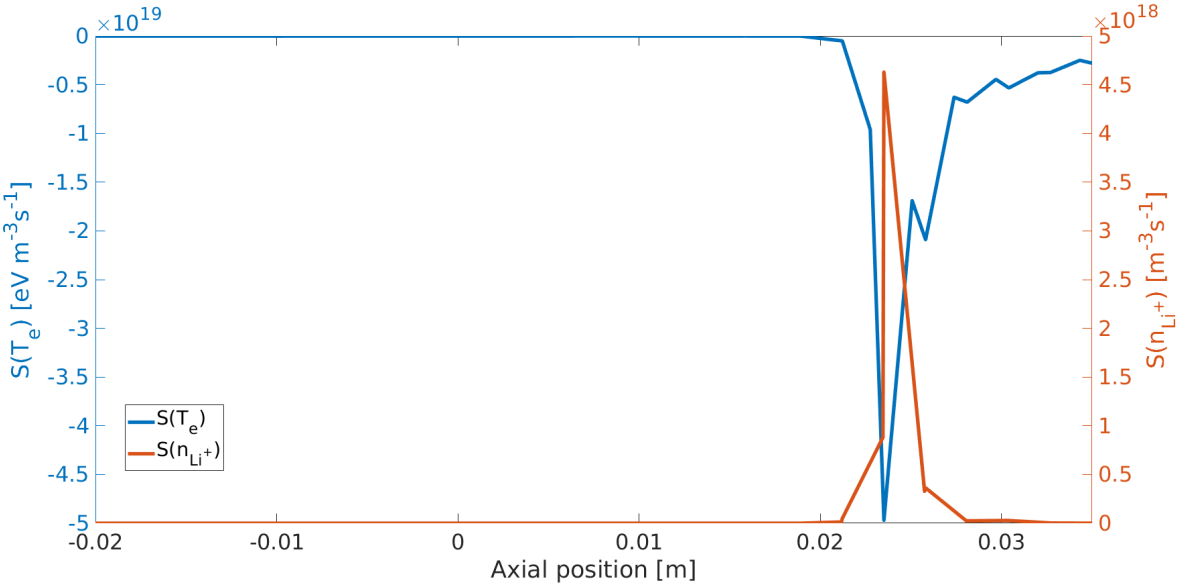

Figure 5.23: Axial projection of electron energy source compared to Li^+ density source in run031. Lithium density source is specular to electron energy source

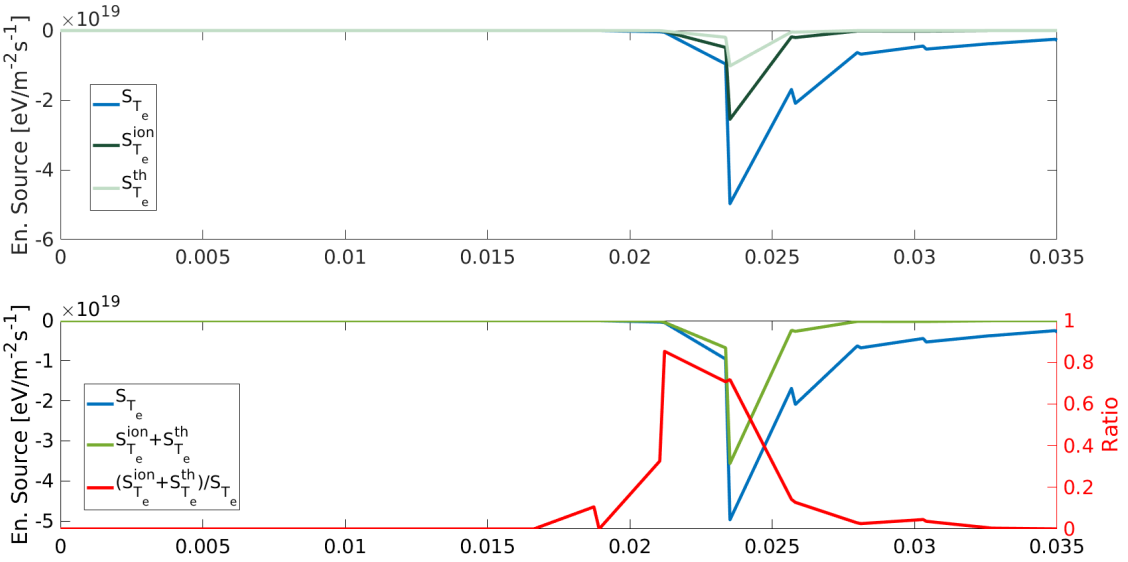

Figure 5.24: Axial projection of S_{T_E} and its major contributions $S^{ion}_{T_E}$ and $S^{th}_{T_E}$ in run031.

calculated. It must be underlined that the total S_{T_e} includes the contributions from all the reaction reported in blue in table 2.2. In figure 5.24 the ionization contribution to the the electron energy loss $S^{ion}_{T_e}$ as much as the thermalization contributions $S^{th}_{T_e}$ are plot together with S_{T_e}. $S^{ion}_{T_e}$ is calculated as follows:

$$S^{ion}_{T_e} = -E_{ion} S_{n_{Li^+}}, \tag{5.12}$$

where $E_{Ion} = 5.40\,\text{eV}$ is the first ionization energy of lithium. It has to be underlined that calculating ionization electron energy loss I am underestimating its impact on plasma cooling. The reason of this statement is the fact that the amount of ionization collisions is underestimated by $S_{n_{Li^+}}$ that is the difference between ionization and recombination collisions; the real energy dissipated by the electrons through lithium ionization is proportional to the number of ionization collisions per second per cubic meter that is higher than $S_{n_{Li^+}}$.
$S^{th}_{T_e}$ is calculated as:

$$S^{th}_{T_e} = -2T_e S_{n_{Li^+}}, \tag{5.13}$$

since the Li^+ particles are almost frozen compared to the plasma particles and have to be brought to the equilibrium electron temperature; the 2 is due to the fact that both electrons and ions need to be thermalized.
Results are shown in figure 5.24 where the two components are shown in the first picture. In the second picture the sum of the two components is plotted together with the total electron temperature loss and the ratio between the two.
Figure 5.24 shows that the two components are responsible for the majority of plasma cooling specially at the S_{T_E} negative peak and it is calculated to be the main plasma cooling contribution even if the calculation underestimates it.
Closer to the target the plasma temperature is lower and so $S_{n_{Li^+}}$ decreases, even if it must be said that in this region it is even more underestimated since recombination plays a bigger role. This is the region where electron temperature stops decreasing fast since only the minor contributions to plasma cooling are present here. In this region $n_{Li} > n_{Li^+}$ and that is where line radiation is higher. For this reason an interesting experimental validation would be a scan in $2\,\text{p} \rightarrow 2\,\text{s}$ line radiation to understand if n_{Li} drops down exactly where electron temperature drops down as shown in figure 5.22.
The relevance of ionization in lithium plasma cooling as been proven for run031 but the same behavior is shown in every run.
In figure 5.25 and 5.26 electron temperature energy source and Li^+ density source in the first centimeters out of the target in run032 and run039 are shown. Those runs have different target temperature, and

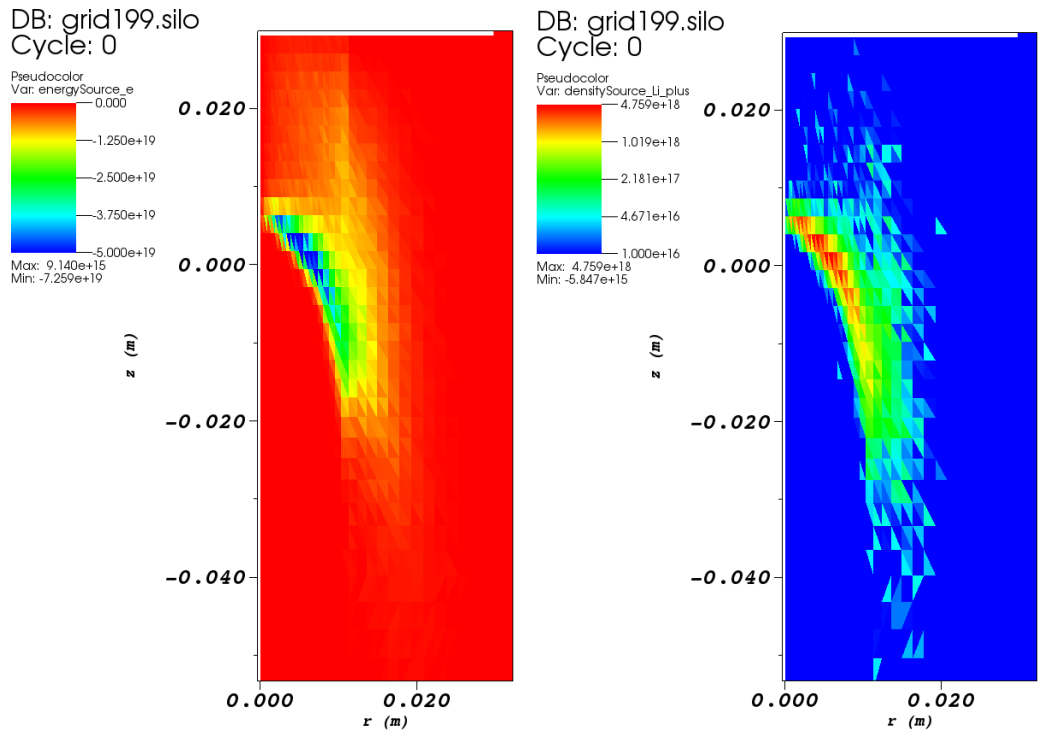

(a) (b)

Figure 5.25: Electron energy source and Li^+ density source in run032

plasma temperature peak and profile, nevertheless they show the same behavior described for run031: the negative energy source peak corresponds to Li^+ density source.

5.2.1 Lithium confinement

It has been shown that neutral lithium is limited to the plasma zone where the plasma temperature is lower than 0.4 eV. This is the reason why the redeposition drops at that temperature, the neutral lithium is able to cross a low temperature zone and escape the plasma beam. On the other hand, if lithium is ionized, radial transport is limited by the magnetic field while and Li^+ axial transport is heavily limited by momentum exchange collisions with the plasma beam.
What makes the difference in terms of lithium efflux from the target area is the distance from the target where plasma temperature drops or, from lithium point of view, where Li density increases. Comparing lithium density in the target temperature runs (figure from 5.2a to 5.5a) it is evident that the higher the target temperature, the farther from the target the plasma temperature drop takes place; but if lithium flux from the target is high enough to reduce plasma temperature to 0.4 eV and form a lithium cloud in front of the target, the density of the lithium cloud is not strongly dependent on lithium flux from the target and it varies from 10^20 to $1 \times 10^{21}\,m^{-3}$ even if between a 700 K and a 850 K target lithium flux varies by more than two orders of magnitude.

Comparing target temperature scan run with plasma temperature scan runs it is also possible to compare the impact of plasma temperature distribution; it must be reminded that plasma temperature scan runs have a temperature profile 80% wider than the previous runs.
Run031 and run036 can be compared since their only difference is plasma temperature profile width. In figure 5.7c plasma temperature in run036 is shown. The fact that the temperature profile upstream is larger allows the plasma beam to reach the target holder (the zone hit by the beam next to the liquid lithium target) with a temperature higher than 0.5 eV. On the other hand in run031 plasma temperature at the target holder is below that limit as shown in figure 5.3c. This is the reason why the lithium cloud in front of the target is different in run031 and run036, even close to the beam axis

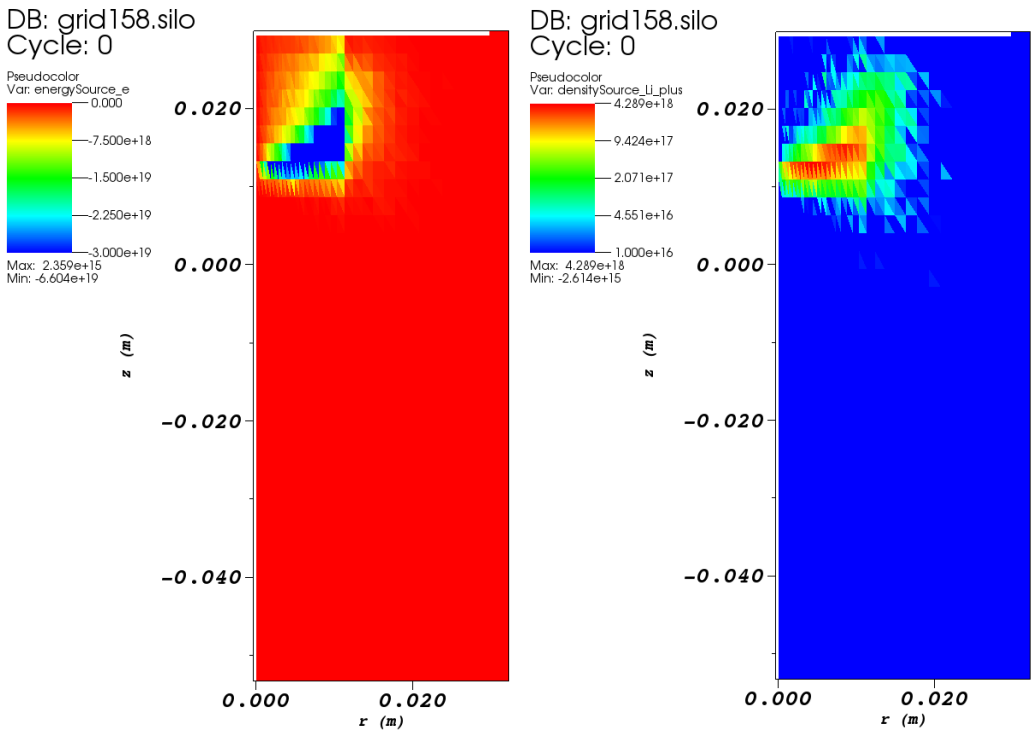

(a) (b)

Figure 5.26: Electron energy source and Li^+ density source in run039

where the temperature upstream is similar between the two runs.
Thanks to the high plasma temperature at the sides lithium is confined in front of the target, and creates a bigger cloud that cools the plasma even more than with the narrower plasma beam. some lithium jet is present even in run036, since the plasma is partially cooled by incoming lithium particles, but the relevance of the plasma jet lithium transport is comparable with the ionization/recombination transport that I have already proven to be generally weak.
With even higher target temperature lithium is even more confined and plasma jet disappears in figure 5.8a and 5.9a.

Lastly Li^+ transport through the beam has to be compared in the different configurations.
In figure 5.27 and figure 5.28 lithium axial profile is plotted for the different runs. It is shown that close to the target Li^+ density reaches a flat top as much as the Li density. Li^+ flat top density value is comparable to the Li density value; the reason is that, since electron temperature decreases slowly after reaching the CR model crossing point, Li and Li^+ density is equal.
Li^+ density then decreases rapidly due to momentum transfer collisions until it reaches a value that depends on the peculiarity of every single run.
This behavior will be checked in next chapter because, since the geometry of the simulation is very short, the results on Li^+ density upstream can be influenced by the boundary conditions.

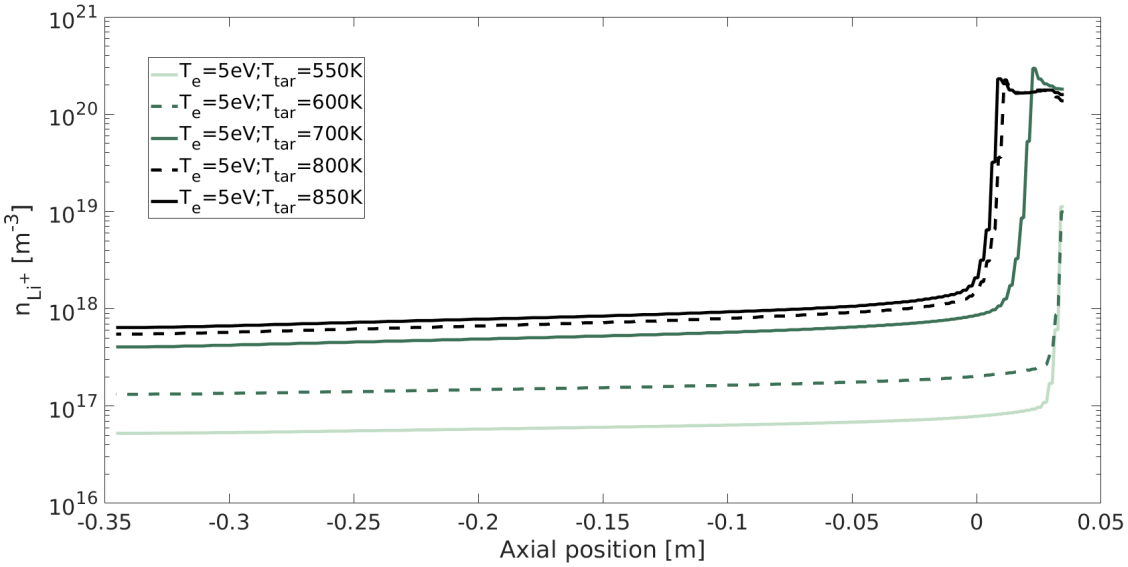

Figure 5.27: Axial projection of Li^+ density in target temperature scan runs.

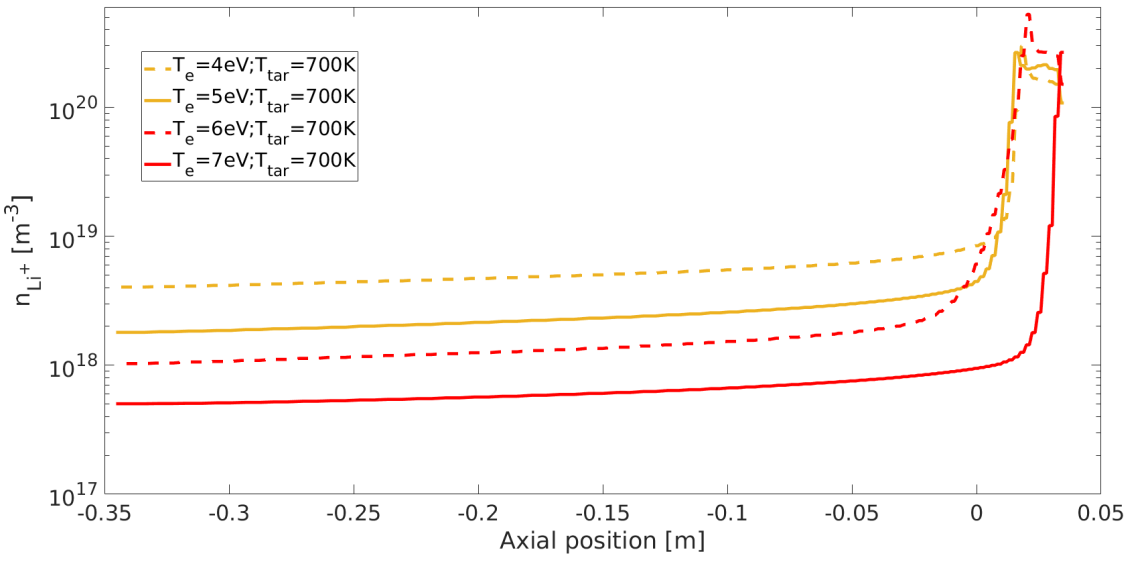

Figure 5.28: Axial projection of Li^+ density in plasma temperature scan runs

Chapter 6

Comparison with previous simulations

In this chapter the outcome of simulations performed with total Magnum-PSI geometry will be compared to previous simulations performed with B2.5 standalone[20] and Eunomia standalone [6]. In those simulations the lithium target has been simulated as big as the entire target holder (diameter of 6 cm) because this had been the same geometry implemented in the previous standalone simulations that I will analyze.

6.1 B2.5 standalone

Lithium was implemented in B2.5 standalone by Mike Machielsen in his thesis work at Differ[20]. In his standalone simulation neutral lithium flux into the plasma beam was treated by a dynamic model, a source was set at the target and lithium flux into the chamber was a free parameter. The H and H^+ background density was chosen as a input parameter of the simulations as well.
One of the biggest difference with the coupled simulations I run was that the only section of Magnum-PSI that was simulated was the plasma beam, the inner part of the chamber. The reason of this limitation is due to the fact that B2.5 can be defined only where the plasma beam is.
In figure 6.1a and figure 6.1b Li density and Li^+ density are shown in simulations that were performed with different lithium flux from the target. The figures show two peculiarities: absence of lithium cloud, even with very high plasma fluxes, and exponential decay of lithium density in the plasma.
In figure 6.2 electron temperature and Li^+ density is compared for different lithium flux values from the target. Those simulations show the same two behaviors that were described for the previous runs. Since the neutrals description in the B2.5 standalone code is made by a dynamic model, the exponential decay of lithium density simply shows the probability of reaching a certain point in the beam after having been emitted from the target.

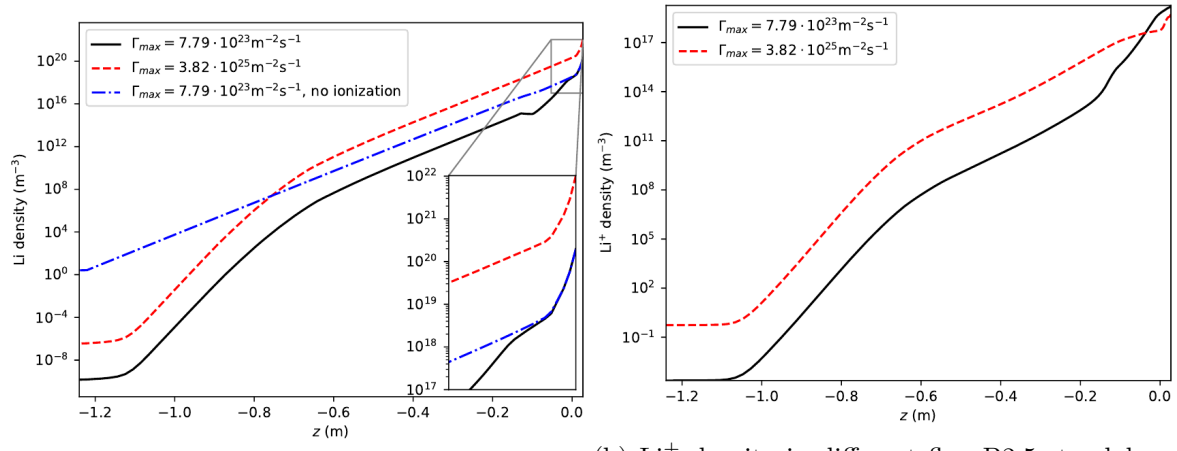

(a) Li density in different flux B2.5 standalone runs (b) Li^+ density in different flux B2.5 standalone runs

Figure 6.1: Standalone B2.5 run output.

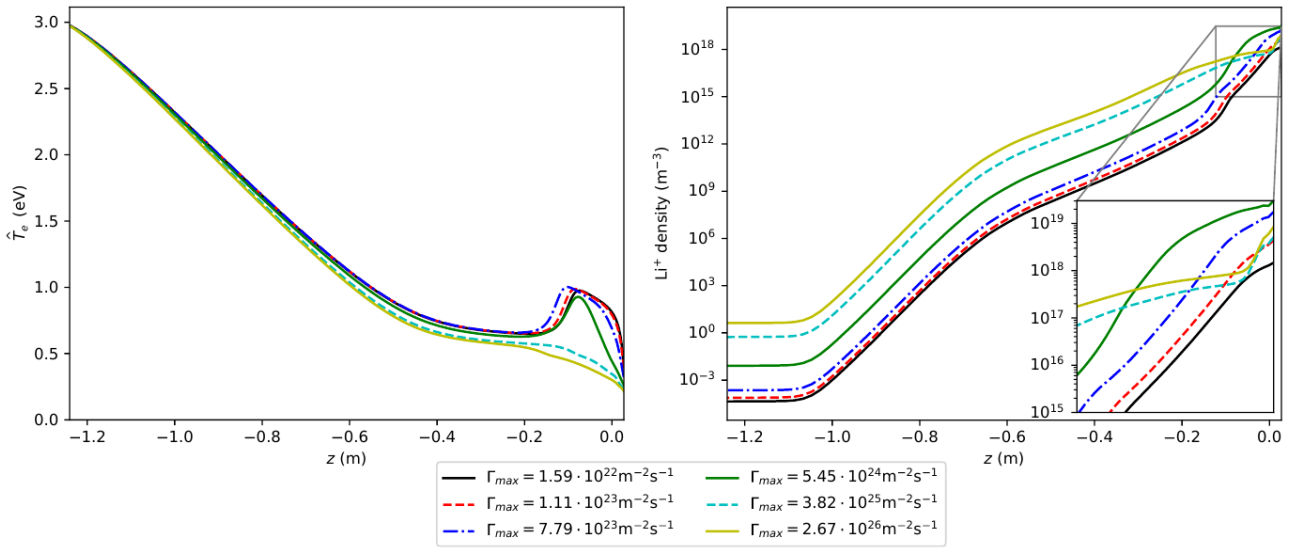

Figure 6.2: Axial projection of electron temperature and Li^+ density in B2.5 standalone runs with different Li fluxes from the target.

In order to compare lithium transport and cooling in standalone runs with coupled runs, a coupled run was performed using the same plasma input parameters that had been used in the standalone runs. The implemented collisions were also the same, while the lithium flux was kept at about $10^{24}\,m^{-3}s^{-1}$. Lithium flux from the target could not be completely fixed since one of the two flux effluent components, sputtering, depends on plasma flux. The target temperature, the real input parameter for coupled runs simulations was set to 700 K in order to reach the required lithium effluent from the target.
Li density in Magnum-PSI geometry, from coupled run is shown in figure 6.3a, while the axial projection of Li^+ density in the center of the beam is shown in figure 6.4; in the same figure Li density out of the beam is shown as well.

It's clear that lithium transport in standalone and coupled simulations is completely different. In the coupled run the lithium cloud in front of the target is evident, and neutral lithium particles are able to cool down the plasma beam to a temperature lower than 0.5 eV in the entire target chamber. Lithium density in even higher than in the previous chapters because of the low plasma temperature upstream, 3 eV, the narrow plasma temperature width, 5 mm, and the lower plasma density, $10^{19}\,m^{-3}$.

The reasons of the big differences between the two results are the neutral lithium modeling and the simulated geometry.
In the standalone runs lithium density at a certain distance from the target is given by the probability that a neutral lithium particle can go so deep into the plasma beam. With this approximation the possibility of recombination, following the ionization of an emitted Li particle, is not considered.
This is the reason why there is no Li cloud in front of the target. As it has already been proven with the coupled runs, in the lithium cloud the plasma temperature is approximately the temperature relative to the cross point of Li and Li^+ abundance in the CR model. For this reason in that region lithium particles continuously make ionization or recombination collisions. But if, for neutral particles, only the loss term is considered, the density can only start dropping exponentially even from the first centimeters out of the target. The exponential decay of lithium density shows that only neutral particles loss is considered, the exponential decay reflects the Poisson probability of not making any ionizing reaction till a certain point in the plasma.
From image 6.3a it is also evident that Li transport along the beam mainly takes place in the low temperature zone of the beam. The comparison of the two Li density profile (standalone and coupled) together with the low Li^+ density source term in coupled runs indicates that lithium transport upstream mainly takes place in the low plasma temperature-low plasma density zone where ionization and recombination of lithium particles continuously takes place.
This ion transport because of magnetic confinement has a privileged direction along the axial direction

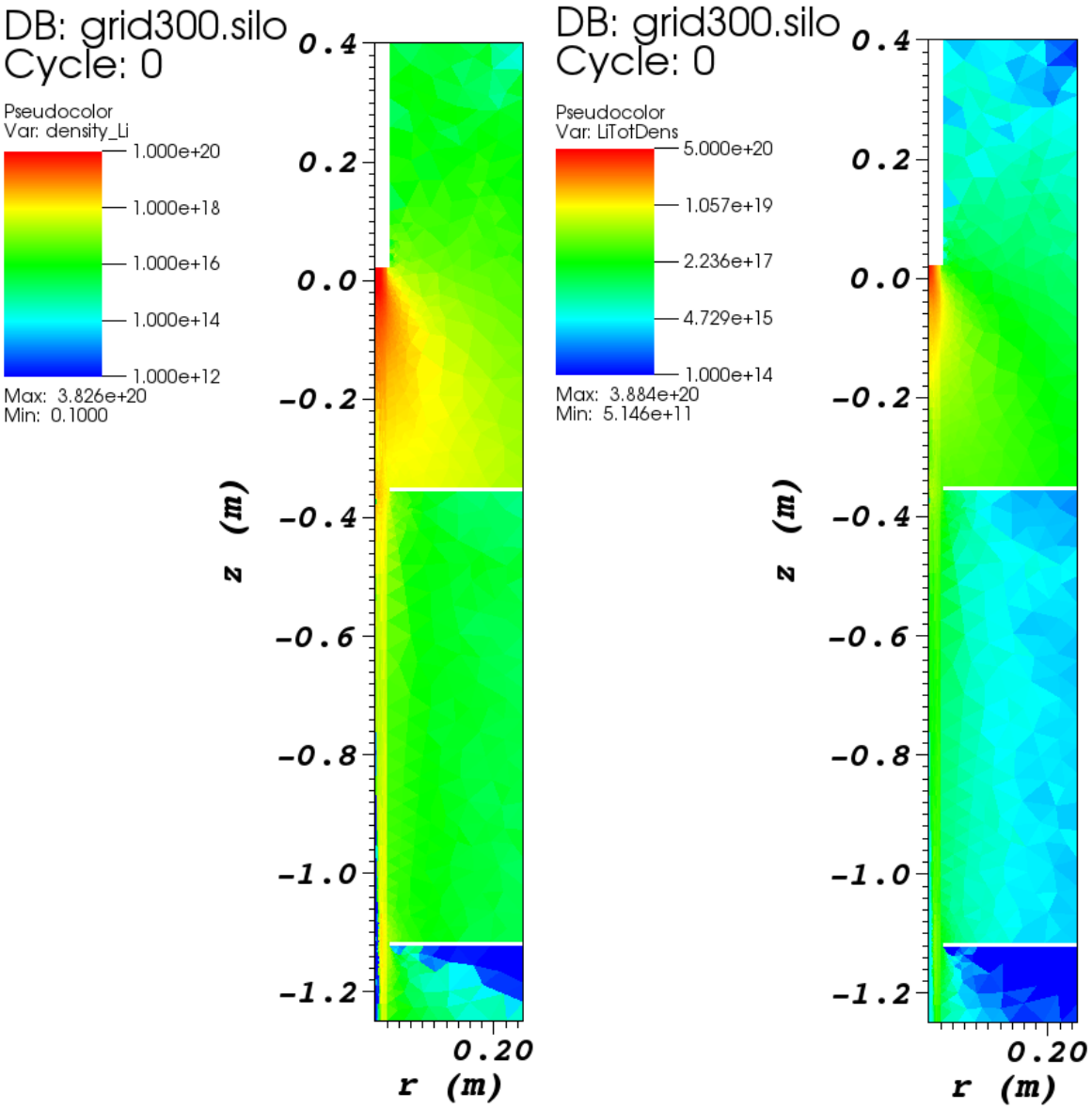

(a) Li density.

(b) Lithium total density, $n_{Li} + n_{Li^+}$

Figure 6.3: Output of coupled run using the same input and boundary conditions that were used in the standalone runs.

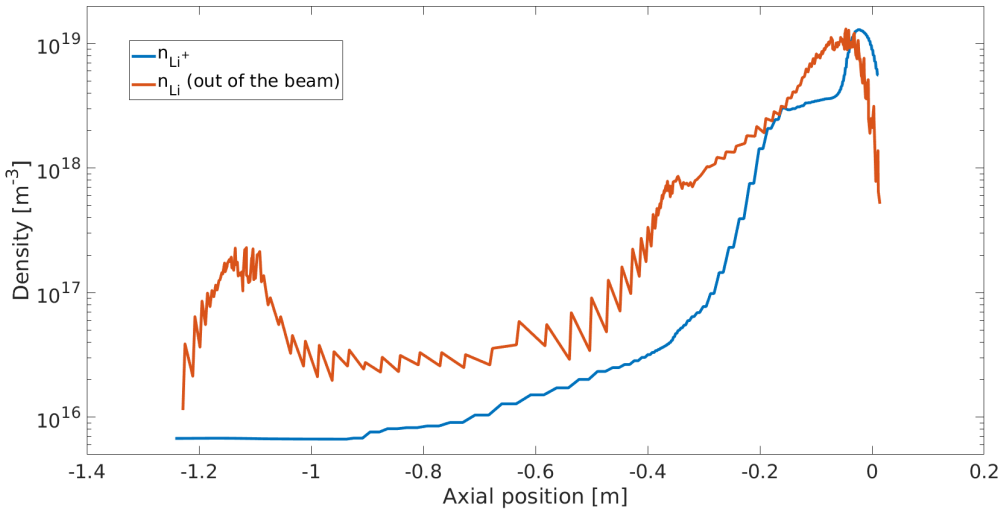

Figure 6.4: Axial projection of Li^+ density in a coupled B2.5-Eunomia run.

and because of recombination reactions also Li transport is higher in that direction . This way lithium particles can diffuse and cool the plasma beam also upstream.

The difference between the two standalone and coupled geometries also plays a role since in the coupled simulation lithium particles are allowed to exit the beam area and then to come back after a certain amount of collisions. This is also a lithium transport channel upstream.
The main effect of those two transport channels, that will appear also in further simulations, is the saturation of Li^+ density in the beam upstream. The reason of this saturation value is the high neutral density close to the beam and in the outer part of the beam. Li density profile out of the beam is shown in figure 6.4 in red. When neutral lithium diffuses in the beam, it is ionized and Li^+ density increases. This is also clear is figure 6.3b where the total lithium density, calculated by summing neutrals and ions density, is shown.

6.2 Eunomia standalone

A similar comparison was done with Eunomia standalone simulations by using the same boundary conditions in the coupled and standalone runs. The collisions implemented were the same. For this simulation a $T_{e,max} = 5\,\text{eV}$ plasma profile was chosen as boundary condition. The target temperature is set to 700 K in both runs and the target diameter is again 6 cm.
Lithium output density for the standalone run is shown in figure 6.5a while electron temperature is plot in figure6.5b.
The main difference between the coupled and the standalone run is that the plasma temperature can not decrease in front of the target because is fixed; so neutral Li is confined in the first millimeters out of the target in the region where $T_e < 0.4\,\text{eV}$ and its immediately ionized out of the target. A guess has to be made on Li^+ density velocity and temperature distributions. For this reason no lithium cloud is formed in front of the target and a small lithium jet is possible only on beam sides where the plasma temperature is lower.

In the simulation shown in figure 6.5, plasma at the entrance of the target chamber has almost the same temperature distribution that was set in run036, but the output of the standalone simulation is completely different and lithium density in the standalone simulation is orders of magnitude lower than in the coupled run even if the lithium target is larger in the standalone simulations. For this reason the two results are so different that can not be compared simply because of the absence of lithium effects on plasma.

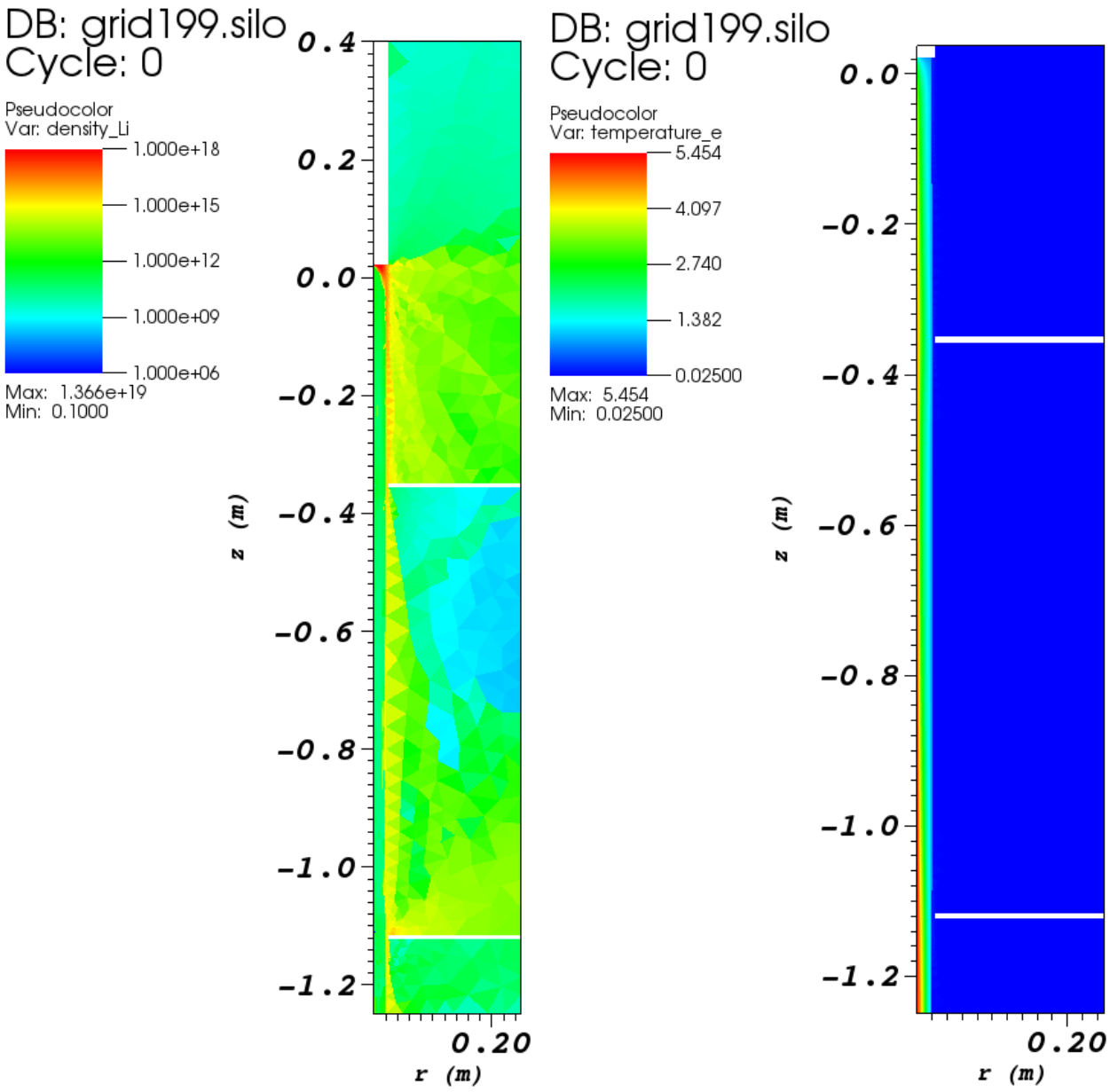

(a) Eunomia standalone lithium density run output (b) Eunomia standalone electron temperature input

Figure 6.5: Eunomia standalone results.

Chapter 7

Total magnum geometry, the vapor box and other possible fusion applications

7.1 Total Magnum-PSI geometry

Simulations with Magnum-PSI total geometry were run to quantify lithium flux to the different chambers of Magnum-PSI and to understand the importance of different lithium transport channels. Simulations with total Magnum-PSI geometry can also give predictions on lithium transport in a vapor-box because its geometry is similar to the one of a vapor-box: the total volume is divided in different chambers/boxes. To understand the influences of different numbers of vapor chambers two different geometries were used: the total Magnum-PSI geometry described in figure 3.2 and a second geometry where the heating chamber of Magnum-PSI was divided in two chambers; this way the this alternative geometry will be made of four chambers.
The simulations have the same physical input parameter and boundary conditions: the lithium target temperature is set to 700 K and the lithium target is simulated to be as big as the entire target holder; plasma temperature and density upstream are equal and with a temperature peak at 5 eV in both simulations.
The pumps ore positioned in three different walls: the last wall of the *Magnum target chamber geometry*, as it was in the previous simulations; the external wall of the heating chamber and the external wall of the source chamber.
Results for the Magnum-PSI total geometry are shown in figure **??**, results for the alternative geometry run are shown in figure 7.2.
The figures show that lithium density upstream is slightly reduced with the alternative geometry. The Li^+ density saturation value upstream is slightly reduced as well.
The reason why lithium transport is not highly reduced by adding a inner wall is due to the distance between the inner walls and the plasma beam.
In figure 7.3 a zoom on the inner walls zone is shown. On the left side of the image the plasma temperature is shown, on the right side of the image the lithium density is shown. It' clear that lithium transport upstream is not reduced because lithium can pass through the low plasma density region and the region between the plasma beam and the internal wall.
For geometrical and numerical reason it is not possible to increase the internal wall length to the plasma beam but this seems to be the ideal solution to reduce lithium transport upstream.
In order to reduce lithium transport in the vapor-box some solutions are proposed in the next sections.

7.2 Proposed solutions

According to the results of the simulations that were shown in chapter 5 and section 7.1, some solutions for divertor plates and vapor box geometry are presented.

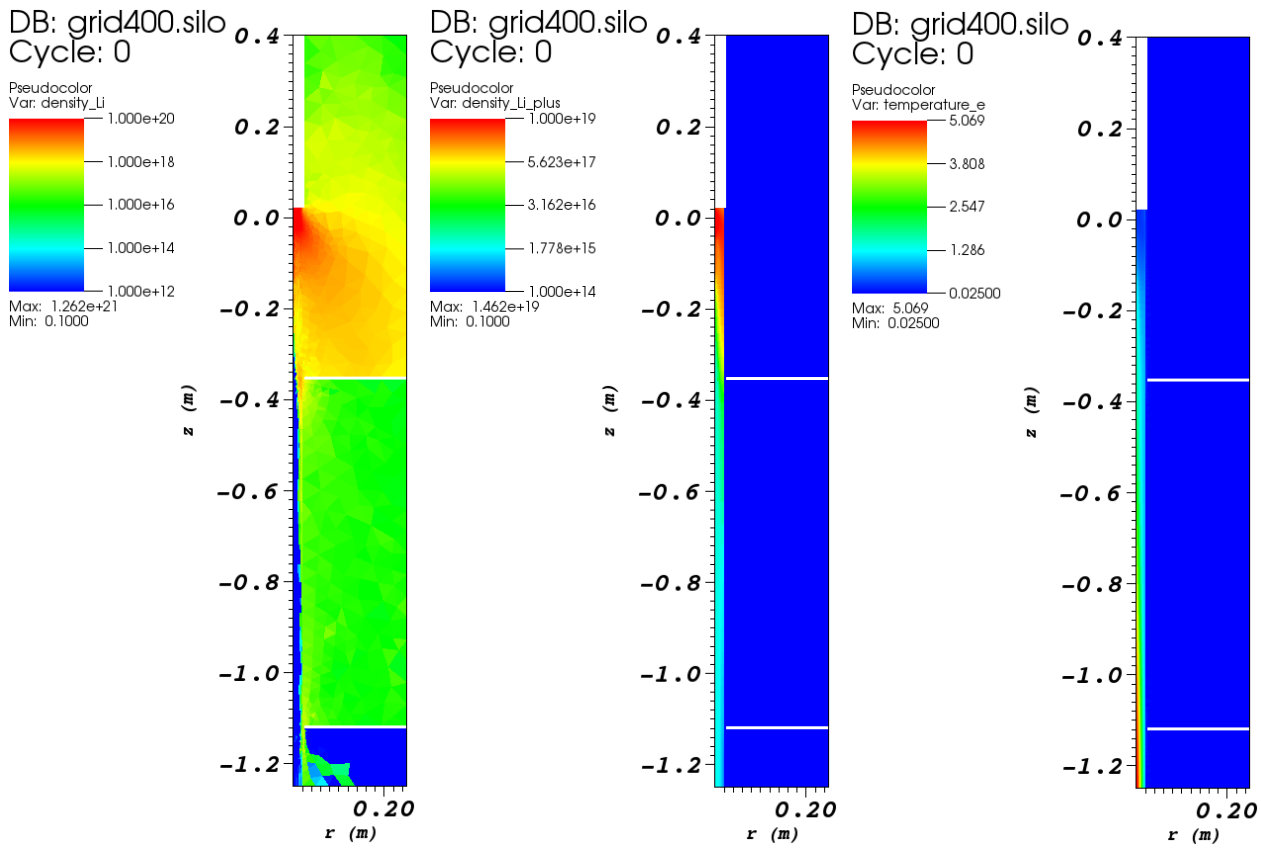

(a) Li density (b) Li^+ density (c) T_e

Figure 7.1: Results obtained using total Magnum-PSI geometry

7.2.1 Vapor box geometry

In chapter 5 and chapter 7 it was proven that lithium transport upstream (with considering both Li and Li^+ density) is mainly due to lithium transport out of the plasma or in the low density-low temperature beam region. Lithium diffusion after ionization continues inside the beam and is responsible for Li^+ density saturation regime upstream.
In order to limit this type of transport a solution for the vapor box geometry is proposed; a sketch is shown in figure 7.4.
In figure 7.4 the plasma beam is in yellow, the temperature in higher in the middle of the beam (left hand side of the image) and is lower in the outer part; in black the outer and inner walls of the vapor box; the brown part represent the lithium cloud.
The idea is the inner part of the vapor-box to intercept the low energy-low density tails of the incoming plasma. With this solution the lithium coming from the target, that can diffuse in the first box of the vapor-box (upper part of the image), when diffusing to the successive boxes of the vapor-box either hits the wall of the vapor-box or encounters the part of the plasma beam that has gone trough the inner-wall of the vapor-box. The idea is sizing the inner wall of the vapor-box in order to intercept the low plasma temperature tail where plasma temperature is below 0.4 eV; this way the inner walls of the vapor-box are part of the divert because they absorb directly a fraction of the plasma energy.
With this geometry lithium particles are ionized before leaving the first box; once it has been ionized lithium particles are immediately pushed back by ion-ion momentum exchange. This lithium particles have a physical barrier, the inner wall and the plasma beam, that should reduce lithium flux upstream. A lower Li density in the following boxes will give a lower Li^+ saturation value upstream.
The major physical limit of the proposed geometry is the cooling of the vapor-box inner wall due to heat deposit by the plasma low energy tails. As it was calculated in chapter 5, the power deposit to a target, when plasma temperature is below 0.4 eV, is in a range that can be handled by actively cooled tungsten, but this, together with tungsten erosion has to be experimentally tested.

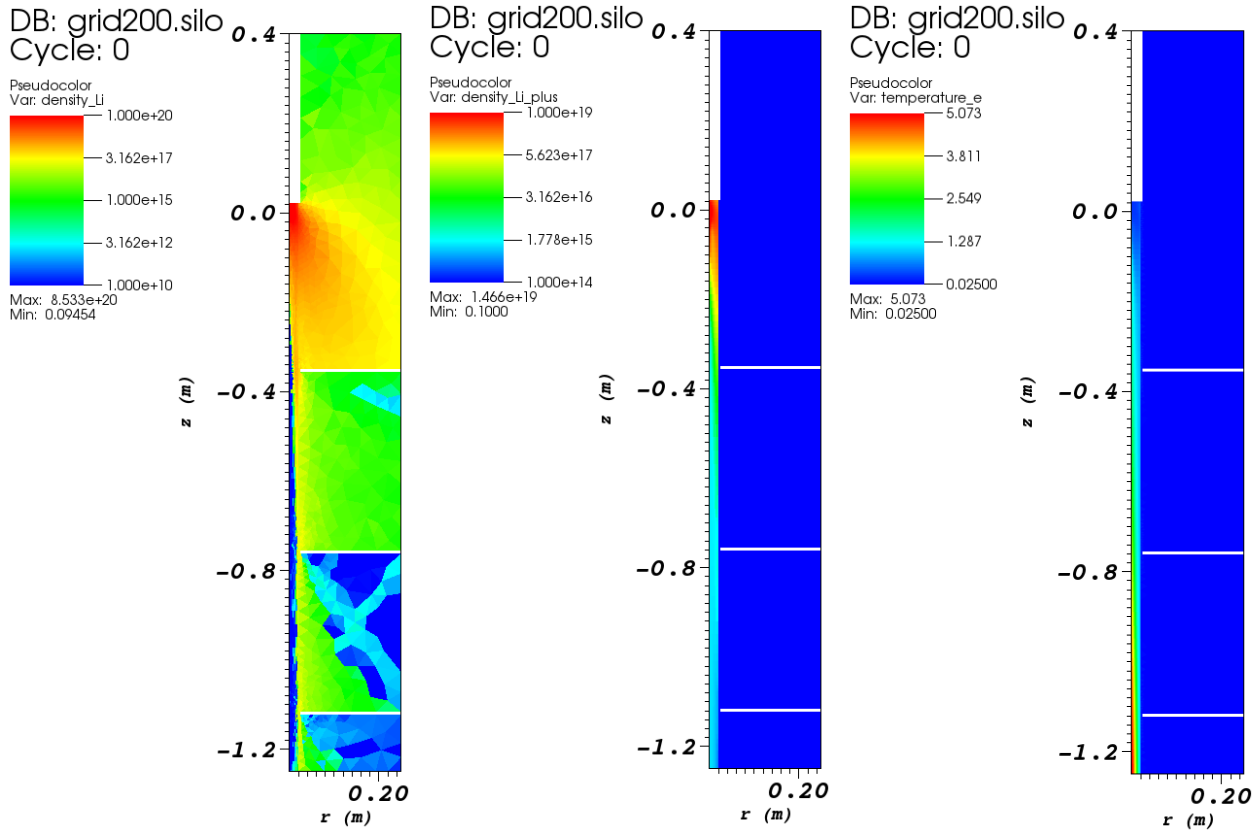

(a) Li density (b) Li^+ density (c) T_e

Figure 7.2: Results obtained using the alternative geometry where Magnum-PSI heating chamber is divided in two different chamber by an additional internal wall.

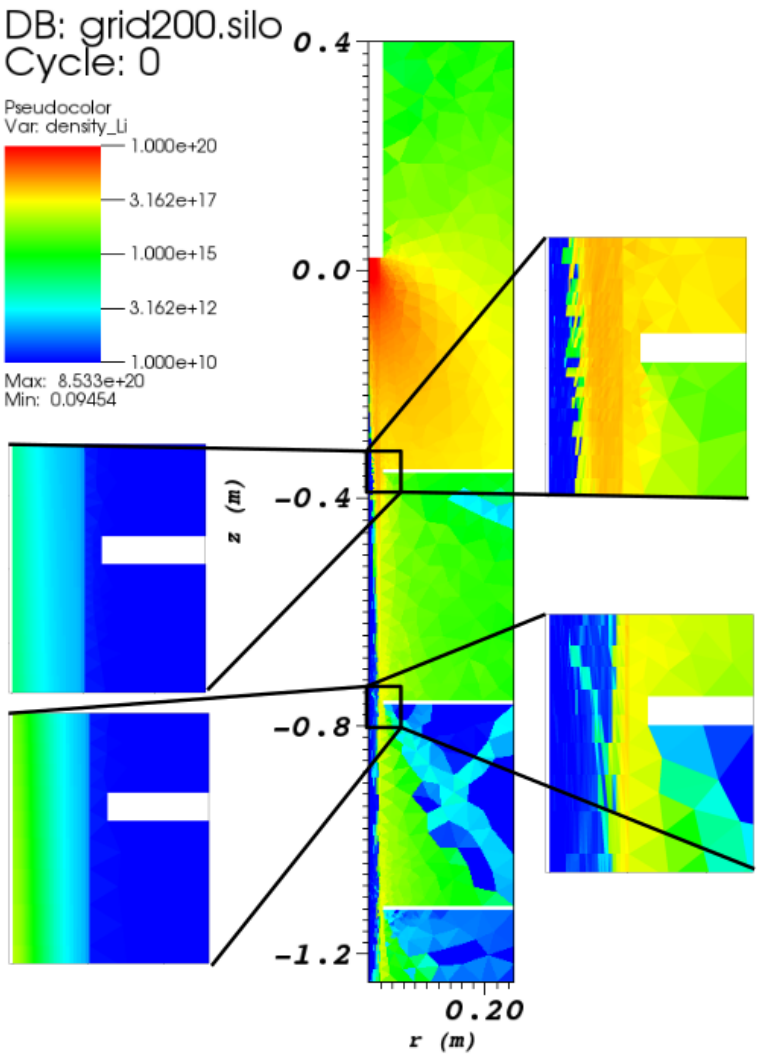

Figure 7.3: Li density and plasma temperature at the internal walls.

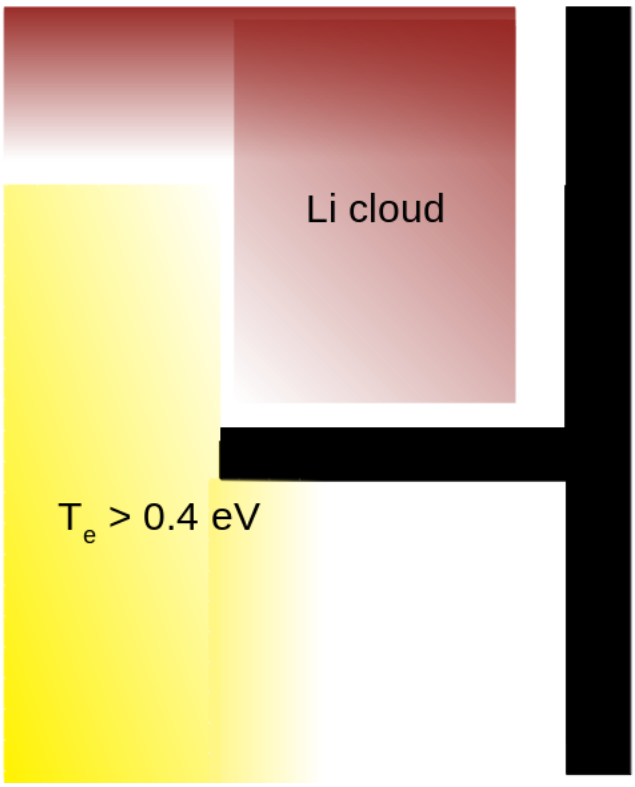

Figure 7.4: Vapor box geometry proposal.

The vapor-box cooling and erosion can be tested in linear devices like Magnum-PSI.
To understand where the 0.4 eV plasma temperature surface is, coupled dynamic-kinetics simulations like these must be carried on in order to design the vapor box with the required precision. The simulation of this geometry is not possible with B2.5; the code in fact requires a rectangular geometry, that then can be curved to simulated the entire scrape of layer of a toroidal device, but no "cut", like the one described in figure 7.4 can be made in the plasma geometry.

7.2.2 Divertor geometry

Whit using the same physical principle that has been explained in the previous section a similar recipe is proposed for the lithium target geometry. The idea is having not a single block of porous tungsten connected to a lithium reservoir, but a porous tungsten target surrounded by tungsten blocks.
A sketch of the proposed divertor plate geometry is shown in figure 7.5. The geometry and the ratio between plasma diameter and lithium target diameter is similar to those of the simulations of the so called *Plasma temperature scan* in chapter 5. In those simulation the width of the plasma temperature distribution was larger than the the lithium target diameter, therefore, in some of those simulation, the plasma that was hitting the target holder had energy higher than 0.4 eV. The fact that plasma temperature at the target holder, next to the lithium target, was was higher or lower than 0.4 eV was the crossing point between lithium jet from the target and ionization-recombination transport.
It has been proven that the latter is a slower transport channel and that lithium density in the vapor boxes can be reduced drastically eliminating lithium direct jet from the target.
For those reasons this target geometry is proposed for future experiments at Magnum-PSI. Magnum-PSI beam width can not be adapted arbitrary, so, in order to test different target diameter-plasma temperature width ratio, different targets should be made.

In future fusion application the main issue will be the sizing of each component and the power handling of the outer part of the target not protected by lithium cooling. Again it is very important that the energy crossing point in lithium CR model is at a temperature (0.4 eV) that nowadays tungsten plates already handle. Lithium is now considered the best option for liquid metal divertor because of its low atomic number and high capillarity, but this low energy crossing point in the CR model could

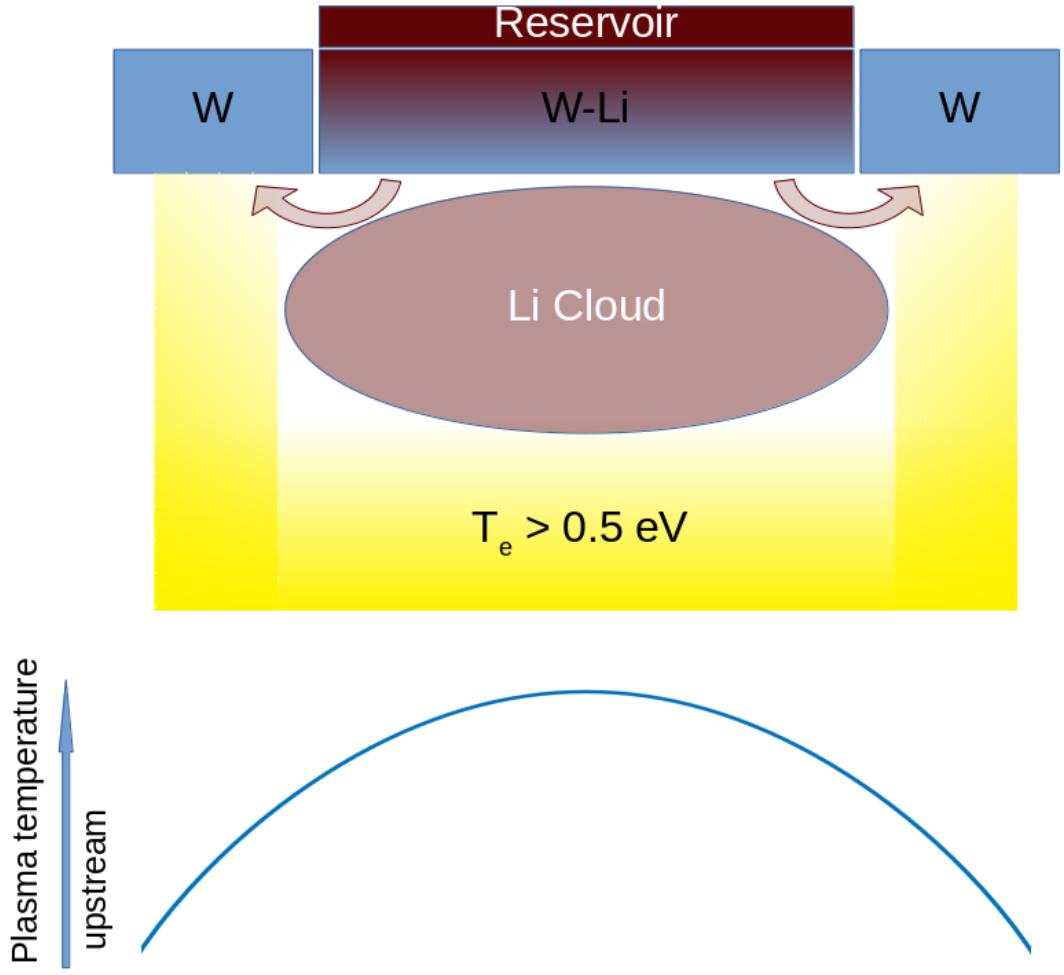

Figure 7.5: Divertor geometry.

be another reason to chose liquid lithium divertors over solution based on other elements.

7.2.3 Next experimental validation with Magnum-PSI

An experimental campaign will start in the next months at Magnum-PSI, in those weeks the described liquid metal target will be exposed to Magnum-PSI plasma beam. The experiments will be made with the aim of testing the liquid lithium target and its properties and of validating the predictions of B2.5-Eunomia coupled codes.
Some quantities will be chosen to experimentally validate the coupling of the codes. According to the simulation results shown in this thesis the most important quantities to be check are Li and Li^+ density in and out of the lithium cloud and the plasma temperature close to the target and out of the lithium cloud.

Because of the relative position target and Thompson scattering laser and detector, in Magnum-PSI, when operating with liquid metals, Thompson scattering is not available at position $z = 0\,\text{cm}$; for this reason measures of plasma temperature close to the target won't be available.
It is possible to make Thompson scattering measures upstream, in the heating chamber, where the lithium density is lower. Plasma density and temperature profiles upstream can be used as input parameters for B2.5-Eunomia runs. The target temperature distribution, an important parameter in the simulations as it was shown, will be measured by pyrometry and spectral thermography. The error associated with a pyrometer measure at about 800 K is $\pm 50\,\text{K}$. As it was shown in the previous chapters, a 50 K bias on target temperature can make huge difference in plasma-neutral interaction, especially in the extension on the plasma could; more than one simulation should be run, each one with different target temperature in the error range.
Validation will be mainly done comparing simulation data with spectroscopic data. A multi-channel spectrometer will be positioned at axial position $z = 0\,\text{cm}$, this spectrometer is made by three acquisition channels each one of them looking at the same axial and radial position but in different frequency range. One of the channel is set to the Balmer series of hydrogen range, this is the same range where the $3p \rightarrow 2p$ transition of Li at 323 nm is; a second channel range will be set between 500 nm and 780 nm for measuring the $2p \rightarrow 2s$ line at 671 nm; the third channel has a wave length range from to 750 nm to 950 nm and will check the $3s \rightarrow 2p$ line at 813 nm. The absolute intensity of each line of hydrogen and lithium, together to their relative intensity will give information about H and Li temperature and density in a certain axial and radial position thanks to the CR model. The comparison between the $2p \rightarrow 2s$ transition of lithium and other lithium lines will validate the approximation that was made on lithium energy states.
A second spectrometer, a Jarrell Ash spectrometers, will be positioned at the same axial position. The Jarrel Ash spectrometer is made of an array of 20 spectrometers looking at different radial positions. The spectral range of the Jarrel Ash spectrometer will be from 650 nm to 850 nm. In this range the two most important lithium lines, at 671 nm and 813 nm will be measured. This will allow to have a radial profile of lithium density and temperature.
During my project at DIFFER I took care of the data collection for the absolute calibration of the multi-channel spectrometer and the energy calibration and absolute calibration of the Jarrel Ash spectrometer. The energy calibration of the Jarrel Ash spectrometer was done with a argon vapor lamp; the intensity calibration of both spectrometers was done using a uniform emitting white sphere lamp with variable intensity that could be set by an input current. During the calibration, between the lamp and the spectrometers, the same window, that after the calibration was mounted on Magnum-PSI to avoid transmittance bias, was positioned.
The possibility of using a bolometer, and the calibration of the bolometer itself, in liquid lithium target experiments at Magnum-PSI, is currently being studied at DIFFER.

The total lithium loss from the target can be calculated by weighing the target before and after plasma exposure. The experimental lithium loss could be compared to the lithium flow predicted by the simulations. It must be considered that in the simulations two steady state codes are implemented, so their predictions are accurate in the initial and final transient of each shot.

Finally, by knowing the external target cooling, target temperature and heat transport trough the target, an estimation on power deposit to the target can be done and compared to the predictions of the simulations.

Chapter 8

Conclusions

At the beginning of this master thesis project the goals were divided in computational-modeling and physical goals.
The computational and modeling goals aimed at the completion of the coupling of the codes with lithium, including and expanding the previous standalone models in a coupled model. After that, the procedure for running the codes had to be optimized. Then the limits of the model and and internal validation method had to be found.
The physical goals were understanding, from simulation output analysis, lithium transport and cooling channel, finding recipes to increase cooling and reduce lithium transport upstream and proposing future experiments to validate the code output and the consequent physical analysis.

8.1 Setting up the models

The coupling of the two codes with lithium has been performed and runs successfully. The two codes are able to communicate with each other in different plasma and neutral regimes.

A procedure was found with which it is possible to reach convergence with different physical conditions (chapter 4). The different input parameter that have been tested are: plasma temperature peak from 4 eV to 7 eV, plasma temperature distribution and target temperature from 550 K to 850 K. It was found that the higher the lithium density the more difficult finding a physically meaningful convergence of the coupled codes.
With high lithium density, corresponding to high target temperature or low plasma temperature, it was found that, while looking for convergence, it is important to avoid oscillation of plasma and neutral quantities. The oscillation of those quantities with high lithium density is due to the importance of lithium-plasma interaction: the higher the amount of lithium, the bigger the effect on plasma particles. For this reason plasma profile can change rapidly each iteration and the oscillation of both, plasma and neutral particles gets bigger. The oscillations proven to leave trapped neutral lithium particles in high temperature plasma regions that are unphysical; when those oscillation happens, the simulation has to be restarted with smaller time discretization.
Solutions was found to this problem, it consists in reducing dt but increasing the number of B2.5 iterations between Eunomia simulations.
The numerical convergence of the coupled runs was checked by using a script that had already been used successfully for $H-H_2$ only coupled simulations, see section 4.2.
The codes work consistently with each other as described in chapter 2 and chapter 3. The major plasma-plasma, neutral-neutral and plasma-neutral collisions have been included in the simulations, this was proven by implementing an external CR model, with the same collisions included in the simulations, whose results have been compared to some from literature. There are also nor Li or Li^+ losses in the simulation, but the predictable loss at the internal boundary at the B2.5 geometry.
From the external CR model the limits of collisional model, implemented in B2.5-Eunomia have been found.
To summarize the coupling of the codes and the internal validation of the coupling con be considered

successfully completed. The coupled codes are ready to simulate different experimental scenarios with different geometries and physical parameters in the limits found for the model.

8.2 Simulations results

In chapter 6, I proved that the usage of a coupled dynamic-kinetic code is fundamental when simulating plasma interaction with a liquid metal target. This has been proven by comparing standalone runs with coupled runs with similar physical parameters. The reason why standalone runs are never an option to describe such a dynamics is that there are no operational ranges where plasma effects on neutrals are negligible or the other way around.

To understand lithium cooling contributions in different regimes I ran the codes with different physical configurations. It was found that the most important lithium cooling channel is Li ionization, which amounts to about 60% of the total plasma cooling. For this reason plasma cooling by plasma-lithium interaction was found to mainly take place in the zone where both Li and Li^+ particles are abundant. Thus, the plasma beam can be divided in three parts: the upper part upstream where $n_{Li^+} \gg n_{Li}$ where lithium cooling is only driven by thermalization of upcoming Li^+ particles; the zone close to the target where the lithium cloud is and cooling is provided by plasma-neutral interaction in therms of elastic collisions and excitation and radiation emission; the intermediate part, where the majority of the plasma cooling occurs, is the zone where $n_{Li^+} \simeq n_{Li^+}$, in this zone ionization and recombination collision continuously take place. This intermediate zone is located where the plasma temperature is about 0.4 eV according to the external CR model.

I found that there are two different lithium transport channels upstream in the chamber: the first and the faster is the standard neutral lithium transport by diffusion and jet from the target; the second and slower one process is a multi-step process: by ionization of neutral particles, transport of ion to a lower energy region and then recombination. Due to the different diffusive speed the latter process is the one that reduces lithium loss diffusion out of the beam.
Since lithium transport is slower in the second case, due to magnetic confinement, it was found that 0.4 eV plasma temperature surfaces are also high Li density surfaces and that plasma temperature higher than 0.4 eV is a lithium confinement method.
Consequently the recombination factor is always larger than 90% when the plasma temperature close to the target reaches 0.4 eV, the CR model crossing point between Li and Li^+ abundance, and immediately drops down to 80% or less when the plasma temperature is lower than 0.4 eV. The energy deposit to the target was calculated for every different run. It was proven that lithium cooling saturates, this means that after reducing the plasma temperature in front of the target to 0.4 eV the energy to the target decreases very slowly despite the increasing by orders of magnitude of lithium flux from the target.
For those reasons, I can conclude that the liquid metal divertors (LMDs) are a solution for future fusion devices and that the modelling of LMDs must be done with coupled kinematic-dynamic codes. The cooling provided by the lithium cloud can reduce plasma heat to the target to regimes that tungsten targets can handle. The main problem with liquid metal divertors is the impurity flux upstream. In order to reduce this flux two solutions were proposed: a geometric configuration of the target and a geometric configuration for the vapor-box. In both solution the temperature cross point in lithium collisional radiative model is used to confine lithium.

In the proposed target geometry the liquid lithium target would only be the central part of the divertor plate, the outer part, where the incoming plasma temperature is lower would be a pure tungsten target. This way neutral lithium is emitted only in the central part of the target and it is confined by the external plasma that directly hit the pure tungsten target.
Coupled kinetic-dynamic simulation would play a major role in designing such a target before testing, in fact plasma temperature profile has to be found in order not to exceed the maximum energy load that the target can handle but making sure that the plasma temperature to the outer part of the target

is about 0.4 eV to confine neutral lithium.

The total geometry of Magnum-PSI was simulated to understand lithium transport in the experiment and to find the most relevant quantities to be checked during the experimental validation campaign. The extension of the neutral lithium cloud and plasma temperature in the lithium cloud have been found to be the most important validation parameters.
Since Magnum-PSI has a vapor-box-like geometry, the output of the simulations could be related to vapor-box-like scenario.
Lithium transport in the low energy-low density plasma region is demonstrated to be the main lithium transport channel from chamber to chamber in Magnum-PSI geometry and in a possible similar vapor-box configuration.

According to these results, a possible geometry for future vapor box was proposed. It consists in extending the internal walls of the vapor-box in order to intercept the low energy tails of the plasma beam itself. The internal walls would absorb part of the energy from the plasma but would avoid lithium transport upstream in the low plasma temperature region. With B2.5-Eunomia it is not possible to generate a geometry where the internal walls intercept part of the plasma column due to geometrical limits of B2.5.

8.3 Possible future scenarios

The physics of plasma-neutral cloud interaction and the most important cooling channels have been studied. Some other simulations can be performed using the total Magnum-PSI geometry. One of the phenomena that should be quantified is the influence of plasma density on Li^+ transport upstream. The higher the plasma density, the higher the momentum transfer collisions frequency but this behavior must be quantified.
Designing future fusion devices Li^+ flux must be known and kept under the Greenwald limit to avoid disruption. Future simulations must focus on quantifying lithium flux upstream and on relating results of simulation in linear geometry to toroidal geometry.
Deuterium/hydrogen[1] retention is a phenomenon that was not implemented in my simulations but it should be considered because lithium and hydrogen form lithium hydride, LiH, a molecule that dissociates at 900 K. The presence of LiH in the very top layer of the target that has two consequences: first of all the increasing of slow hydrogen particles coming from the target to the plasma by evaporation; second the reduction of deuterium absorption due to partial saturation. For those reasons in the facing target plasma there will be evaporated and reflected deuterium particles. This could be described by setting a reflection or retention probability and a hydrogen source from the target. LiH decomposition and consequent deuterium evaporation would be calculated from the target temperature.

8.3.1 Experimental validation

An experimental campaign will start in October 2018 at Magnum-PSI, by exposing the described liquid metal target will be exposed to Magnum-PSI plasma.
Experimental data like plasma density and temperature profiles upstream a target temperature will be used as input parameters of simulations whose output will be compared to spectroscopic data for validation of the coupling.
The physical phenomena that will be checked are: the presence of the lithium cloud in front of the target, the density of the lithium cloud in front of the target and the fact that the lithium target density remains constant even if, with higher lithium flux from the target, the lithium cloud expands. The last quantity that can be checked is plasma heat flux to the target, knowing target temperature and heat transmission in the target.

[1] In future fusion device the plasma entering the divertor region will be a deuterium/tritium plasma; in the previous simulations and in the first experiments at Magnum-PSI the plasma beam will be a hydrogen beam.

A radial scan of lithium density can be done using the spectrometers and bolometer available at DIFFER. The position and extension of the lithium cloud will be the main quantities to check.

8.3.2 Fusion application

For future fusion application, possible experiments with the vapor-box geometry at Magnum-PSI are now being considered in collaboration with the University of Princeton. The experimental setup will be made of a vapor box inside Magnum-PSI vacuum chamber in order to test lithium cooling and transport in proper vapor box geometry.

Nowadays there are no tokamaks with liquid metal divertor and different liquid metal divertors configurations are being studied.
Shortly the detailed design of the DTT (Divertor Test Tokamak), the facility that will be built for testing DEMO divertor will start. It has already been decided that one of the alternative divertor configurations is the liquid metal divertor. Testing with DTT will be fundamental to understand the possibility of using LMDs in DEMO, the demonstrative divertor.

Acknowledgement

I did my thesis working for a initial period with the fusion group of the Technische Universiteit of Eindhoven (TU/e). I would like to thank the group leader, professor Niek Lopez Cardozo for welcoming me in his group, and making me feel a part of it. I would like to thank professor Roger Jasper who helped with the introduction in the group, and everyone in the fusion group: professors, researchers, secretaries, PHD students and students who were doing their final project like me.
I would specially like to thank Peter Rindt, PHD student at TU/e, who helped me with finding and defining my project even before coming to Eindhoven. Unfortunately, for technical reasons, we couldn't proceed with the experimental campaign that we were planning together; nevertheless his contribution to this work was fundamental thanks to the time he invested in it and the suggestions he gave me.

I spent the most of the time of my project working at the Dutch Institute For Fundamental Energy Research (DIFFER) in the Computational Plasma Physics and Chemistry group (CPPC). I would like to thank the group leader Paola Diomede for welcoming me in her group and all the people at DIFFER for the time I spent there.
I would especially like to thank my supervisors at DIFFER doctor Hugo De Blanck and Ray Chandra for helping me with my project from the very first day at DIFFER. Their contribution to this project was fundamental thanks to the advice and the help they gave me during the project.

I would like to thank my internal supervisor doctor Gianluigi Serianni that suggested me to try this experience abroad about two years ago. I really need to thank him for the help he gave me in the latest stages of this work.

Bibliography

[1] ABRAMS, T. W. Erosion and Re-Deposition of Lithium and Boron Coatings Under High-Flux Plasma Bombardment. *Princeton University* (2015).

[2] Amjuel. *B2.5-Eunomia simulations of Pilot-PSI (PhD thesis).* 2012.

[3] AMJUEL. *B2.5-Eunomia simulations of Pilot-PSI (PhD thesis).* 2012.

[4] Ata., M. A convergence criterion for the monte carlo estimates. *Simulation Modelling Practice and Theory 15* (2006), 237–246.

[5] A.V.Chankin, D.P.Coster, R. C. G. A. L. A. M. A. K. H. J. R. M. Comparison between measured divertor parameters in asdex upgrade and solps code solutions. *Journal of Nuclear Materials 363–365* (2007), 335–340.

[6] Chandra, R. Simulation of neutral lithium atoms in Magnum-PSI using Eunomia.

[7] Chen, C., Bian, L., and Ma, J. From traces to trajectories: How well can we guess activity locations from mobile phone traces? *Transportation Research Part C: Emerging Technologies 46*, 2017 (2014), 326–337.

[8] Choudhuri, A. *The Physics of Fluids and Plasmas.* Cambridge University Press, 2012.

[9] DATABASE:. http://open.adas.ac.uk/. *OPEN-ADAS database.*

[10] De Temmerman, G., Van Den Berg, M. A., Scholten, J., Lof, A., Van Der Meiden, H. J., Van Eck, H. J., Morgan, T. W., De Kruijf, T. M., Zeijlmans Van Emmichoven, P. A., and Zielinski, J. J. High heat flux capabilities of the Magnum-PSI linear plasma device. *Fusion Engineering and Design 88*, 6-8 (2013), 483–487.

[11] Goldston, R. J., Hakim, A., Hammett, G. W., Jaworski, M. A., and Schwartz, J. Recent advances towards a lithium vapor box divertor. *Nuclear Materials and Energy 12* (2017), 1118–1121.

[12] H.J.N.van Eck, T.Abrams, M. d. B. S. G. E. M. R. H. d. M. T. M. d. P. J. P. G. T. P. V. P. v. E. Operational characteristics of the high flux plasma generator Magnum-PSI. *Fusion Engineering and Design 89*, 2150–2154.

[13] Honig, R. E. Vapor pressure data for the solid and liquid elements. *RCA review 1*, 30 (1969), 285–305.

[14] Intergovernmental Panel on Climate Change. Climate Change 2014 Mitigation of Climate Change. *Climate Change 2014: Mitigation of Climate Change. Contribution of Working Group III to the Fifth Assessment Report of the Intergovernmental Panel on Climate Change* (2014), 1454.

[15] Jaworski, M. First-wall, plasma-material interaction, liquid metals, and strategic elements for advancing liquid metal science and technology. *Presentation to the NAS Committee for a Strategic Plan for U.S. Burning Plasma Research April 12, 2018* (2018).

[16] John Scholten, P.A.Zeijlmans van Emmichoven, H. E. P. G. T. S. M. d. B. H. d. M. M. d. P. M. P. A. J. Operational status of the Magnum-PSI linear plasma device. *Fusion Engineering and Design 80*, 1785–1788.

[17] LaBombard, B. Adx a high-field, high power density advanced divertor and rf tokamak experiment. *ES Community Planning Workshop: Plasma-Materials Interactions PPPL, Princeton, NJ – May 4-6, 2015* (2015).

[18] Langmuir, I. The Condensation and Evaporation of Gas Molecules. *Proceedings of the National Academy of Sciences 3*, 1 (1917), 141–147.

[19] Lieberman, M. *Plasma sheath and surfaces.*

[20] Machielsen, M. Modelling lithium density in the plasma of magnum-psi. *Master Thesis in Fusion* (2018).

[21] Metropolis, N., Rosenbluth, A., Rosenbluth, M. N., and Teller, A. H. Equation of state calculations by fast computing machines. *The journal of chemical ... 21*, 6 (1953), 1087–1092.

[22] Morozov, D. K. Greenwald density limit and power balance in tokamaks. *J. Phys.: Conf. Ser 941* (2017).

[23] Nygren, R. E., and Tabarés, F. L. Liquid surfaces for fusion plasma facing components—A critical review. Part I: Physics and PSI. *Nuclear Materials and Energy 9* (2016), 6–21.

[24] Olivier, J. G. J., Schure, K. M., and Peters, J. A. H. W. Trends in Global CO2 and Total Greenhouse Gas Emissions: Summary of the 2017 report. *PBL Netherlands Environmental Assessment Agency*, September 2017 (2017).

[25] Pace, L. D., El-Guebaly, L., Kolbasov, B., Massaut, V., and Zucchetti, M. Radioactive waste management of fusion power plants. *Radioactive waste* (2012).

[26] Rindt, P., Lopes Cardozo, N. J., van Dommelen, J. A., Kaita, R., and Jaworski, M. A. Conceptual design of a pre-loaded liquid lithium divertor target for NSTX-U. *Fusion Engineering and Design 112* (2016), 204–212.

[27] Sun, H. Study of near scrape-off layer (SOL) temperature and density gradient lengths with Thomson scattering. *Plasma Physics and Controlled Fusion 57*.

[28] Tamai, H. Behaviour of divertor neutral pressure during the divertor detachment in the pumped w-shaped divertor of jt-60u. *EPS Conf. on Contr. Fusion and Plasma Physics, Maastricht 23J*.

[29] T.D.Rognlien, A.G.McLean, M. M. A. I. C. W. A. G. M. Comparison of 2D simulations of detached divertor plasmas with divertor Thomson measurements in the DIII-D tokamak. *Nuclear Materials and Energy 12* (2017), 44–50.

[30] van Eden et al., G. Oscillatory vapor shielding of liquid metal walls in nuclear fusion devices. *Nature communication 1*, 8 (2017).

[31] Wieggers R.C. *B2.5-Eunomia simulations of Pilot-PSI (PhD thesis).* 2012.

[32] You, J. H., Visca, E., Bachmann, C., Barrett, T., Crescenzi, F., Fursdon, M., Greuner, H., Guilhem, D., Languille, P., Li, M., McIntosh, S., Müller, A. V., Reiser, J., Richou, M., and Rieth, M. European DEMO divertor target: Operational requirements and material-design interface. *Nuclear Materials and Energy 9* (2016), 171–176.